AFRL-MN-EG-TR-2005-7030

STEADY FLOW OF A PARTICULATE TARGET MEDIUM OVER A PROJECTILE: EXPERIMENTS AND MODELING

Oana Cazacu
Nicolaie D. Cristescu

Graduate Engineering and Research Center
University of Florida
1350 N. Poquito Road
Shalimar, FL 32579

CONTRACT NO. F08630-01-1-0007

FEBRUARY 2005

FINAL REPORT FOR PERIOD APRIL 2001 – AUGUST 2004

DISTRIBUTION A

Approved for Public release; further distribution unlimited.

AIR FORCE RESEARCH LABORATORY, MUNITIONS DIRECTORATE

■ **Air Force Materiel Command** ■ **United States Air Force** ■ **Eglin Air Force Base**

NOTICE

When Government drawings, specifications, or other data are used for any purpose other than in connection with a definite Government-related procurement, the United States Government incurs no responsibility or any obligation whatsoever. The fact that the Government may have formulated or in any way supplied the said drawings, specifications, or other data is not to be regarded by implication, or otherwise in any manner construed, as licensing the holder, or any other person or corporation; or as conveying any rights or permission to manufacture, use, or sell any patented invention that may in any way be related thereto.

This technical report is releasable to the National Technical Information Services (NTIS). At NTIS it will be available to the general public, including foreign nations.

Contract Number: F08630-01-1-0007

Contractor: Graduate Engineering & Research Center,
University of Florida
1350 N. Poquito Road
Shalimar, FL 32579

This technical report has been reviewed and is approved for publication.

FOR THE COMMANDER

//ORIGINALLY SIGNED//

Frederick A. Davis
Technical Director
Assessment and Demonstrations Division

//ORIGINALLY SIGNED//

Dr. Yen Tu
Program Manager

Anyone having need of a copy of this report should first contact the Defense Technical Information Center (DTIC) at the address shown below. If you are a registered DTIC User, DTIC can provide you with a copy. Please do not request copies from the Air Force Research Laboratory, Munitions Directorate. Requests for additional copies should be directed to:

Defense Technical Information Center (DTIC)
8725 John J. Kingman Road, Ste 0944
Ft Belvoir, VA 22060-6218

This report is published in the interest of the scientific and technical information exchange. Publication of this report does not constitute approval or disapproval of the ideas or findings.

If your address has changed, if you wish to be removed from our mailing list, or if your organization no longer employs the addressee, please notify AFRL/MNAC, Eglin AFB FL 32542-6810, to help us maintain a current mailing list. Do not return copies of this report unless contractual obligations or notice on a specific document requires that it be returned.

REPORT DOCUMENTATION PAGE

Form Approved
OMB No. 0704-0188

Public reporting burden for this collection of information is estimated to average 1 hour per response, including the time for reviewing instructions, searching existing data sources, gathering and maintaining the data needed, and completing and reviewing this collection of information. Send comments regarding this burden estimate or any other aspect of this collection of information, including suggestions for reducing this burden to Department of Defense, Washington Headquarters Services, Directorate for Information Operations and Reports (0704-0188), 1215 Jefferson Davis Highway, Suite 1204, Arlington, VA 22202-4302. Respondents should be aware that notwithstanding any other provision of law, no person shall be subject to any penalty for failing to comply with a collection of information if it does not display a currently valid OMB control number. **PLEASE DO NOT RETURN YOUR FORM TO THE ABOVE ADDRESS.**

1. REPORT DATE *(DD-MM-YYYY)* 27-02-2005	**2. REPORT TYPE** Final	**3. DATES COVERED** *(From - To)* April 2001 – August 2004

4. TITLE AND SUBTITLE
Steady Flow of A Particulate Target Medium Over A Projectile:
Experiments and Modeling

5a. CONTRACT NUMBER
F08630-01-1-0007

5b. GRANT NUMBER
N/A

5c. PROGRAM ELEMENT NUMBER
65502C

6. AUTHOR(S)
Oana Cazacu, Nicolaie D. Cristescu

5d. PROJECT NUMBER
2502

5e. TASK NUMBER
07

5f. WORK UNIT NUMBER
33

7. PERFORMING ORGANIZATION NAME(S) AND ADDRESS(ES)

Graduate Engineering and Research Center
University of Florida
1350 N. Poquito Road
Shalimar, FL 32579

8. PERFORMING ORGANIZATION REPORT NUMBER

9. SPONSORING / MONITORING AGENCY NAME(S) AND ADDRESS(ES)
Air Force Research Laboratory, Munitions Directorate
AFRL/MNAC
101 W. Eglin Blvd, Ste 334
Eglin AFB, FL 32542
850-882-8303 ext. 3431

10. SPONSOR/MONITOR'S ACRONYM(S)
AFRL-MN-EG

11. SPONSOR/MONITOR'S REPORT NUMBER(S)
AFRL-MN-EG-TR-2005-7030

12. DISTRIBUTION / AVAILABILITY STATEMENT

DISTRIBUTION
Unlimited – Approved for Public Release

13. SUPPLEMENTARY NOTES

14. ABSTRACT
Report developed under contract No. F08630-01-1-0007.
This report presents the results of an experiment study on the deformation and strength properties of several particulate systems under quasi-static compression for a variety of loading histories and strain rate conditions. To gain better understanding of the role of particle size distribution, initial porosity and loading history on compaction, triaxial compression data were obtained on selected cohesive systems: 1. Spherical silica particles (silicon dioxide, floated powder) with a mean size of 63.5μm, 2. Cylindrical Polyethylene pellets, 4mm in height and 3mm in diameter, 3. Angular microsystalline cellulose, PH105, with a mean particle size of 20μm. The experiments were complemented with model development in the frame work of plasticity and viscoelasticity theories. Comparison between the theory and data obtained show that the models developed describe very well the main features of the behavior observed in the range of pressure and strain rates considered.

15. SUBJECT TERMS: University Grant Report, High Strain-Rate Response, Characterization of Particulate Medium, Penetration Mechanics.

16. SECURITY CLASSIFICATION OF:			**17. LIMITATION OF ABSTRACT**	**18. NUMBER OF PAGES**	**19a. NAME OF RESPONSIBLE PERSON** Dr. Yen Tu
a. REPORT unclassified	**b. ABSTRACT** unclassified	**c. THIS PAGE** unclassified	UL	90	**19b. TELEPHONE NUMBER** *(include area code)* 850-882-8303 x-3431

Standard Form 298 (Rev. 8-98)
Prescribed by ANSI Std. Z39.18

TABLE OF CONTENTS

ABSTRACT ii
LIST OF FIGURES iv

SECTION **TITLE**

I **TASK 1: EXPERIMENTAL CHARACTERIZATION OF PARTICULATE SYSTEMS** 1

I.1 Introduction 1
I.2 Experimental Set-up 2
I.3 Experimental Results on Silica Powder 6
I.3.1. Material Characteristics 6
I.3.2. Monotonic Test Results on Silica Powder 8
I.3.3. Cyclic Test Results on Silica Powder 14
I.4 Experimental Results on Polyethylene Pellets 18
I.4.1 Material Characteristics 18
I.4.2 Monotonic Test Results on Polyethylene Pellets 18
I.4.3 Cyclic Test Results on Polyethylene pellets 25
I.4.4 Long-term Creep Test on Polyethylene pellets 30
I.5 Experimental Results on microscrystalline cellulose 32
I.5.1. Material Characteristics 32
I.5.2 Cyclic Test Results on microcrystalline cellulose 32
I.6 References Section I 36

II **TASK 2: CONSTITUTIVE MODELING OF THE RESPONSE OF THE PARTICULATE SYSTEMS** 38
II.1 Introduction 38
II.2 Elastic/Plastic constitutive model for the Polyethylene system 39
II.3 Numerical implementation and comparison with experimental results 44
II.4. Constitutive Modeling of the Behavior of the Silica System 48
II.4.1 Elastic/plastic Approach 48
II.4.2 Numerical Implementation 52
II.4.3 Viscoelastic Modeling 55
II.5. Summary and conclusions 59
II.6. References Section II 61

III **TASK 3: ANALYSIS OF THE STEADY-STATE FLOW OF A COMPRESSIBLE POROUS VISCOPLASTIC MEDIUM** 64

III.1. Introduction 64
III. 2. Constitutive model for the target 65
III. 3. Computation of the resistance to penetration at steady-state 67
III.3.1. Statement of the problem 67
III.3.2 Friction laws 69
III.3.3. Resistance to penetration 70
III.4. Application to WES 5000 concrete (data after Schmidt (2003)) 73
III.5 Application to concrete (data from Osborn (1981)) 78
III.6. References Section III 89

ABSTRACT

This report presents the results of an experimental investigation on the deformation and strength properties of several particulate cohesive systems under quasi-static compression for a variety of loading histories and strain rates conditions. These systems are: (i) *silica* (silicon dioxide) powder, *spherical* particles having a mean particle size of 63.5 μm; (ii) *polyethylene pellets*, *cylindrical* in shape (4 millimeters in height by 3 millimeters in diameter), and (iii) microscrystalline cellulose, PH-105, of angular shape and mean particle size 20μm. The experimental activities were complemented with model development in the framework of plasticity and viscoelasticity theories. Comparison between theory and data show that the models developed describe very well the main features of the behavior observed in the range of pressures and strain rates considered in the experimental investigation. A new model for calculating the resistance to penetration into compressible porous viscoplastic media was proposed. The influence of the characteristics of the penetrator/target interface, impact velocity, target mechanical properties and nose geometry on the resistance to penetration were investigated.

LIST OF FIGURES

SECTION I

Figure 1.1	Schematic diagram of the triaxial tester and new volume change device	4
Figure 1.2	Device and split mold for controlled pre-compaction of the particulate systems prior testing	6
Figure 1.3	SEM micrograph of monosized silica of mean particle size of 63.5 μm (or 240 mesh	7
Figure 1.4	Pressure vs. volumetric strain response under hydrostatic compression for silica	9
Figure 1.5(a)	Deviatoric stress vs. axial strain at 93 kPa confinement	10
Figure 1.5(b)	Deviatoric stress vs. volumetric strain at 93 kPa confinement	11
Figure 1.6	Volumetric strain profiles for confining pressures of 93 kPa, 40 kPa, and 70 kPa	12
Figure 1.7	Triaxial compression cell with deformed specimen	13
Figure 1.8(a)	Deviatoric stress vs. axial strain curve in a cyclic test at 27 kPa confinement	15
Figure 1.8(b)	Deviatoric stress vs. volumetric strain in a cyclic test at 27 kPa confinement	16
Figure 1.8(c)	Zoom in of the deviatoric stress vs. volumetric strain curve in a cyclic test under 27 kPa confining pressure showing the change in creep direction as the passage between the compressibility and dilatancy regime.	17
Figure 1.9	Pressure vs. volumetric strain response under hydrostatic compression for PE pellets	19
Figure 1.10(a)	Stress - axial strain curves showing the effect of confining pressure on the behavior of polyethylene pellets	20
Figure 1.10(b)	Stress-volumetric strain curve showing compressibility followed by dilatancy	21
Figure 1.11(a)	Stress-axial strain curves in monotonic triaxial compression test at σ_3 = 14 kPa showing the strain rate sensitivity of polyethylene pellet	22
Figure 1.11(b)	Stress- volumetric strain curves.in monotonic triaxial compression test at σ_3 = 14 kPa showing the strain rate sensitivity of polyethylene pellets	23

Figure 1.12	Comparison between the volumetric stress-strain behavior of coated and non-coated polyethylene pellets showing that the coated system exhibits much more dilatancy and thus improved flowability	24
Figure 1.13(a)	Stress-axial strain curves in cyclic triaxial compression test at σ_3 = 35 kPa; before each partial unloading, axial load was kept constant; Young modulus E values computed from the unloading slopes are indicated	26
Figure 1.13(b)	Stress- volumetric strain curves in cyclic triaxial compression test at σ_3 = 35 kPa; before each partial unloading, axial load was kept constant; computed values of the bulk modulus K are indicated	27
Figure 1.14	Detail of the stress-volumetric strain curve at σ_3 = 35 kPa showing the change in creep direction as the material transitions from compressible to dilatant behavior	28
Figure 1.15	Comparison between the stress-axial strain curves at σ_3 = 35 kPa for monotonic and cyclic loading paths	29
Figure 1.16(a)	Evolution of the axial strain with time in a creep test over 24 hours at σ_3 = 14 kPa and σ_1 = 52.53 kPa showing that stabilization is reached within 20 minutes	30
Figure 1.16(b)	Volumetric strain versus time curve showing that volumetric creep doesn't stabilize within the duration of the test (24 hours at σ_3 = 14 kPa and σ_1 = 52.53 kPa	31
Figure 1.17	Deviatoric stress vs. volumetric strain curves for microcrystalline cellulose under confining pressures of 69 kPa , 138 kPa, and 207 kPa	33
Figure 1.18	Variation of the bulk modulus K for microcrystalline cellulose as a function of deviatoric stress showing increased compaction under shear conditions	34
Figure 1.19(a)	Strain rate effects on compaction as observed from the variation of volume in a deviatoric test for microcrystalline cellulose at a confining pressures of 69 kPa for crosshead speed of 100mm/min	34
Figure 1.19(b)	Strain rate effects on compaction as observed from the variation of volume in a deviatoric test for microcrystalline cellulose at a confining pressures of 69 kPa for crosshead speed of 10mm/min	35

SECTION II

Figure 2.1	Variation of the plastic work normalized by the atmospheric pressure with the stress level $f_p \equiv \left(\frac{I_1^3}{I_3} - 27\right) \cdot \left(\frac{I_1}{p_a}\right)^m$ at σ_3 = 14.7 and 35 kPa, respectively	41
Figure 2.2(a)	Comparison between theoretical and experimental stress-axial strain curves at σ_3 = 14 kPa and 35 kPa	46

Figure 2.2(b)	Comparison between theoretical and experimental stress-volumetric strain curves at σ_3 = 14 kPa and 35 kPa	47
Figure 2.3	Comparison between theoretical and experimental stress strain curves for hydrostatic compression on PE ellets	48
Figure 2.4	Comparison between the experimental and theoretical variation of the bulk modulus with the mean pressure for silica system	49
Figure 2.5	Mohr-Coulomb Yield Surface for silica system	50
Figure 2.6	Calculated Failure Surface and yield cap in triaxial plane.(b) trace of the yield surface in octahedral plane for silica	51
Figure 2.7	Mean stress vs. volumetric strain for silica system. Effects of hardening constant d	53
Figure 2.8	Simulated and experimental deviatoric stress vs. axial strain at 70.6 kPa for silica powder	54
Figure 2.9	Simulated and experimental deviatoric stress vs. volumetric strain curve corresponding to a confining pressure of 70.6 kPa for silica powder	55
Figure 2.10	Comparison between model prediction and data under σ_3 = 93 kPa	58
Figure 2.11	Comparison between the theoretical variation of the parameter m_1 and data (symbols)	59

SECTION III

Figure 3.1	Schematic of the flow over the wedge	68
Figure 3.2	Resistance to penetration σ_b normalized by the locking pressure p_* as a function of the projectile semi-angle α for different values of the friction coefficient between the target and the wedge tip; impact velocity V=300 m/s.	75
Figure 3.3	Optimum projectile semi-angle vs. impact velocity for various contact conditions between the wedge tip and viscoplastic target.	76
Figure 3.4	Normalized resistance to penetration corresponding to the optimum projectile semi-angle vs. the coefficient of friction between the wedge tip and viscoplastic target for various impact velocities	77
Figure 3.5	Hydrostat for 34.47 MPa concrete (after Osborn (1981))	79
Figure 3.6	Determination of the parameters involved in the pressure-density relationship of using Osborn(1981) hydrostat for 34.47 MPa concrete	81
Figure 3.7	Resistance to penetration σ_b normalized by the locking pressure p^* as a function of the projectile semi-angle α for different striking velocities V; $k(\rho_f) = 63\,k(\rho_0)$, μ = 0.2 and μ_r = 0.6	82
Figure 3.8	Optimum projectile semi-angle vs. impact velocity	83
Figure 3.9	Normalized resistance to penetration corresponding to the optimum projectile half-angle as a function of the impact velocity	84
Figure 3.10	Effect of friction between nose and target: the lower the friction the sharper the optimal nose angle	85
Figure 3.11	Resistance to penetration for optimum nose angle corresponding to different friction conditions at the nose/target interface	86
Figure 3.12	Optimum projectile semi-angle vs. impact velocity for $k(\rho_f):k(\rho_0)$= 63 and	

	30; coefficients of friction: μ = 0.2 and μ_r = 0.6	87
Figure 3.13	Resistance to penetration σ_b normalized by the locking pressure p^* corresponding to optimum nose semi-angles as a function of impact velocity for $k(\rho_f):k(\rho_0)$ = 63 and 30; coefficients of friction: μ = 0.2 and μ_r = 0.6	88

TASK 1: EXPERIMENTAL CHARACTERIZATION OF PARTICULATE SYSTEMS

I.1 Introduction

This task focus is on the experimental characterization of the compaction, deformation/flow behavior, and strength of various cohesive particulate systems. A variety of index tests of *flowability* exist such as the Hosokawa Powder Tester, or a Copley Tap Density Volumeter, both of which can be utilized to determine the *Hausner ratio* of aerated to tapped density, an often-used *index* of flowability (see for example Abdullah and Geldart, 1999). Such index tests are often useful in indicating whether one powder will flow more easily than another; however, they provide little information that can be used in a comprehensive model of the flow behavior. For many industrial applications a Jenike tester has become the default standard shear testing technique used to characterize the quasi-static strength of powders under a range of confining loads. This technique suffers from several shortcomings including sensitivity to the filling procedure and induced anisotropy in the sample through the initial compaction phase. Furthermore, the shear is non-uniform and the strain deformation is quite limited. The results change by as much as a factor of two if the shearing direction is changed from the direction of shear during the compaction phase (Feise, 1998). The resulting *flow function* is not a true *failure surface* that can be utilized in a mathematical constitutive model of bulk deformation.

A simple, yet accurate test is the triaxial compression test (Bishop and Henkel, 1962). In the triaxial compression test, measurements of both axial and volumetric strains undergone by the material could be done thus allowing the characterization of stress-strain response under axisymmetric 3-D conditions. Furthermore, all material properties determined by direct shear testing (ultimate strength, cohesion, angle of internal friction) could also be estimated from triaxial test data, with comparable results (Kandala and Puri, 2000).

The present task extends the current knowledge by characterizing the quasistatic behavior under compression for a variety of loading histories and strain rate conditions. The focus was on characterizing the behavior under dry conditions and in the low pressure regime. To gain a better understanding of the role of particle size distribution, initial porosity and loading history on compaction, triaxial compression data were obtained on selected cohesive systems: (i) *silica* (silicon dioxide, floated powder), *spherical* particles having a mean particle size of 63.5 μm; (ii) *polyethylene pellets*, *cylindrical* in shape (4 millimeters in height by 3 millimeters in diameter), and (iii) microscrystalline cellulose, PH-105, of angular shape and mean particle size 20μm.

Both monotonic and cyclic triaxial compression data in the low confining pressure regime are reported. By performing creep tests and confined compression tests at different strain rates, the time influence on the overall behavior as well the strain rate sensitivity of the material was characterized.

The experimental activities presented here are complemented with model development for the systems studied in Section II.

I.2 Experimental Set-up

Soil mechanics researchers have long recognized the value of triaxial testing in predicting the stress-strain and failure behavior of these geologic materials. However, the classic soil mechanics triaxial compression apparatus allows measurement of volume changes only for fully saturated conditions (see Bishop and Henkel (1962)). Yet, the potential for significant volume changes upon shearing under dry conditions can be great, since particles can form loose networks of contacts which can move as rigid bodies and cause dilation of the bulk material, or, can collapse to denser configurations. A few researchers are developing equipment capable of measuring the biaxial and triaxial response of particulate systems under dry conditions (*e.g.* Abdel-Hadi et al. (2000); Arthur (1985); Kandala and Puri (2000); Verwijs et. al.(2002); etc.).

The equipment that was used for testing is the enhanced triaxial tester developed by Abdel-Hadi (see Abdel-Hadi *et al*. (2000)). The setup consists of five major components: (1) the triaxial cell that contains the specimen that is isolated by a membrane from the confining fluid and a piston that applies the axial load, (2) low pressure lines, (3) electronic volume change device, (4) data acquisition system, and (5) a universal testing machine. The major enhancement is the volume change device, which is fully automated, requires no human intervention, and is ideally suited for computer data acquisition. The elimination of cumbersome pressure lines yields improved sensitivity, accuracy and reliability. It has a fast response time, which enables it to detect minute or abrupt changes in volume during testing. A schematic diagram of the testing device is shown in Figure 1.1.

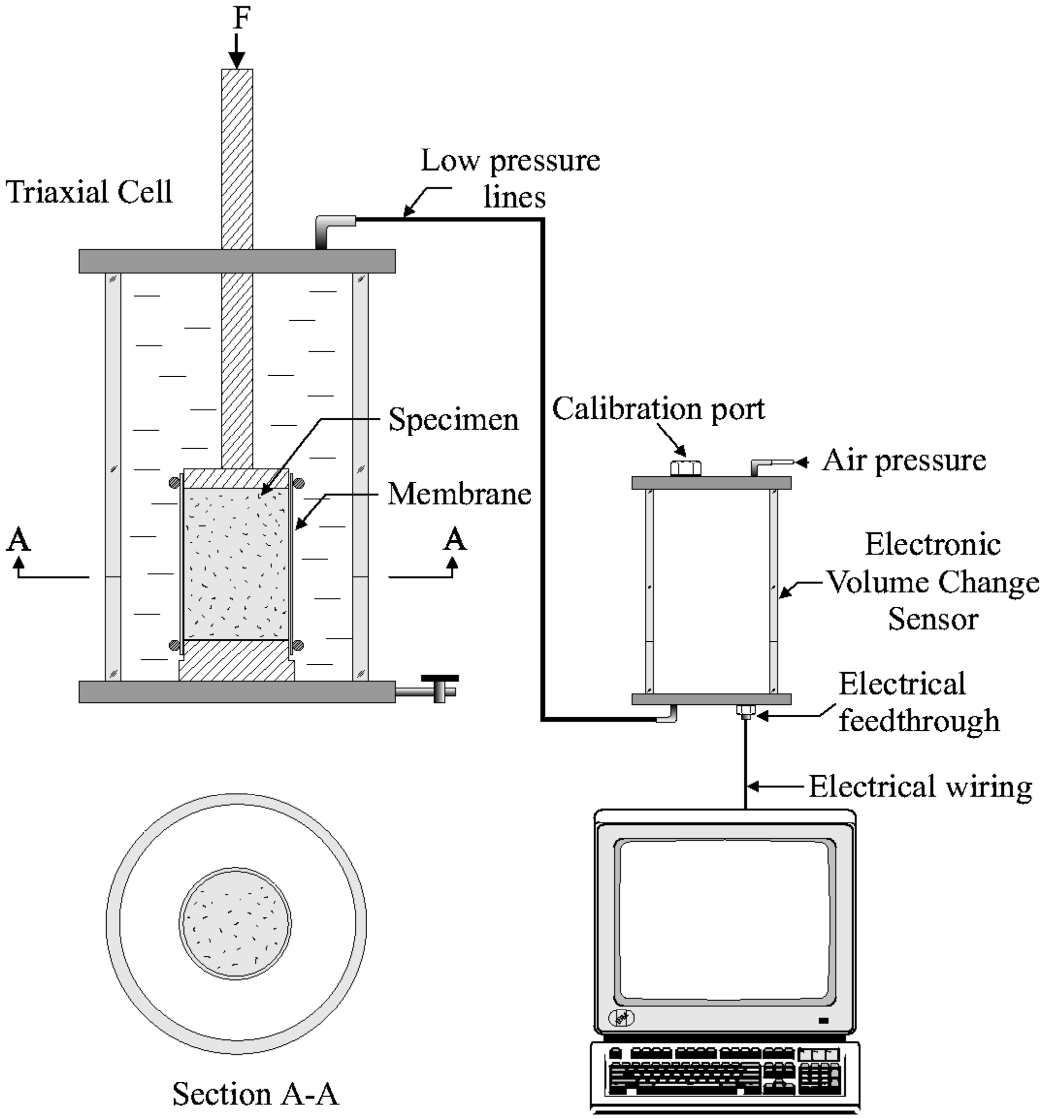
F
Triaxial Cell
Low pressure lines
Specimen
Membrane
A
A
Calibration port
Air pressure
Electronic Volume Change Sensor
Electrical feedthrough
Electrical wiring
Section A-A

Figure 1.1: Schematic diagram of the triaxial tester and new volume change device

A typical test on any system was conducted as follows:

(i) Sample preparation

A latex membrane of 0.3 mm in thickness was stretched around a cylindrical split mold and kept in place by applying vacuum. The mold was sealed by rubber O-rings to a pedestal at the bottom, and to a cap at the top. The material was poured into the mold in successive layers and pre-compacted using an integrated compaction device that can be attached to the split mold. This new device is shown in Figure 1.2. Each layer was thus pre-compacted by a specific amount by adjusting the drop height and the drop weight of the pre-compaction device. In this way, it was ensured that the anisotropy induced by the filling procedure is negligible and that all the specimens are pre-compacted to approximately the same density. The assemblage was then placed in a triaxial compression cell having a maximum compression capacity of 3400 kPa. The cell was filled with water, and then placed on the load cell of an Instron 5566 testing machine.

(ii) Testing protocol

Any test consisted of 2 stages: (1) hydrostatic and (2) deviatoric. In the hydrostatic part of the test, the specimen was subjected to an all-around pressure that was gradually increased up to a predetermined level, say σ_3. The quantities measured during the hydrostatic part of the test were: (1) the applied pressure, (2) the change in the volume of the sample, which was determined by the change in the volume of water used to compress the specimen (Abdel-Hadi et al. (2000)). Once the desired level of confining pressure σ_3 was reached, the lateral pressure was kept constant while an axial load was applied to the sample through the loading piston (deviatoric part of the test). Both axial and volumetric strains were continuously recorded. All tests were conducted in a thermostatically controlled air-conditioned laboratory with minimal ambient changes, the recorded temperatures and relative humidity being 25°C and 45%, respectively.

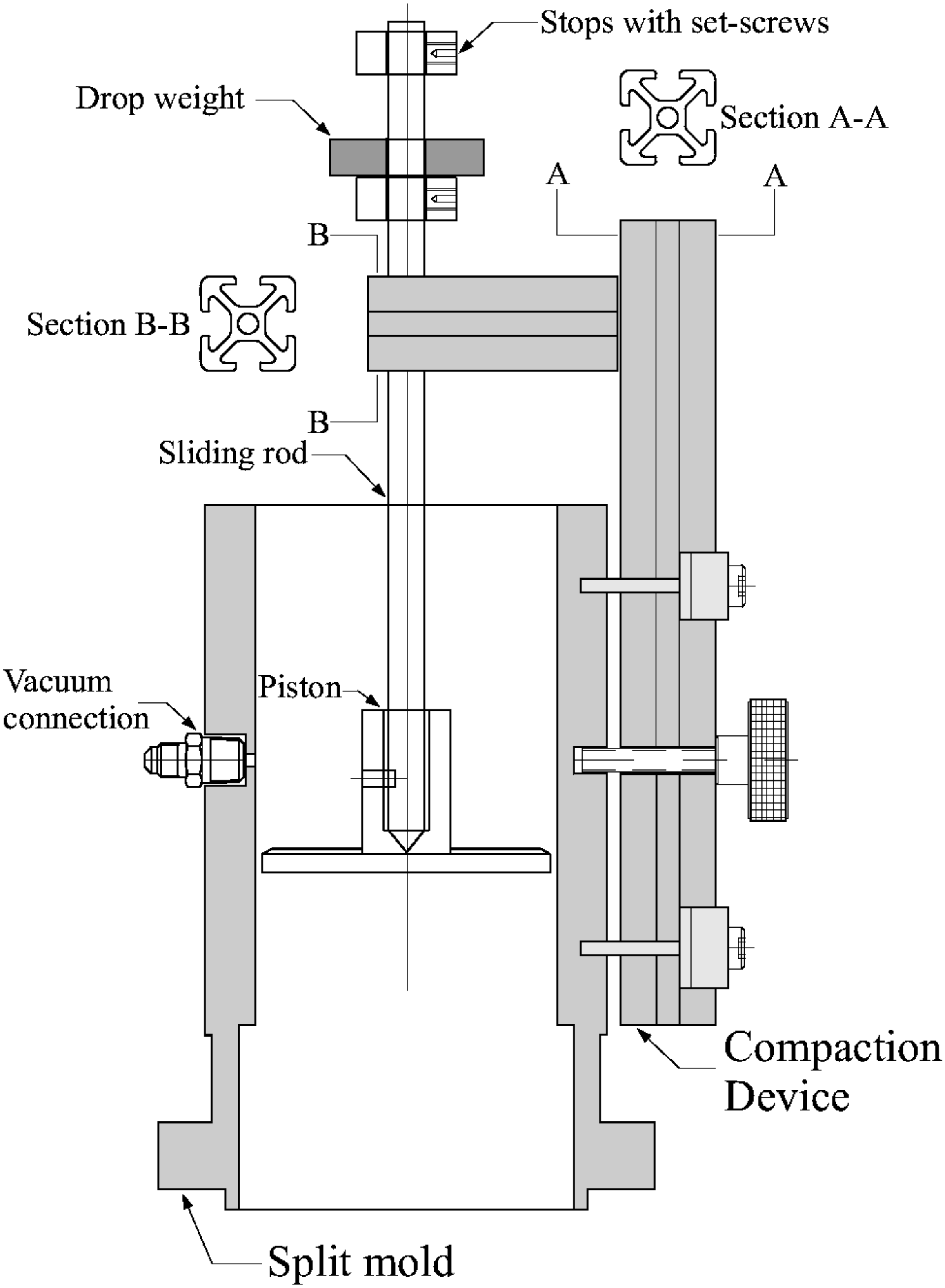
Stops with set-screws
Drop weight
Section A-A
A
A
B
Section B-B
B
Sliding rod
Vacuum connection
Piston
Compaction Device
Split mold

Figure 1.2: Device and split mold for controlled pre-compaction of the particulate systems prior testing.

I.3. Experimental Results on Silica Powder

I.3.1. Material Characteristics

The silica powder (silicon dioxide, floated powder) under study is monosized with a mean particle size of 63.5 μm or 240 mesh. The geometrical configuration and surface structure of the system is shown in an SEM (scanning electron microscope) micro-graph (see Figure 1.3). The particle density was about 2.3 g/cm^3 and the initial density of the powder was about 1.3 g/cm^3. Although this system is fairly well characterized in terms of surface chemistry, the available information concerning its mechanical behavior is limited. Another rationale for studying this system rather than sand is because it is monosized and all particles have the same geometry so we could separate the effects of particle size distribution and geometry from that due to confinement on the compaction of the material. Here and throughout the text compressive stresses and strains are considered positive.

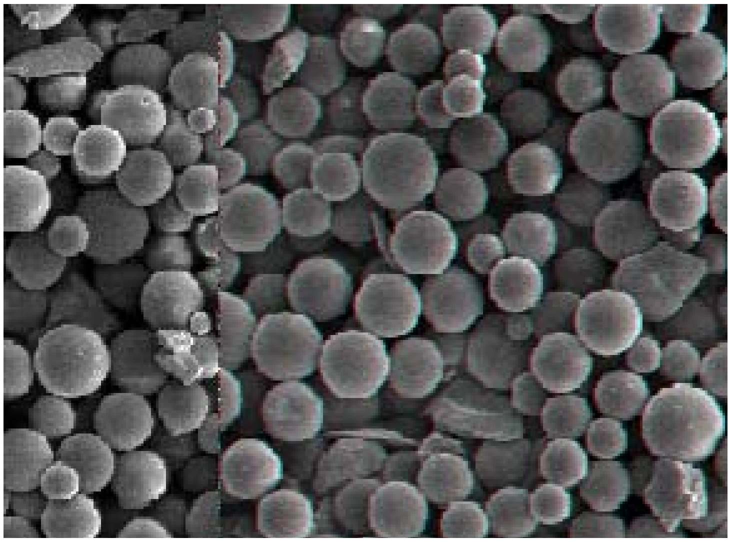

Figure 1.3: SEM micrograph of monosized silica of of 63.5 μm mean particle size (or 240 mesh).

Monotonic triaxial compression tests under lateral confining pressure σ_3 in the range 20 kPa to 350 kPa and cyclic triaxial compression tests consisting of several loading-creep-unloading and reloading cycles under the same confining pressures were conducted. These tests allowed the measurement of both the deformability and strength characteristics. Measurements of the volume changes of the sample as a function of the applied stress were used to determine the evolution of the bulk modulus i.e. compaction characteristics of the material as well as the yield behavior under 3-D stress conditions.

I.3.2. Monotonic Test Results on Silica Powder

To gain a fundamental understanding of the compaction properties of the material, the experimental program included monotonic triaxial compression tests under lateral confining pressure, σ_3 in the range 20 kPa to 350 kPa; the crosshead displacement rate was 0.1 mm/min. A slip-stick phenomenon is observed (sudden reduction in material strength) at the beginning of the tests for the very low confining pressures.

Typical results of a hydrostatic compression test up to 350 kPa are shown in Figure 1.4. As an example of a deviatoric test, the stress-strain curves (i.e. axial and volumetric strain vs. the stress difference $\sigma_1 - \sigma_3$) obtained under a confining pressure $\sigma_3 = 93$ kPa are shown in Figures 1.5 (a) and (b). The initial density of the sample was $\rho_i = 1.33$ g/cm^3. The stress versus axial strain curve presents 3 regions: (1) quasi-linear elastic, (2) concave towards the strain axis, (3) plateau. In the first part (up to 200 kPa), the behavior can be considered to be elastic (the irreversible strains are small in comparison to the elastic, recoverable strains). In the second region, the plastic deformation undergone by the material is significant and the value of the yield limit continuously increases up to failure at $\sigma_d = \sigma_1 - \sigma_3 = 320$ kPa. The existence of a plateau shows that the material has viscous (viscoplastic) properties, that is, it deforms even under constant stress.

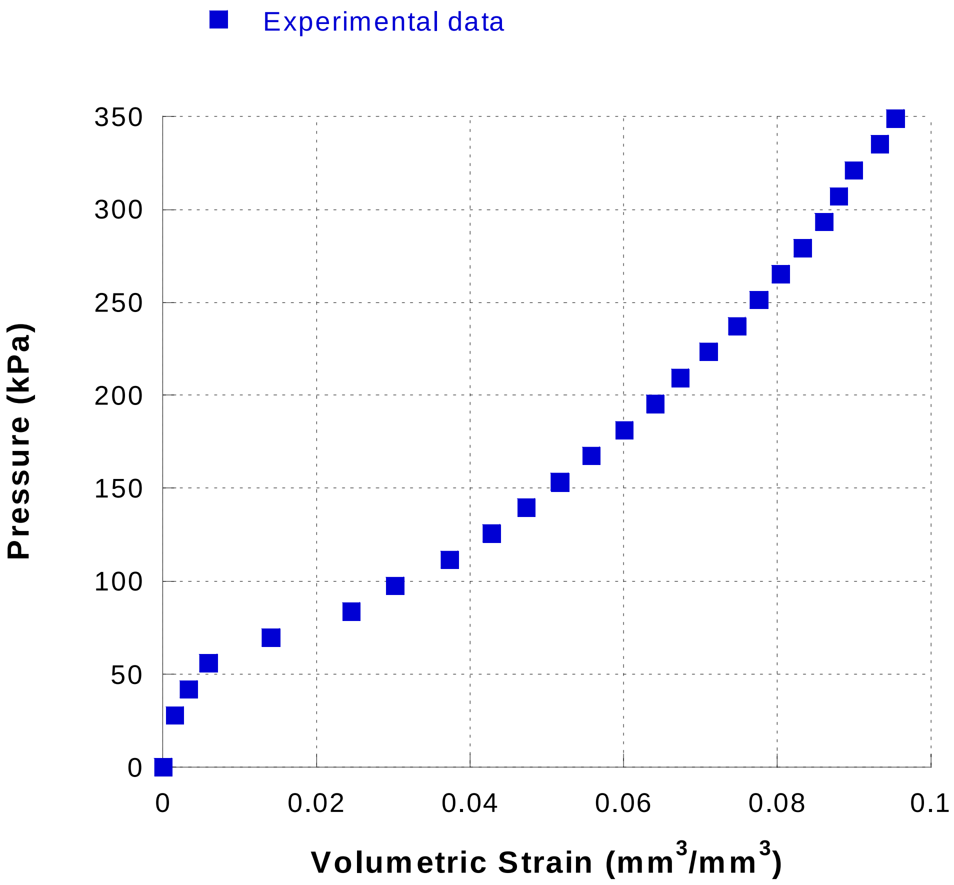

Figure 1.4: Pressure vs. volumetric strain response under hydrostatic compression for silica.

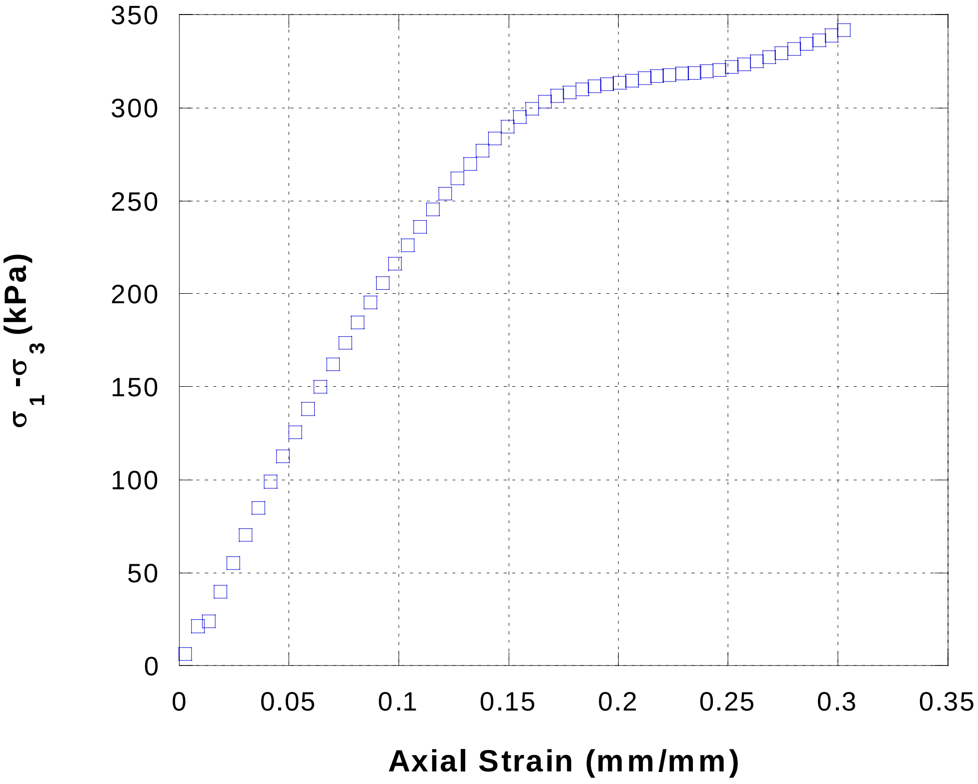

Figure 1.5(a): Deviatoric stress vs. axial strain at 93 kPa of confining pressure.

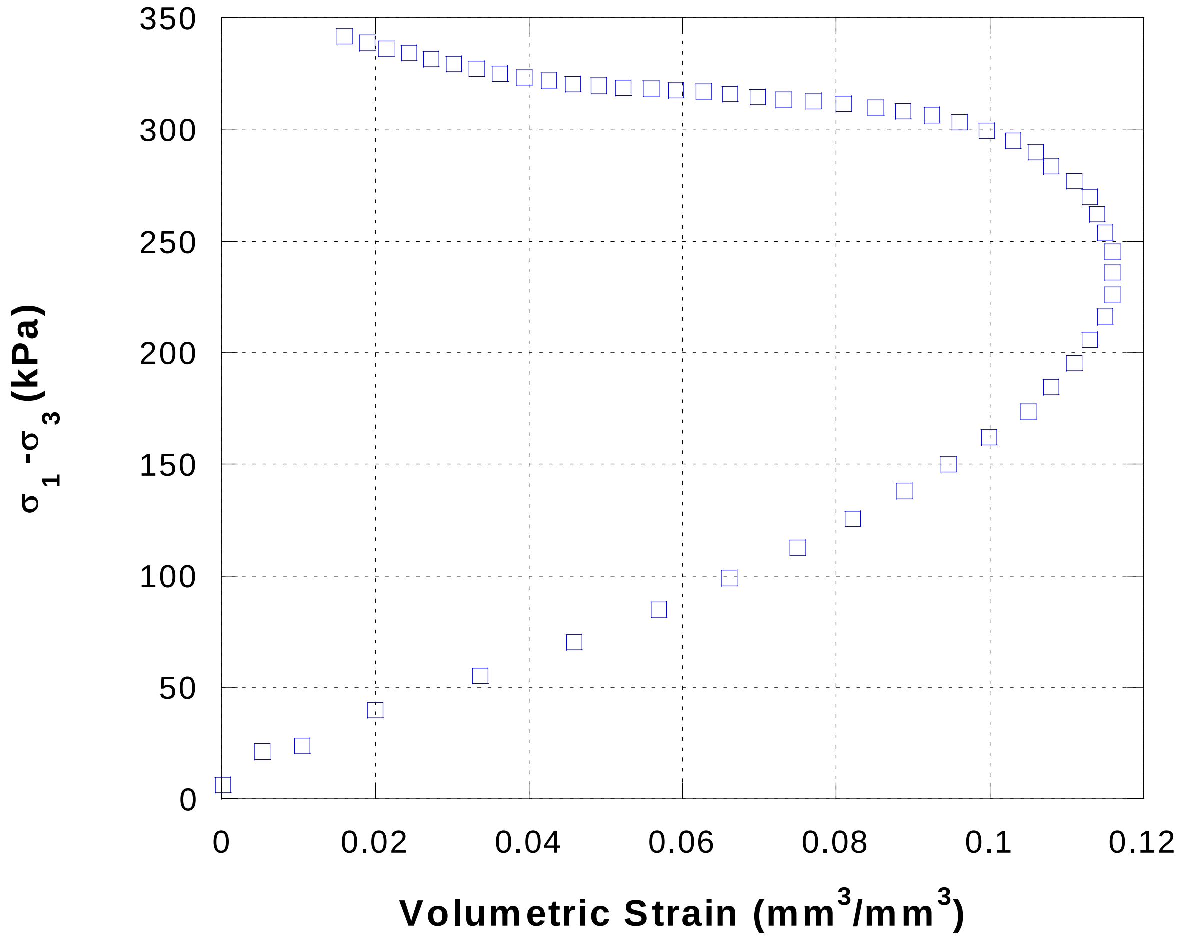

Figure 1.5(b): Deviatoric stress vs. volumetric strain at 93 kPa of confining pressure.

The stress-volumetric strain curve, indicates that the material undergoes further compaction under deviatoric conditions, and then dilates (see Figure 1.5(b)). The existence of those two regimes of volumetric behavior was observed in all tests. Figure 1.6 shows the volumetric profiles obtained in tests under confinement levels of 40 kPa, 70 kPa, and 93 kPa.

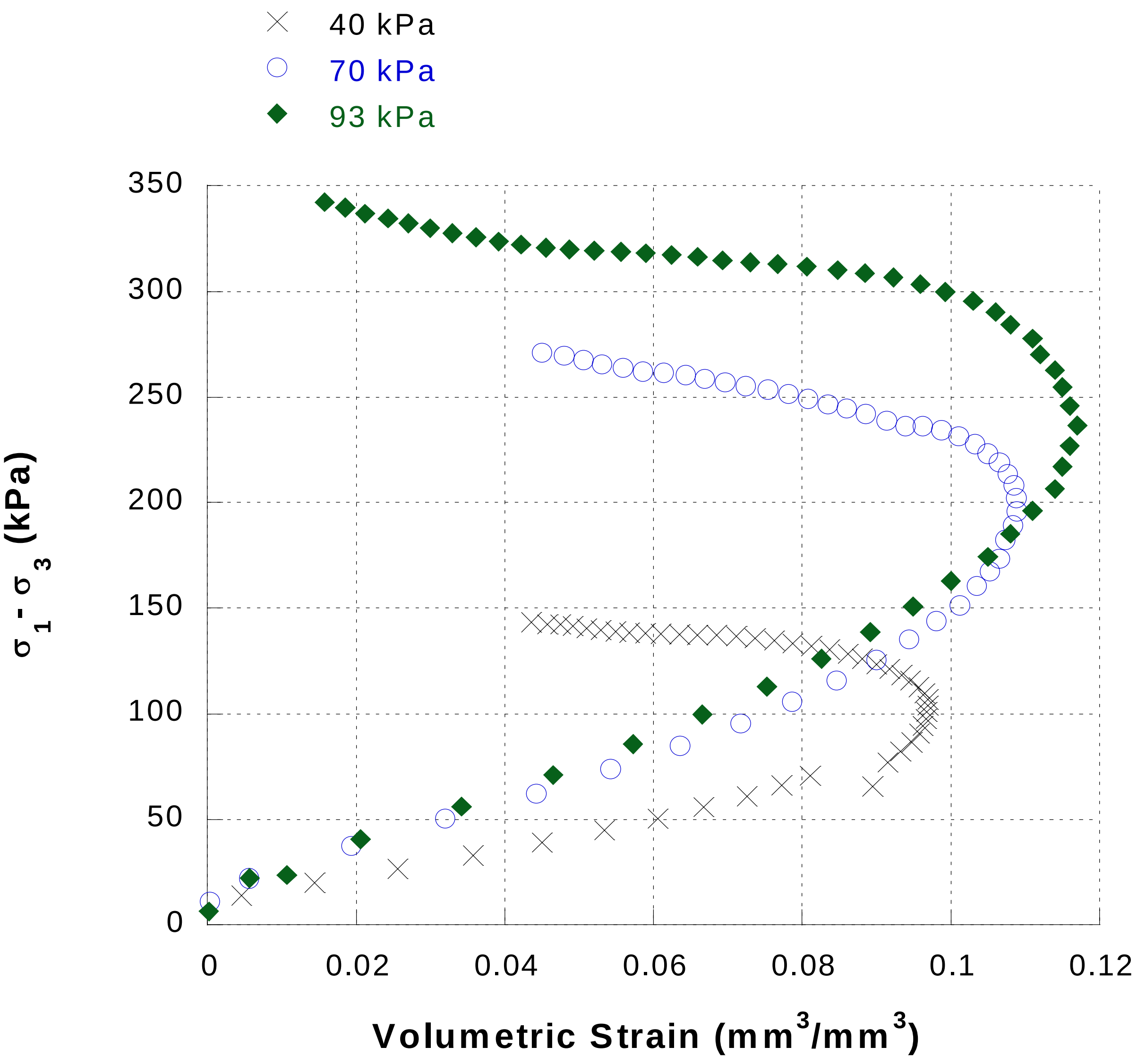

Figure 1.6: Volumetric strain profiles at confining pressures of 93 kPa, 40 kPa, and 70 kPa

It is clear that the usual decoupling between the deviatoric and hydrostatic responses that is usual in constitutive models belonging to the commercial finite element software for transient analyses such as LS-DYNA cannot be considered in the case of silica.

Note that the stress value for which the curve $\sigma_1 - \sigma_3$ versus the volumetric deformation ε_V changes sign depends on the confining pressure. These critical points define the boundary between the compressible and dilatant regimes. As is the case with most particulate systems, the strength of the material is an increasing function of the applied confining pressure. Figure 1.7 shows the deformed specimen at the end of a deviatoric test under 70 kPa confining pressure.

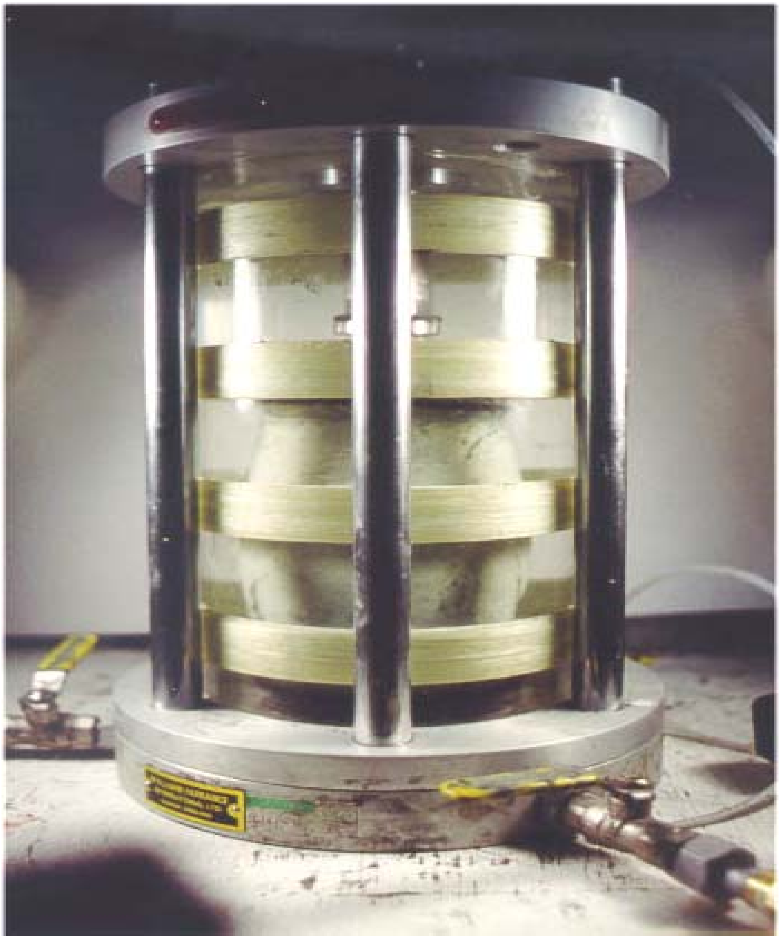

Figure 1.7: Triaxial compression cell with deformed specimen.

I.3.3. Cyclic Test Results on Silica Powder

To characterize the influence of the loading history and time effects on the response of silica, cyclic confined compression tests were also performed for the same confining pressures as in the monotonic tests. The results obtained in a test under 27 kPa confining pressure are shown in Figures 1.8 (a) to 1.8 (c). The test consisted of five loading-unloading and reloading cycles. Before passing from loading to unloading the load was held constant for about 20 minutes in order to separate possible viscous effects from unloading. Then, unloading and further reloading was performed. From the unloading slopes of $\sigma_1 - \sigma_3$ versus ε_1, the Young modulus **E** was determined. A dependence of **E** on the mean stress $p = \frac{\sigma_1 + 2\sigma_3}{3}$ is observed. From the unloading slopes of $\sigma_1 - \sigma_3$ versus ε_V curves, the bulk modulus **K** was evaluated. As an example, in Table 2 are given the values of the elastic moduli determined from data obtained in a cyclic triaxial compression test under a confining pressure of 27 kPa.

Cycle Number	**E (MPa)**	**K (MPa)**
1	63.500	168
2	57	161
3	63	181
4	70.4	195.35
5	97.04	254.34

Table 1.1. Elastic constants as determined from data obtained in a cyclic triaxial compression test on silica under confining pressure of 27 kPa.

Note also a change in the creep direction at the transition from the compaction regime to the dilatancy regime. This effect can be clearly seen in a zoom of the stress-volumetric strain curve shown in Figure 1.8 (c).

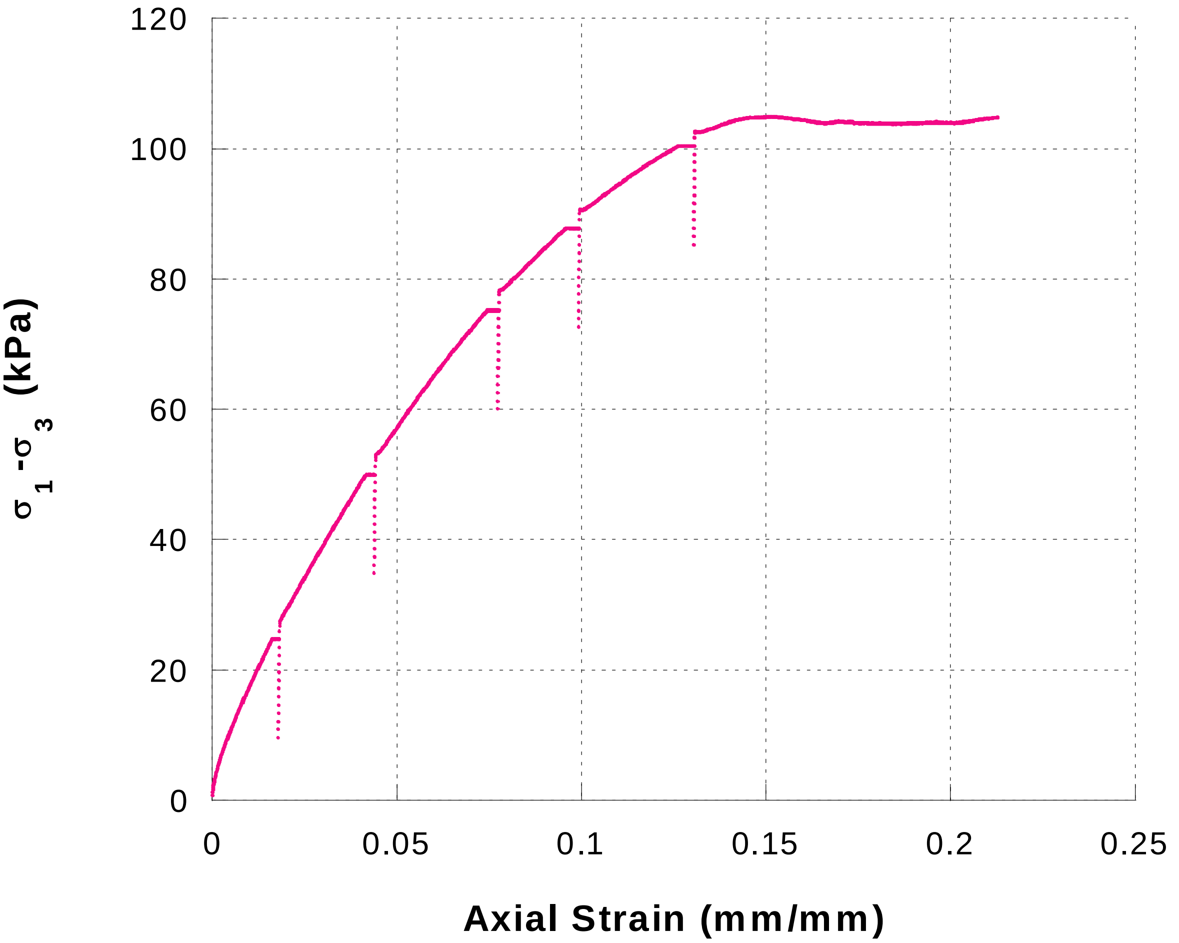

Figure 1.8(a): Deviatoric stress vs. axial strain curve in a cyclic test under 27 kPa confining pressure.

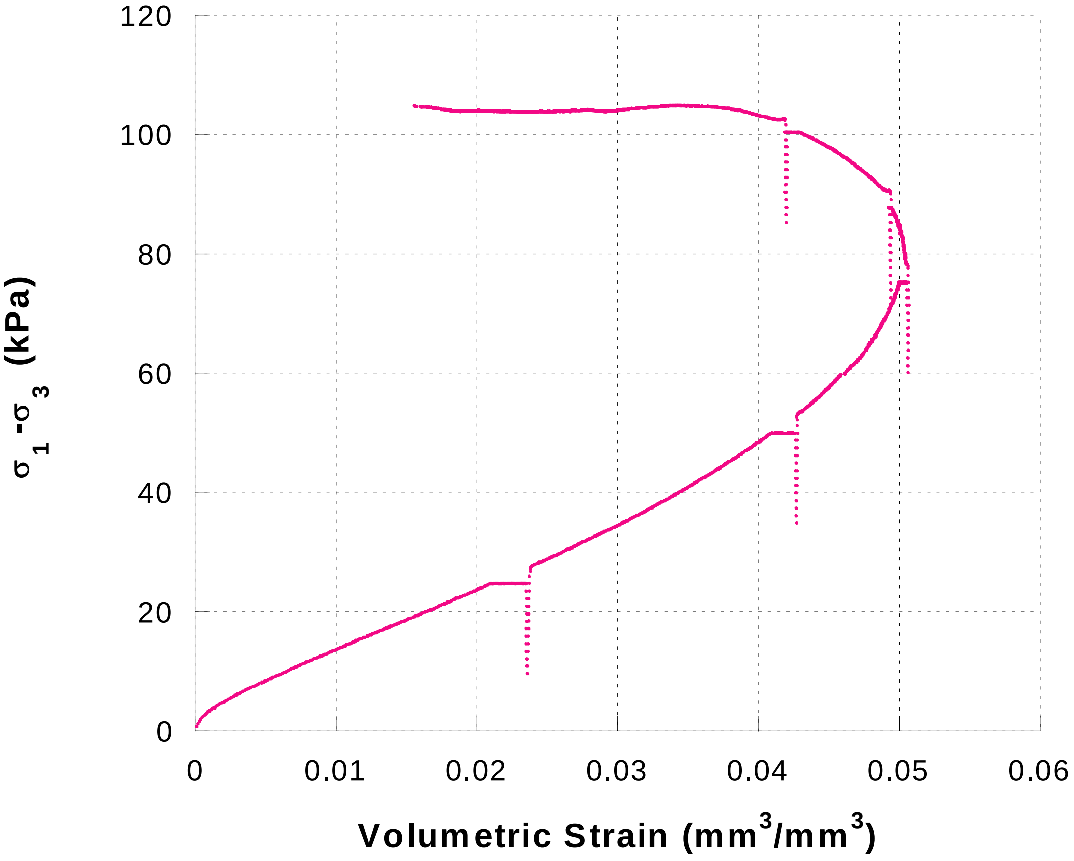

Figure 1.8(b): Deviatoric stress vs. volumetric strain in a cyclic test under 27 kPa confining pressure.

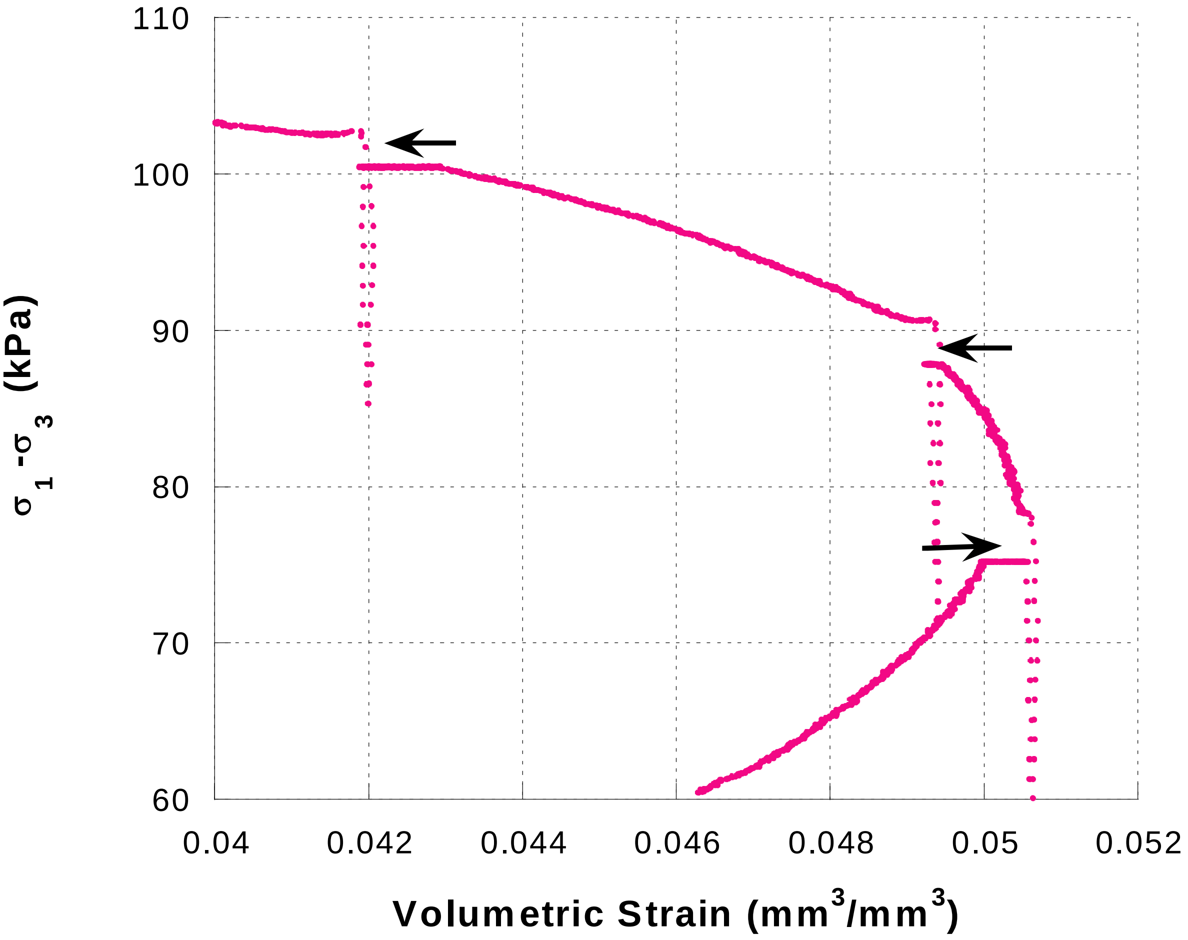

Figure 1.8(c): Zoom in of the deviatoric stress vs. volumetric strain curve in a cyclic test under 27 kPa confining pressure showing the change in creep direction during transition between the compressibility and dilatancy regime.

I.4. Experimental Results on Polyethylene Pellets

I.4.1. Material Characteristics

In this subsection, we present the results of a series of triaxial compression tests conducted on commercially available dry PE pellets. The composition of the pellets is: polyethylene > 99% and talc < 0.1%-1.0%. Their appearance is translucent, white and soft. In general, the pellets are uniform and cylindrical in shape (4 millimeters in height by 3 millimeters in diameter). The pellet density is 0.91 g/cm^3, while the initial density of the PE system varied from 0.59-0.63 g/cm^3.

I.4.2. Monotonic Test Results on Polyethylene Pellets

Typical results of a hydrostatic compression test up to 350 kPa on polyethylene pellets (PE) are shown in Figure 1.9. It can be concluded that the behavior of PE pellets under isotropic compression is linearly elastic within the pressure range considered.

A series of monotonic triaxial compression tests were performed for confining pressure in the range of 14.7 kPa to 35 kPa; the crosshead displacement rate was of 0.1 mm/min. For illustration purposes, we present the test results of the experiments under confining pressures at the extremes of the pressure range. In Figure 1.10 (a) the stress-axial strain curves are shown. It can be noted that the stress-strain response is non-linear. For a given confining pressure, the material underwent elastic deformation followed by irreversible deformation and failure. The corresponding stress-volumetric strain curves (Figure 1.10 (b)) show two distinct regimes of behavior: (1) a compressibility regime, followed by (2) a dilation regime. The occurrence of both regimes of volumetric behavior was observed in all tests in the given range of confining pressures. Figures 1.10(a) and (b) also show the effect of the confining pressure on the overall response, *i.e.* the higher the confining pressure, the higher the yield limit, dilatancy threshold, and strength. An increase of confining pressure of 138% from 14.7 to 35 kPa resulted in an increase of 123% in compressive strength and of 120% in the dilatancy threshold level. However, for any given confining pressure the dilatancy threshold level corresponds to about 75% of the compressive strength.

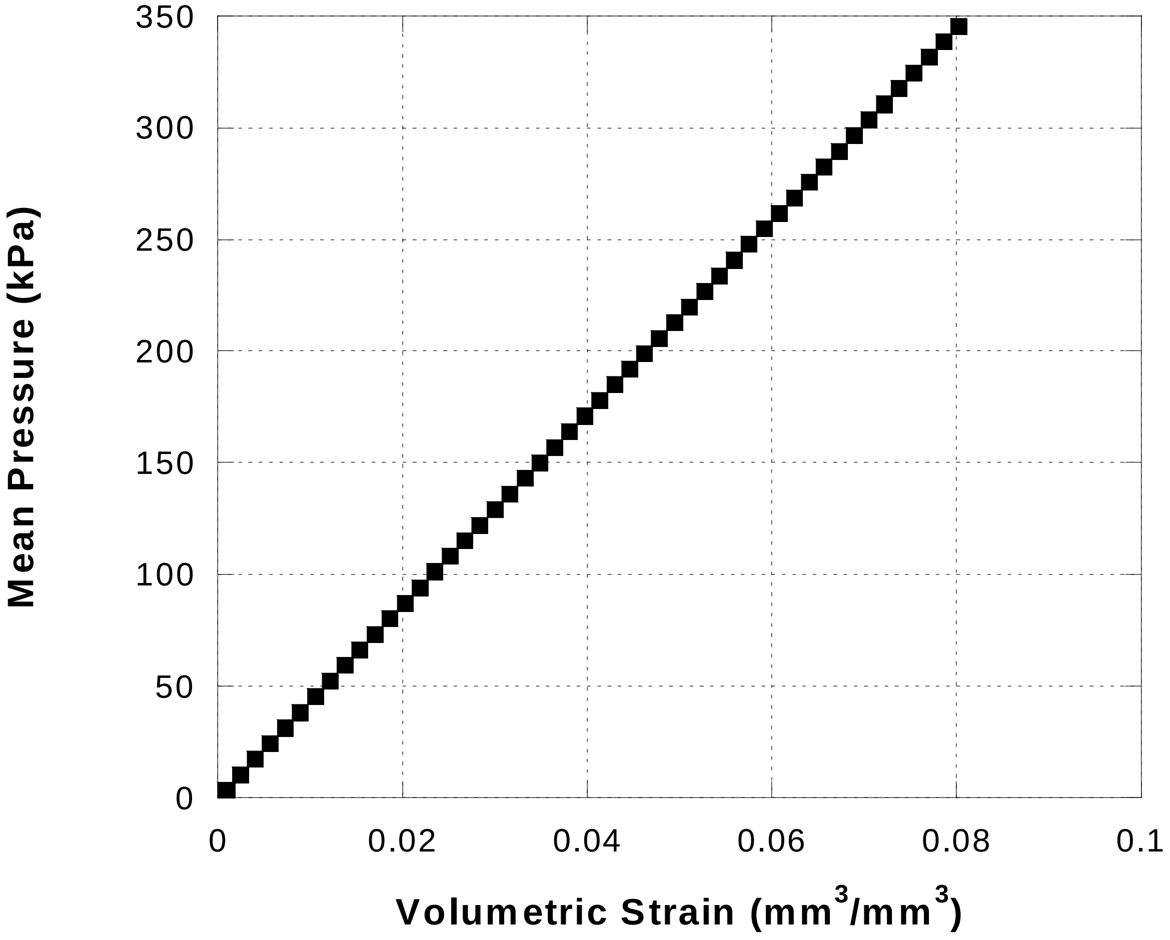

Figure 1.9: Pressure vs. volumetric strain response under hydrostatic compression for PE pellets.

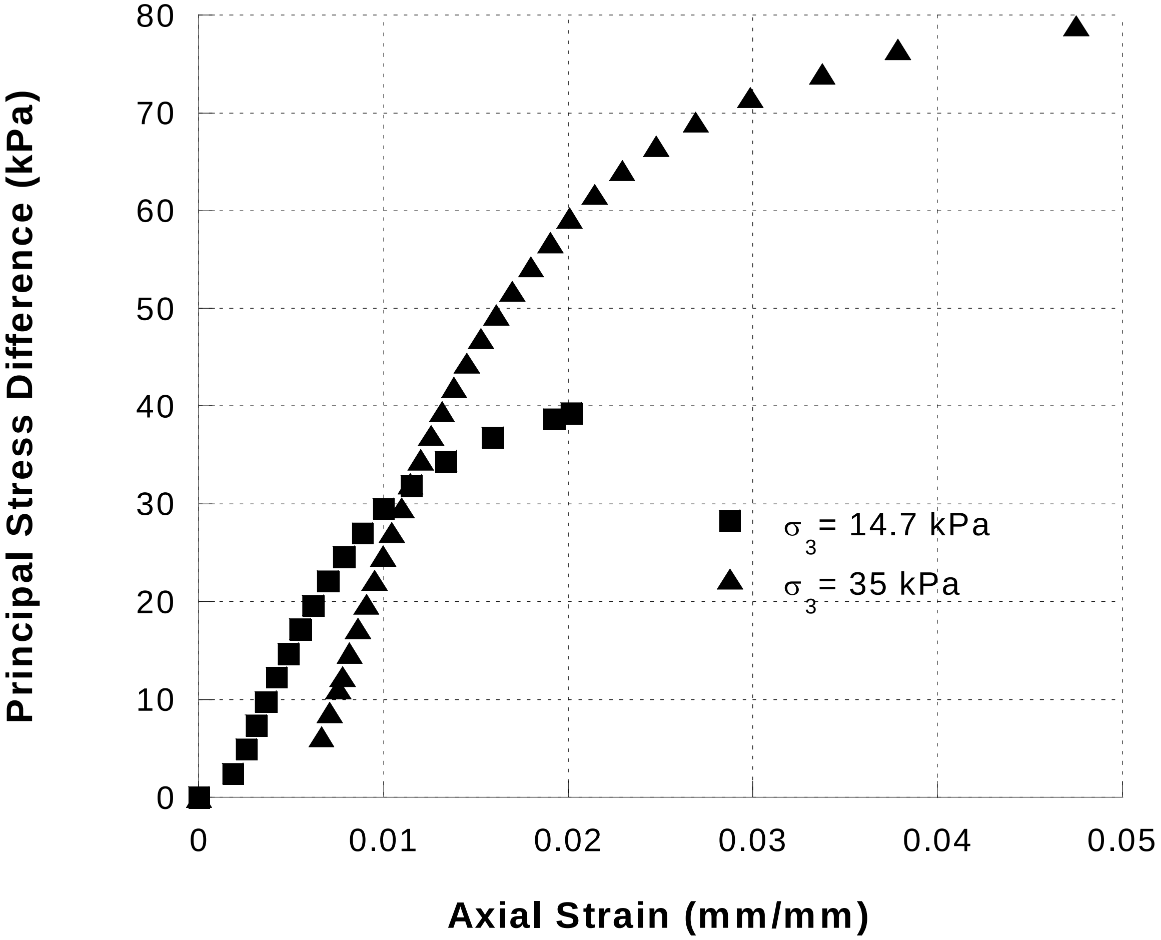

Figure 1.10(a): Stress - axial strain curves showing the effect of confining pressure on the behavior of polyethylene pellets.

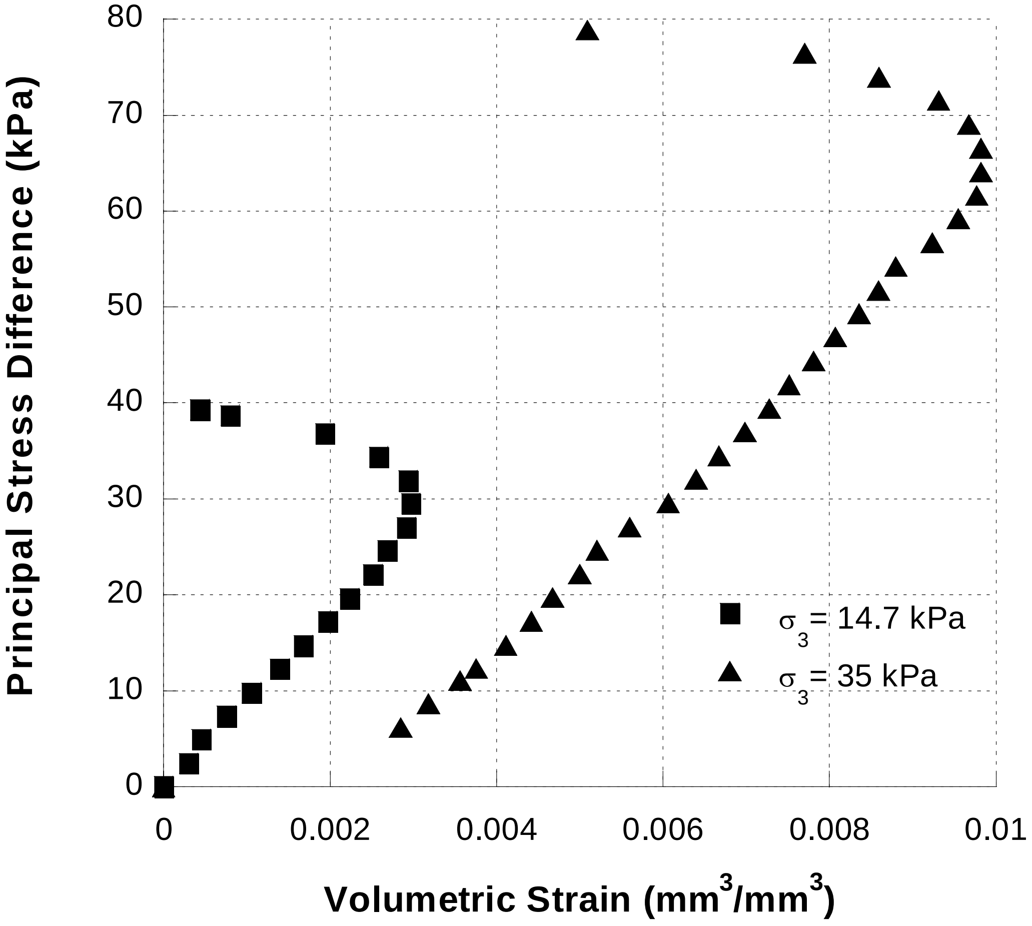

Figure 1.10(b): Stress-volumetric strain curve showing compressibility followed by dilatancy.

Strain rate sensitivity

Figures 1.11 show the results of a standard triaxial compression test at $\sigma_3 = 35$ kPa and 0.1 and 10 mm/min strain rates, respectively. A clear rate sensitivity of the overall response can be noted: an increase in strain rate results in steeper slope of the stress-strain curve, higher dilatancy threshold, more dilatancy, and higher strength (a 1.25 fold increase in strength as a result of a hundred-fold increase in the strain rate).

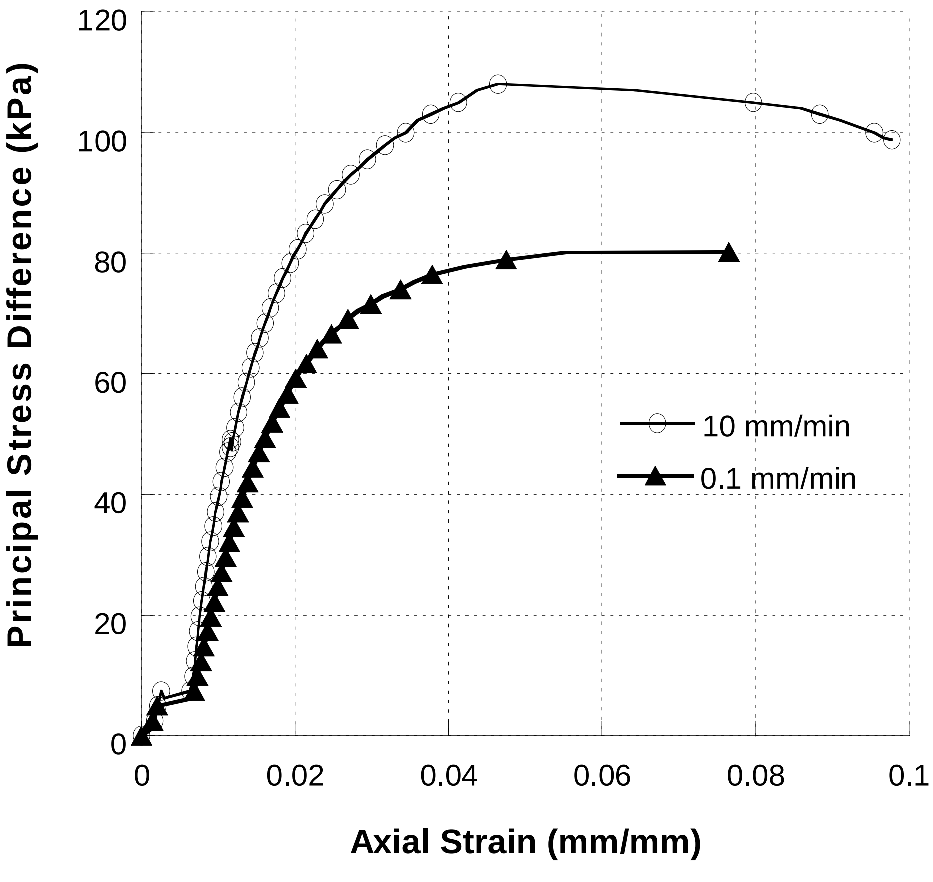

Figure 1.11(a): Stress-axial strain curves in monotonic triaxial compression test at $\sigma_3 =$ 14 kPa showing the strain rate sensitivity of polyethylene pellets;

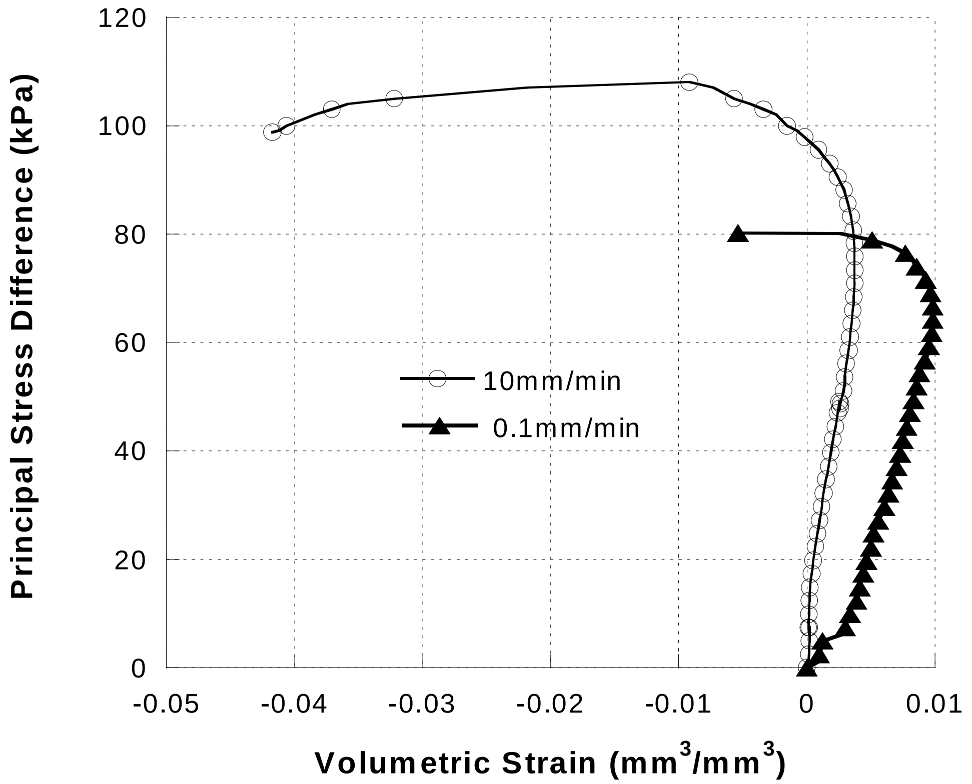

Figure 1.11(b): Stress- volumetric strain curves in monotonic triaxial compression test at σ_3 = 14 kPa showing the strain rate sensitivity of polyethylene pellets.

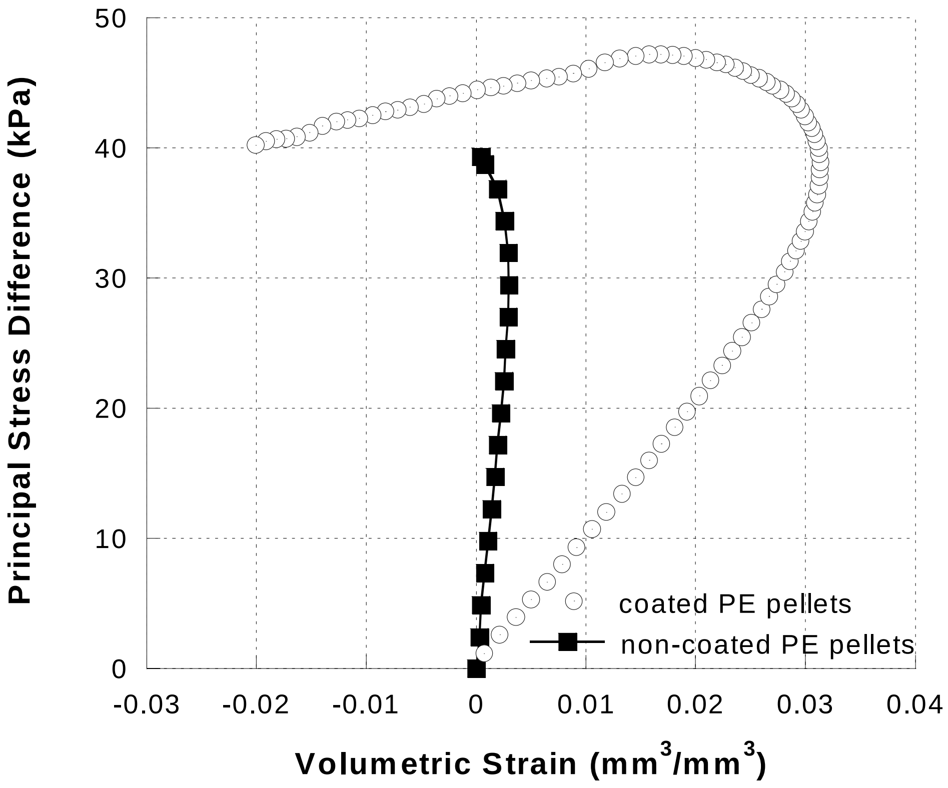

Figure 1.12: Comparison between the volumetric stress-strain behavior of coated and non-coated polyethylene pellets showing that the coated system exhibits much more dilatancy and thus improved flowability.

Coated vs. non-coated pellets behavior:

The stress-strain response of a coated ethylene and styrene copolymer sample in pellet form was investigated and compared to the behavior of non-coated polyethylene pellets (see Figure 1.12). The results show that although the dilatancy threshold is the same for both systems, the coated sample exhibits much more dilatancy. Thus, the enhanced triaxial tester provides an excellent means for comparing the flowability of different systems.

I.4.3. Cyclic Test Results on PE pellets

To characterize the influence of the loading history and time on the response of the material, cyclic confined compression tests were also performed for the same confining pressures as in the monotonic tests. As an example, in Figures 1.13 (a) and (b) are shown the results of a test corresponding to σ_3 = 35 kPa. The test consisted of four loading-creep- unloading -reloading cycles. Note that before unloading, the axial load was held constant. The material deformed by short-term creep, which appeared to stabilize in 15-20 minutes. Then, partial unloading and further reloading was performed. A change in creep direction at the transition from the compressive to the dilatancy regime was observed(see Figure 1.14). Lastly, note the absence of hysteresis loops and that the unloading curves are quasi-linear. The Young's modulus E was determined from the slopes of $(\sigma_1 - \sigma_3)$ versus axial strain (ε_1) curves during unloading. A dependence of E on stress state was observed (see Figure 1.13 (a)). Similarly, the bulk modulus, K was evaluated from the unloading slopes of deviatoric stress vs. volumetric strain curves and its variation with the stress level is indicated in Figure 1.13 (b). A variation of both elastic parameters with stress was observed in all tests.The mean arithmetic values calculated from all tests was: E = 27555 kPa and K= 17975 kPa, respectively. It should be noted that the experimental procedure (short-creep prior to unloading) allowed for a very good separation of viscous effects from unloading, and consequently increased accuracy in the estimate of the elastic properties of the material. More details concerning this experimental procedure and its application to a variety of geologic materials can be found in Cristescu and Hunche (1998).

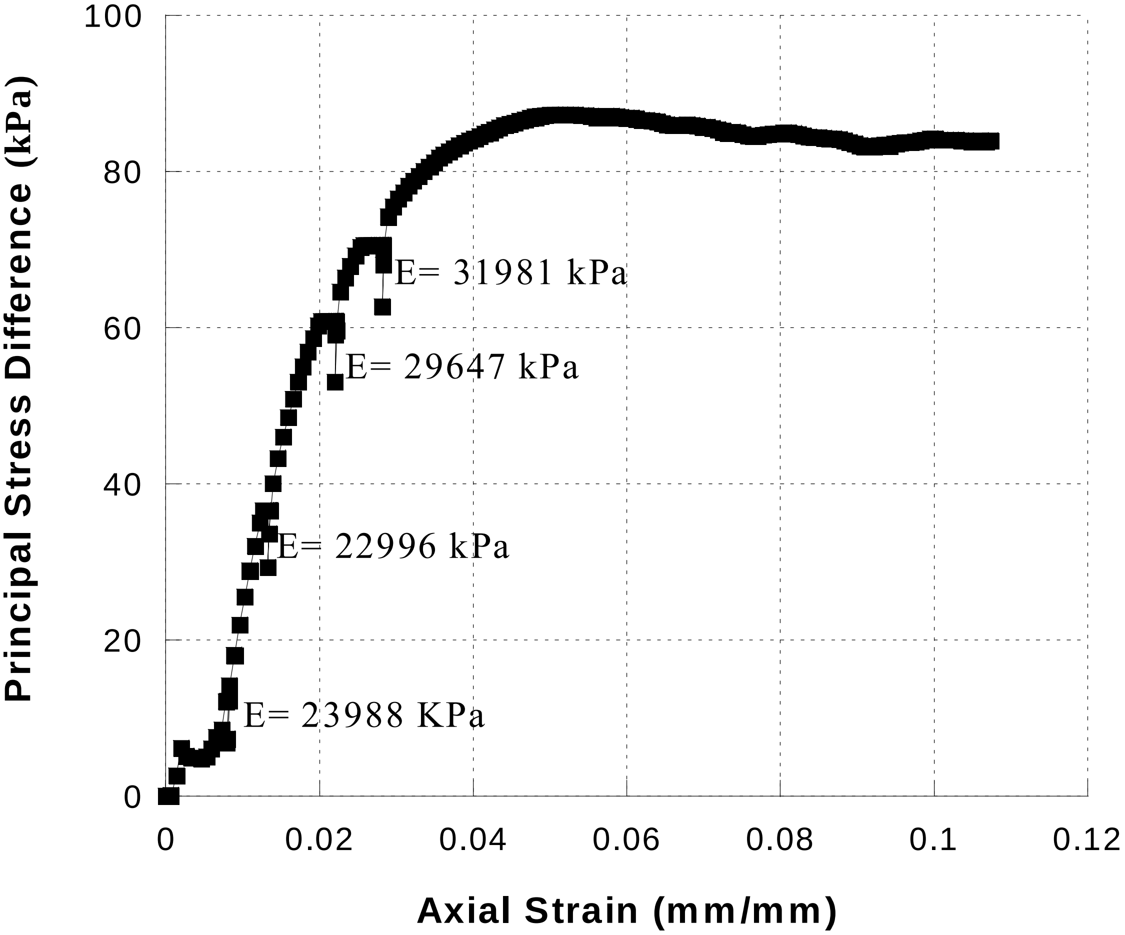

Figure 1.13(a): Stress-axial strain curves in cyclic triaxial compression test at $\sigma_3 = 35$ kPa; before each partial unloading, axial load was kept constant; Young modulus E values computed from the unloading slopes are indicated.

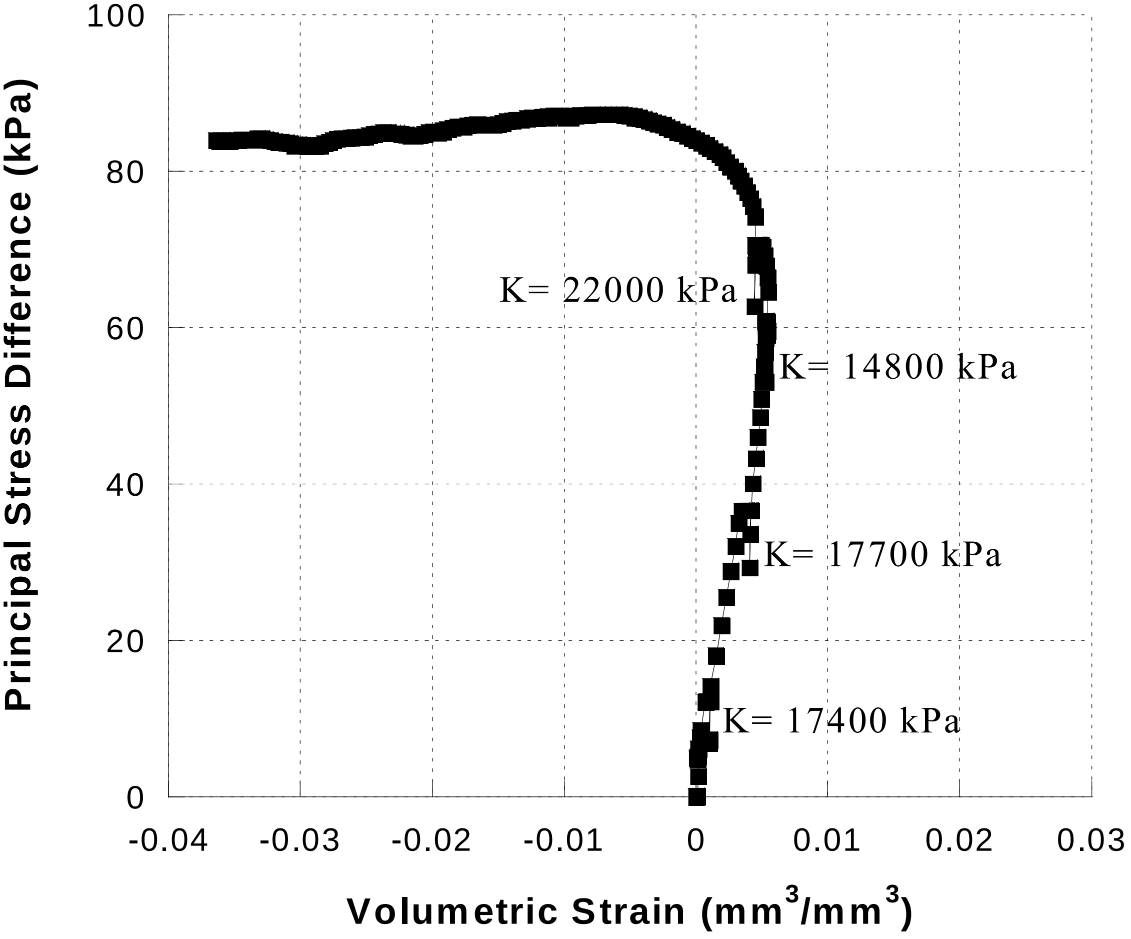

Figure 1.13(b): Stress- volumetric strain curves in cyclic triaxial compression test at $\sigma_3 =$ 35 kPa; before each partial unloading, axial load was kept constant; computed values of the bulk modulus K are indicated

.

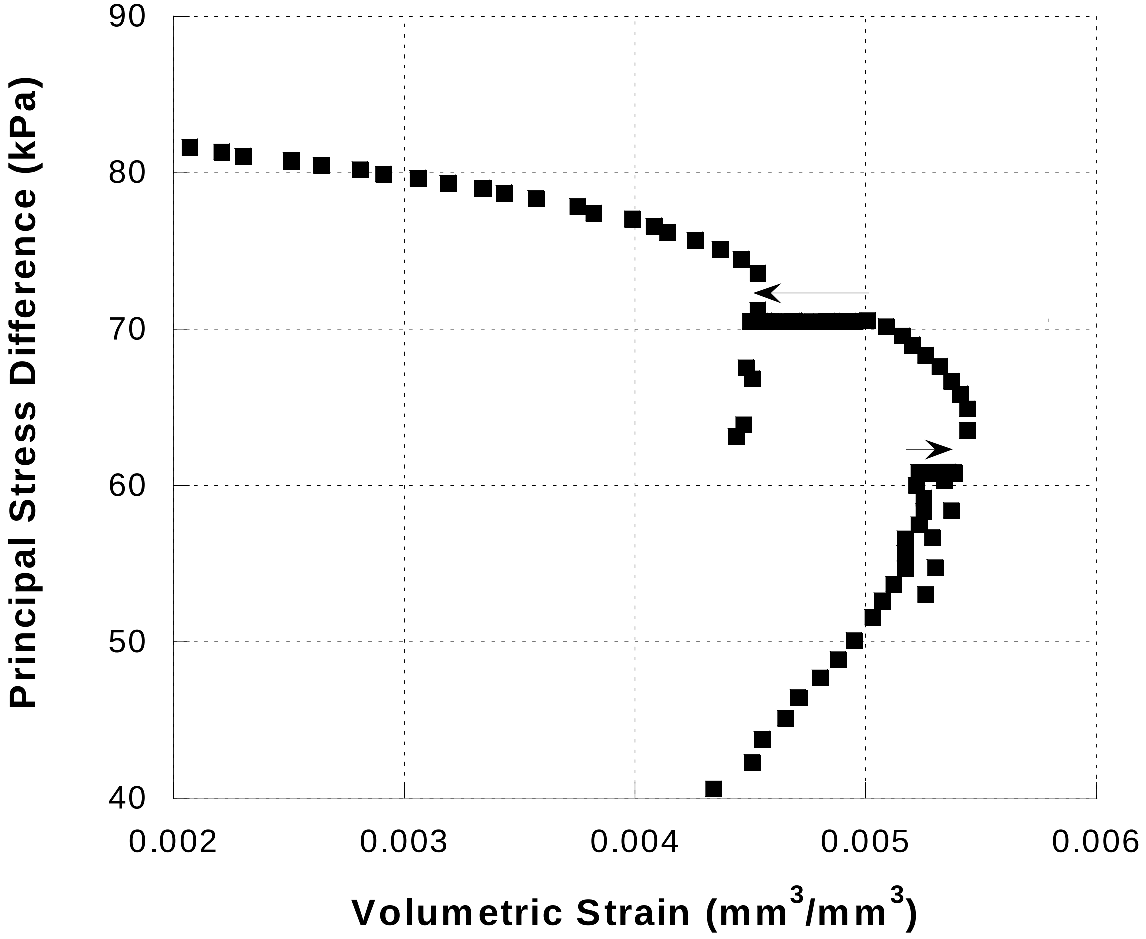

Figure 1.14: Detail of the stress-volumetric strain curve at $\sigma_3 = 35$ kPa showing the change in creep direction as the material transitions from compressible to dilatant behavior.

Stress-path and short-term time effects: Based on the cyclic test results, it can be concluded that the material displays elastic/viscoplastic behavior. The question, which arises, is whether the dominant properties of PE pellets are elastic/plastic or elastic/viscoplastic. In other words, what is the importance of short-term time effects on the response? A comparison between the material response for monotonic and cyclic loading is shown in Figure 1.15. In both tests the crosshead displacement rate during loading was of 0.1 mm/min. It appears that short-term creep effects can be neglected and that an elastic/plastic model could describe accurately the main features of the behavior: non-linearity of the overall stress-strain response, hardening volumetric compressibility/dilatancy, and an influence of the stress invariants on the behavior.

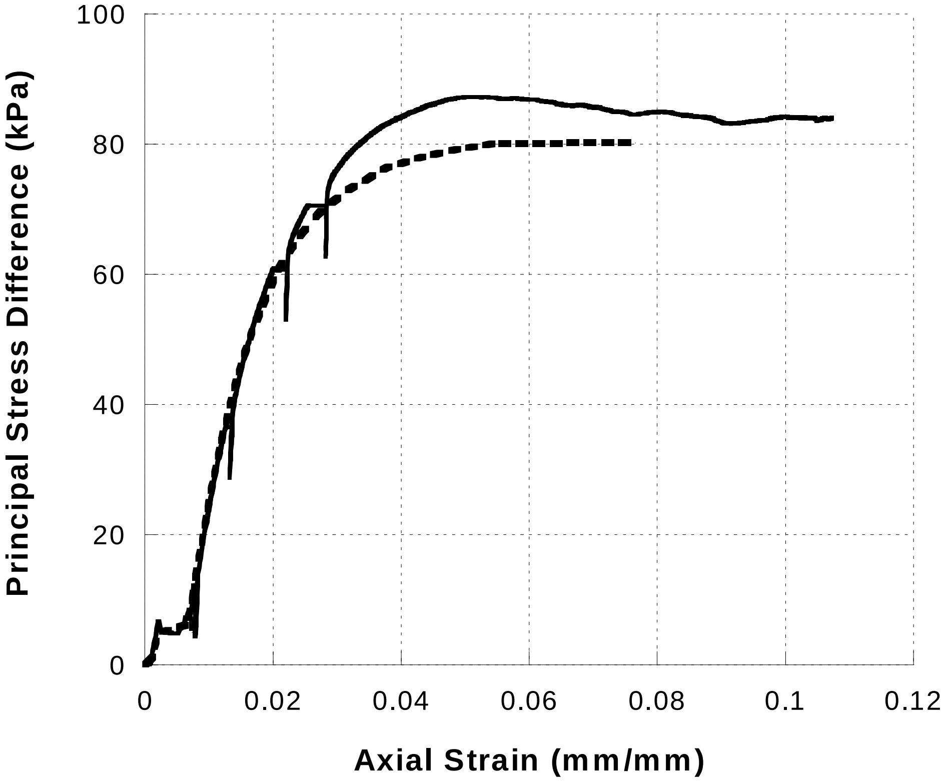

Figure 1.15: Comparison between the stress-axial strain curves at $\sigma_3 = 35$ kPa for monotonic and cyclic loading paths.

I.4.4 Long-term Creep Test on PE pellets

A long-term creep test under confined conditions (lateral confining pressure of 14.7 kPa) was also conducted. The axial load was kept constant at 160 N (σ_1= 52.53 kPa) for 24 hours and both the axial and volumetric strains were continuously monitored. Figure 1.16 (a) shows that the stabilization of the axial strain took place in about 20 minutes. A very interesting evolution in time of the volumetric strain was recorded (see Figure 1.16 (b)).

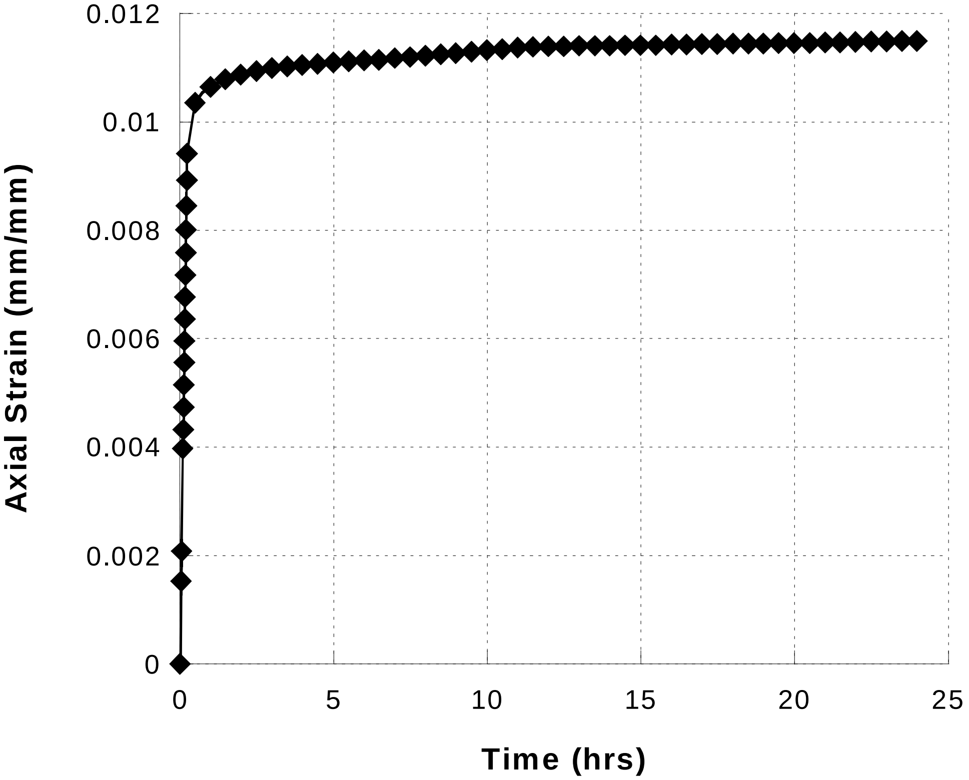

Figure 1.16(a): Evolution of the axial strain with time in a creep test over 24 hours at σ_3= 14 kPa and σ_1 = 52.53 kPa showing that stabilization is reached within 20 minutes.

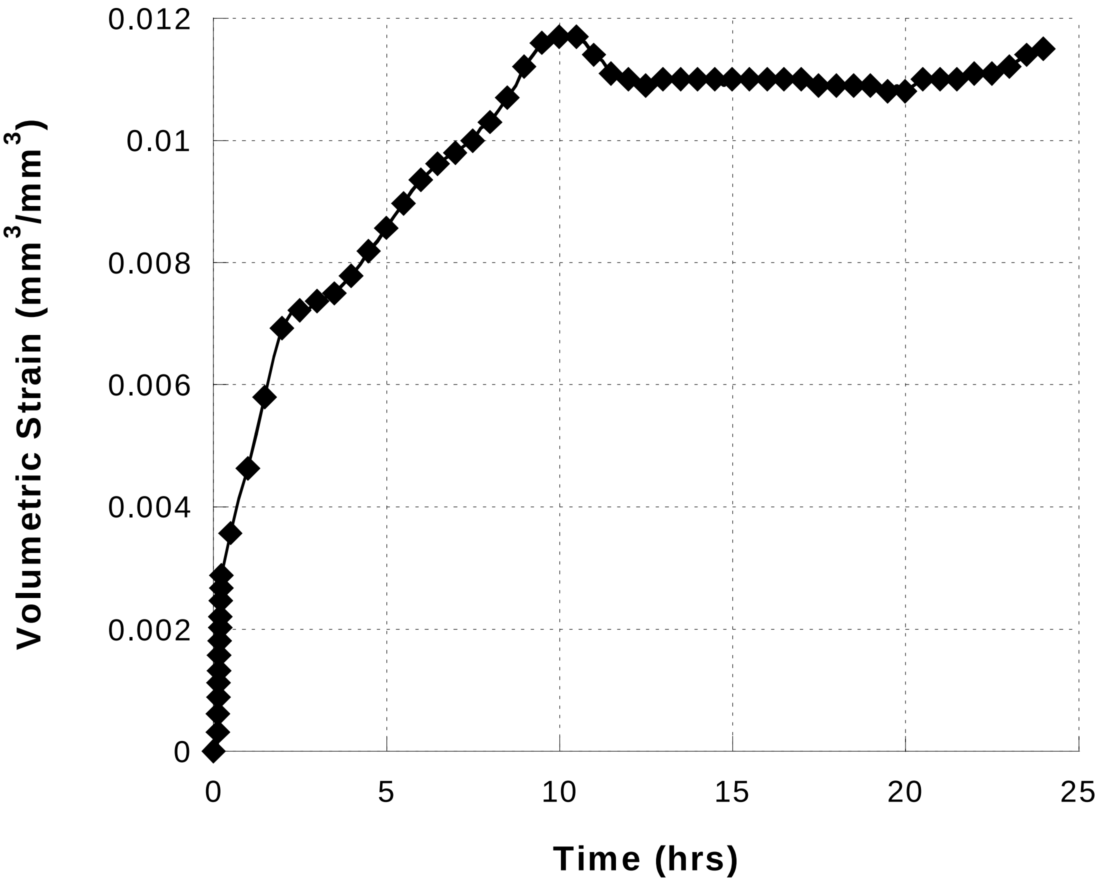

Figure 1.16(b): Volumetric strain versus time curve showing that volumetric creep does not stabilize within the duration of the test (24 hours at $\sigma_3 = 14$ kPa and $\sigma_1 = 52.53$ kPa

Although, it appeared that the volumetric strain stabilizes in 20 minutes, a sharp increase in creep rate was observed between 1-10hrs, followed by a stabilization plateau, and again a change in creep rate after about 20 hrs from the beginning of the creep stage. Stabilization was not reached within the test duration (24 hrs). The test results show a marked difference between axial and volumetric creep behavior. Furthermore, the volume viscosity is not constant, but depends on the current density (or level of compaction). Clearly, such effects cannot be simulated in the framework of the classic theory of viscoplasticity based on the concept of overstress.

I.5. Experimental Results on microscrystalline cellulose

I.5.1. Material Characteristics

The material studied is microcrystalline cellulose, PH-105, $(C_6H_{10}O_5)_n$, mean particle size 20μm. It has a bulk density of about 0.25g/cm^3 and it is highly compressible. This microcrystalline cellulose (MCC) is monosized and has particles spherical in shape. It was tested to provide information on the role of particle size into the deformation and strength through comparison with the test results on silica (see Section I.3.).

I.5.2. Test Results on microcrystalline cellulose

Hydrostatic cyclic tests with several loading-creep-unloading-partial reloading cycles up to a pressure of 275.8 kPa were performed. The average value of the bulk modulus was determined to be of 245 kPa. A series of monotonic and triaxial compression tests were conducted for confining pressures ranging from 68.9 kPa to 275.8 kPa. As an example, in Figure 1.17 are shown the deviatoric stress-volumetric strain curves obtained for confining pressures of 68.9, 137.8, and 206.7 kPa, respectively. For any given level of confinement, the material showed only compressibility, the final volumetric deformation increasing with the confinement (up to 4 times when lateral confinement is increased from 68.9 to 206.7 kPa). For any given level of confinement, a monotonic increasing variation of the bulk modulus with the applied stress deviator was observed (see Figure 1.18). The effects of strain rate of compaction were also investigated for crosshead speed varying from 0.1 mm/min to 100 mm/min. The stress-volumetric strain curves obtained under the same confinement but at an increased strain rate show that the higher the strain rate, the higher is the degree of compaction (see Figures 1.19).

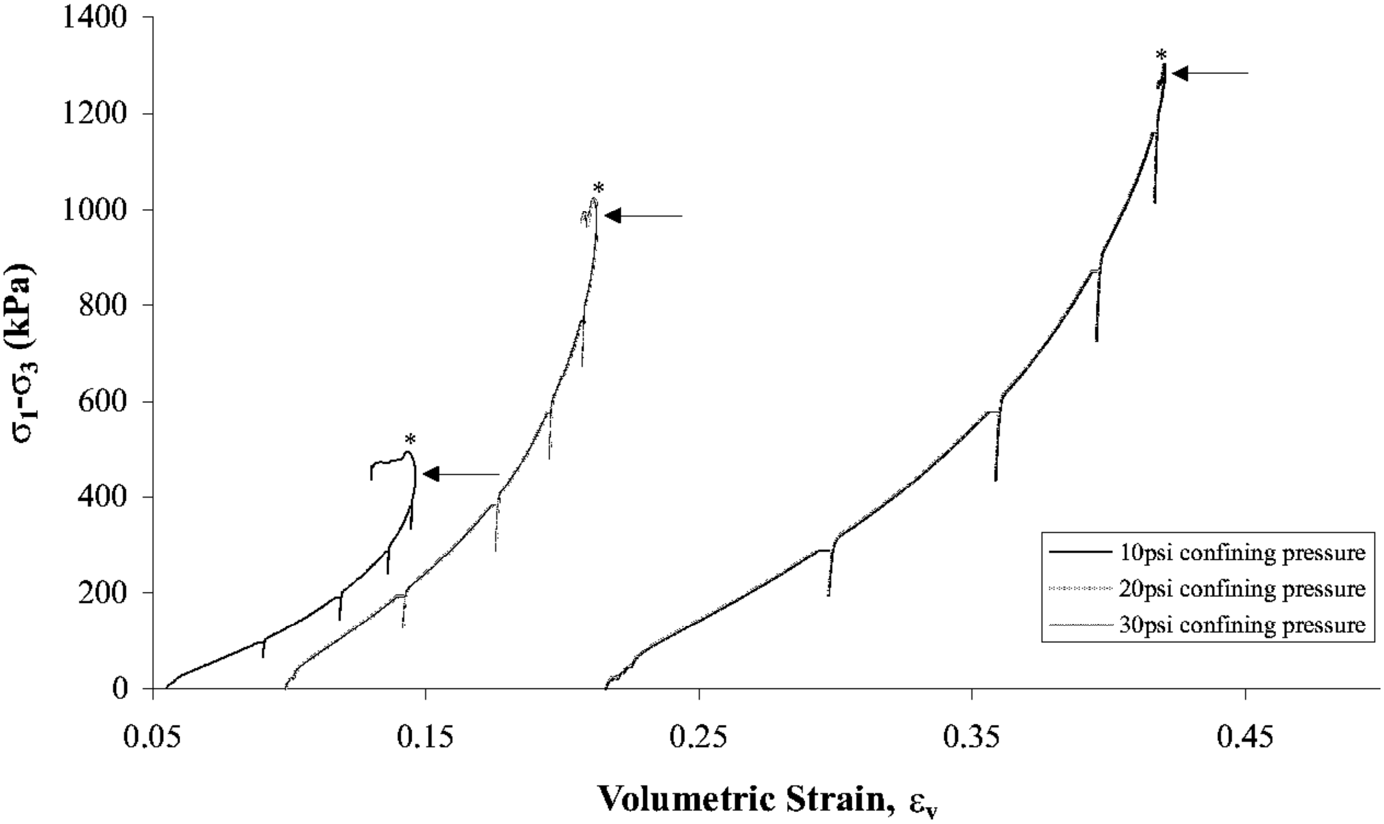

Figure 1.17: Deviatoric stress vs. volumetric strain curves for microcrystalline cellulose under confining pressures of 69 kPa , 138 kPa, and 207 kPa.

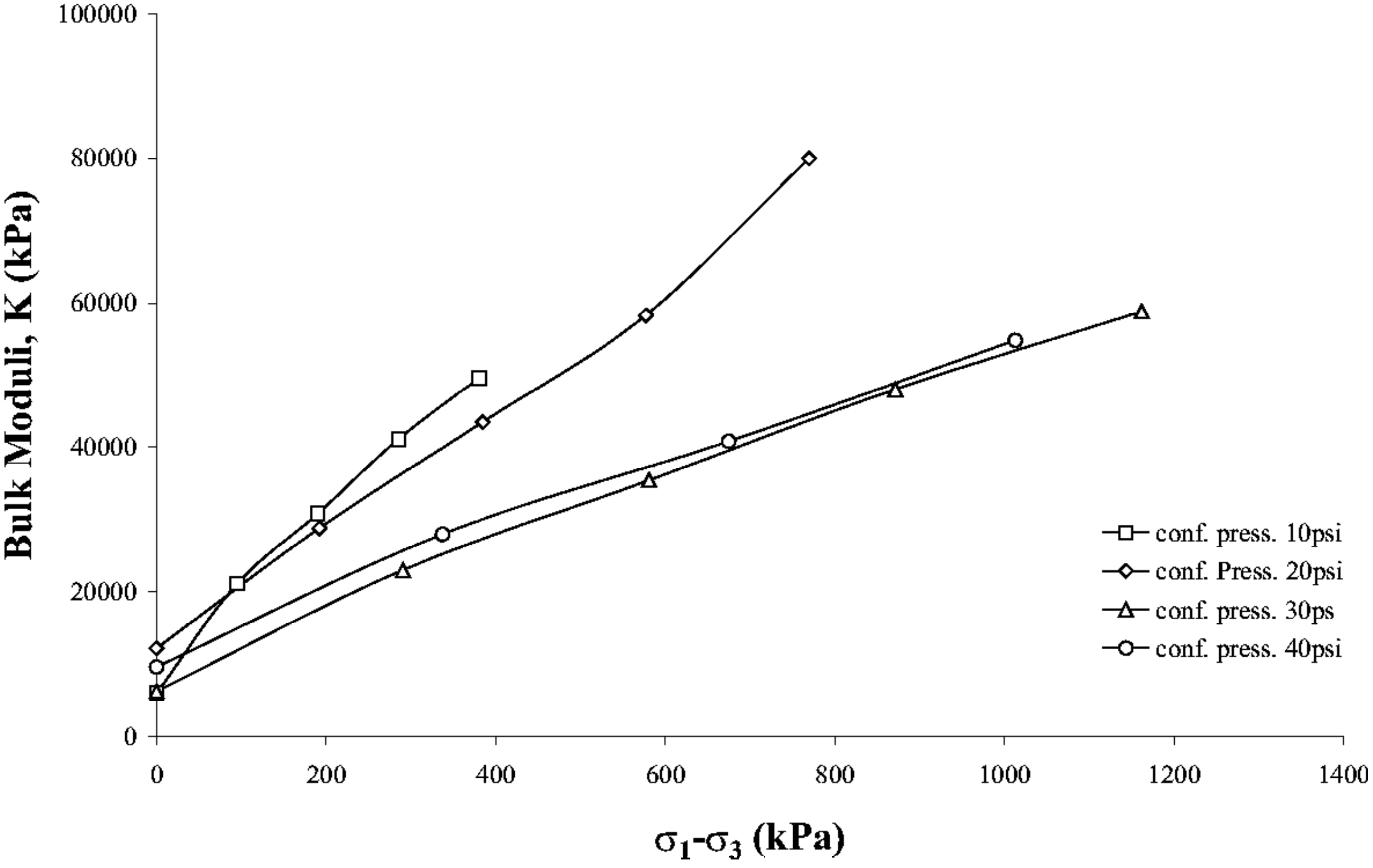

Figure 1.18: Variation of the bulk modulus K for microcrystalline cellulose as a function of deviatoric stress showing increased compaction under shear conditions.

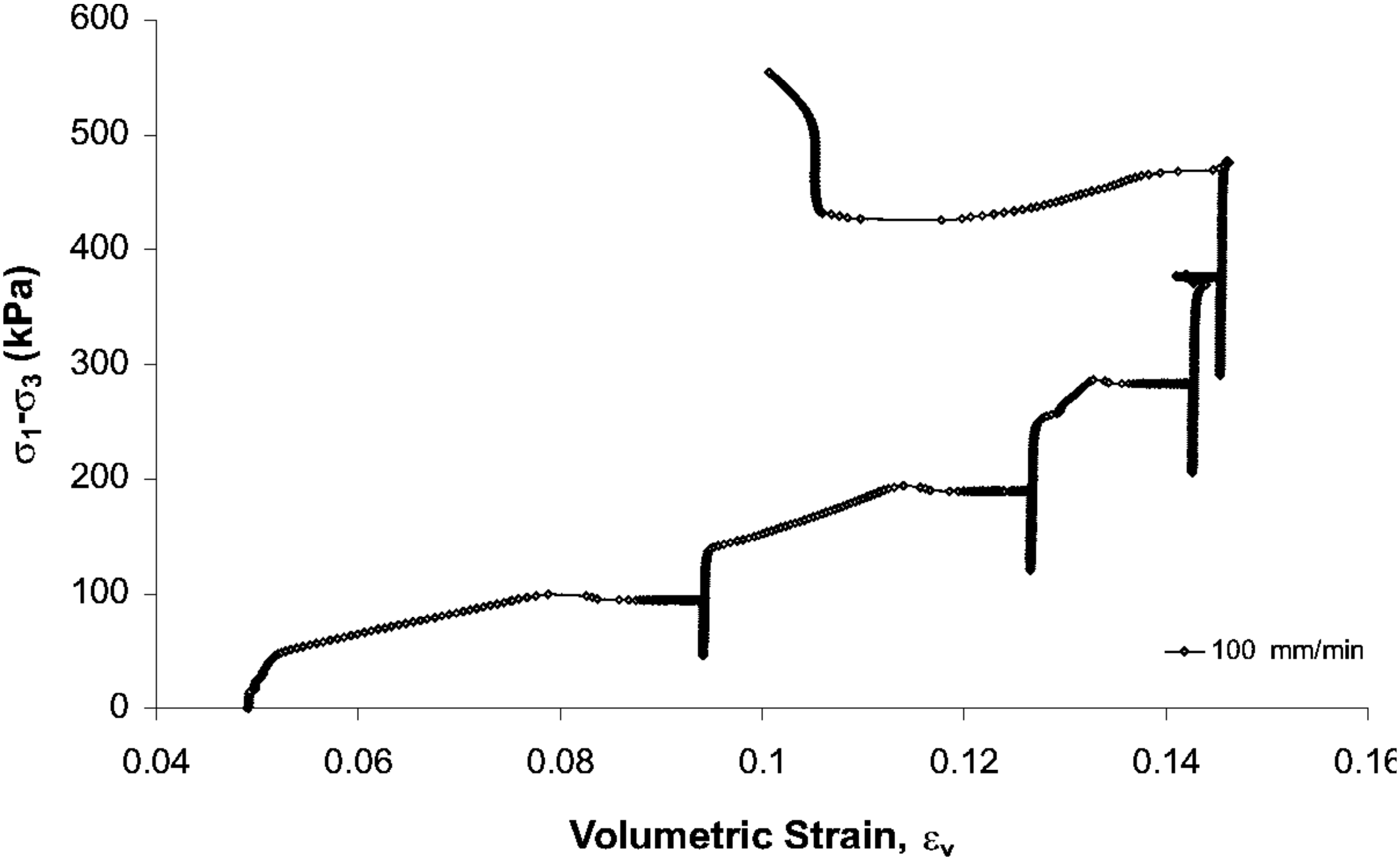

Figure 1.19(a): Strain rate effects on compaction as observed from the variation of volume in a deviatoric test for microcrystalline cellulose at a confining pressures of 69 kPa for crosshead speed of 100mm/min.

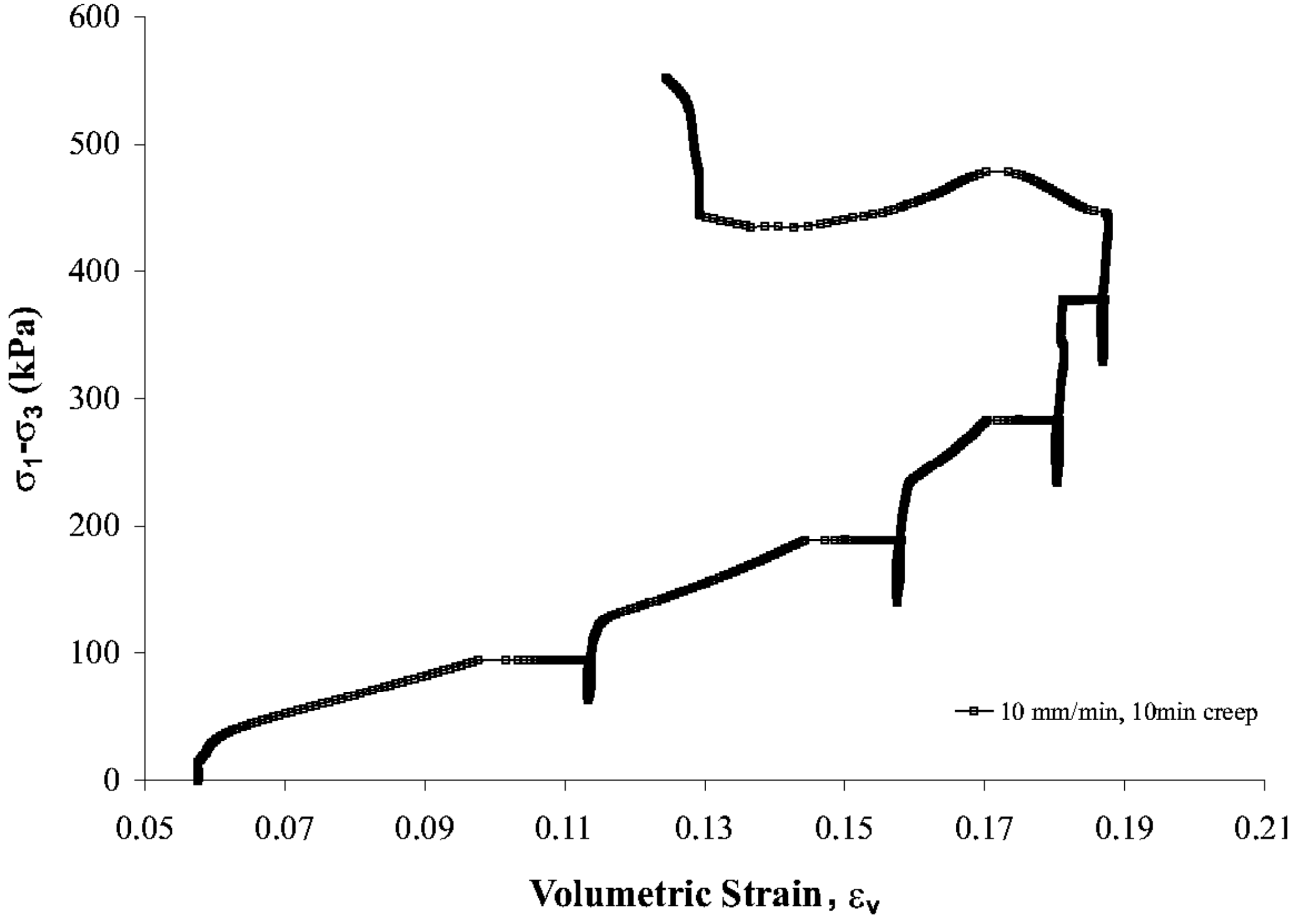

Figure 1.19(b): Strain rate effects on compaction as observed from the variation of volume in a deviatoric test for microcrystalline cellulose at a confining pressures of 69 kPa for crosshead speed of 10mm/min

References Section I

Abdel-Hadi, A. 2004. Development of a new technique for measuring volume change of dry particulate systems under very low confining pressures, Ph.D. Dissertation, Univ of Florida, Gainesville.

Abdullah, E.C. and Geldart, D., 1999. The use of bulk density measurements as flowability indicators. Powder Technol. 102, 151-165.

Arthur, J.R.F., Dunstan, T., Enstad, G.G., 1985. Determination of the Flow Function by Means of a Cubic Plane Strain Tester. Int. J. Bulk Solids Storage Silos, 1 (2), 99-128.

Bishop, A. W., Henkel, D. J., 1962. The Measurements of Soil Properties in Triaxal Test, 2nd ed., Edward Arnold, London.

Cristescu, N.D., Hunsche, U., 1998. Time Effects in Rock Mechanics. John Wiley & Sons, Ltd., Chichester.

Feise, H.J., 1998. A Review of Induced Anisotropy and Steady-State Flow in Powders, Powder Technol. 98, 191-200.

Kandala, R.N., Puri, V.M., 2000. Measurement of cohesion and angle of internal friction using cubical triaxial tester and comparison with computer controlled shear cell, Particul. Sci. Tehnol. 18 (2), 71-88.

Verwijs, M.J., Janssen, R.J.M., Scarlett, B., 2002. Influence of the intermediate principal stress during powder shear in a biaxial tester. In: Proceedings of the World Congress of Technology of Particles. Sydney, Australia, July 2002 (CD-ROM).

TASK 2: CONSTITUTIVE MODELING OF THE RESPONSE OF THE PARTICULATE SYSTEMS

II.1 Introduction

This task focus is on the development of robust constitutive models at the continuum level that can describe the behavior of particulate systems investigated over a wide range of stress and strain conditions. A large body of literature exists in which particulate systems are modeled as a plastic continuum using soil mechanics models. Critical state models such as the Cam-clay model (e.g. Roscoe and Burland, 1968) have been applied to cohesive powders (*e.g.* Puri et al. (1995)). Double-surface models such as the Drucker-Prager/cap elasto-plastic model have been used to describe ceramic powder stress-strain behavior (see Gethin et al. (1994), Aydin et al. (1996); Chtourou et al. (2002), etc.).

Continuum level models formulated in the framework of viscoplasticity theory have been used for describing short-term time effects on the quasi-static deformation of cohesive systems (*e.g.* Cazacu *et. al.* (1997), Jin and Cristescu (1998), Abdel-Hadi *et. al*. (2002) etc.). These models are capable of simulating nonlinear elastic response (stress dependency of the elastic parameters), hardening, compressible/dilatant volumetric behavior, creep and relaxation at room temperature.

All the models discussed so far neglect the effect of the third stress invariant on the behavior. Yet, there is experimental evidence showing that all three principal stresses, σ_1, σ_2, σ_3 (or equivalently all three stress invariants) influence the deformation and failure of particulate systems (see for example, Bardett and Lode, 1990; Peric and Ayari, 2000; Alawaji et al. (1992); Lade and Kim (1995), Saxena et al. (1988), Verwijs *et al.*(2002), etc.). Several models for granular materials that make use of yield functions, flow potentials, and failure conditions involving the third stress invariant were proposed by Lade and co-workers (e.g. Lade (1975); Lade (1977); Lade and Kim (1995), etc). Zhang et al. (1986) demonstrated that the elastoplastic model developed by Lade (1977) for cohensionless sands adequately describes stress-strain behavior for granular agricultural materials.

As part of this research effort, we have proposed an elasto-plastic model for the description of the inviscid behavior of the PE system. Concerning the silica system, we examined the possibility of modeling the inviscid behavior using an elasto-plastic approach and the time dependent behavior using a viscoelastic type approach. For both systems and both models, a general procedure for the determination of the constitutive parameters based on a minimum set of triaxial compression test data is provided.

In section II.2, we present the elasto-plastic model adopted for PE system. It is shown that the inviscid behavior can be described with accuracy using a single surface, Lade (1977) type elasto-plastic theory. A robust and computationally inexpensive algorithm, the convex cutting plane algorithm (Ortiz and Simo, 1986) is used to implement the elastic-plastic model. We conclude with a comparison between the model prediction and data, and suggestions for future work.

Application of the proposed elastic/plastic formulation to the silica system is presented in section II.2. Then, we proceed with the presentation of the general form of the proposed constitutive viscoelastic equation. Finally, through comparison between model predictions and data we show that the viscoelastic model provides a more realistic description of the material's response than the elastic/plastic one.

II.2 Elastic/Plastic constitutive model for PE system

From the test results conducted, it appears that short-term creep effects can be neglected and that an elastoplastic model could describe accurately the dominant properties of the PE pellets. To reduce the complexity of the model, we assume that the elastic behavior is expressed by Hooke’s law with constant moduli: E = 27555 kPa and K=17975 kPa, which correspond to the arithmetic mean of the experimental values from all performed tests. For the sake of simplicity, in the description of the plastic behavior, we assume an isotropic hardening law, i.e. the yield surface expands uniformly and that the degree of hardening is independent on the stress path. Since the material displays both compressible and dilatant behavior, the hardening parameter should be chosen such as to reflect this pattern of the plastic volumetric deformation. Thus, for PE pellets we assume that the hardening parameter is the plastic work per unit volume defined as:

$$W_p = \int \sigma_{ij} d\varepsilon_{ij}^p \ , \tag{1}$$

where σ_{ij} represents the Cauchy stress tensor and $d\varepsilon_{ij}^p$ is the plastic strain increment. The plastic work (1) can be written as

$$W_p = \int I_1 d\varepsilon_V^p / 3 + \int \sigma'_{ij} d\varepsilon'^p_{ij} \ , \tag{1.a}$$

where I_1 is the first invariant of the stress tensor ($I_1 = \sigma_1 + \sigma_2 + \sigma_3$), $d\varepsilon_V^p$ is the plastic volumetric strain increment and "prime" stands for deviator. The second term on the right-hand side of (1a) is always positive and represents the energy input needed for change in shape. The first term on the right-hand side is the energy related to plastic volume change that is stored during compaction and released during volumetric expansion of the system. Because Lade's elastic/plastic theories account for the dependence of the plastic deformation and strength on all stress invariants, and the hardening parameter is the plastic work, for PE pellets we use the expressions of the failure, yield function, and plastic potential proposed in Lade (1977). Thus, the failure condition for PE pellets is assumed to be of the form:

$$\left(\frac{I_1^3}{I_3} - 27\right) \cdot \left(\frac{I_1}{p_a}\right)^m = \eta_1 \tag{2}$$

where $I_3 = \sigma_1 \sigma_2 \sigma_3$ stands for the third stress invariant, p_a is the atmospheric pressure measured in the same units as the stress, while m and η_1 are material parameters. The numerical values of these coefficients are: $m = 0.12$ and $\eta_1 = 21.4$. These values were determined using strength data obtained in standard triaxial compression tests (see Section I.3) in conjunction with (2). In the principal stress space, the shape of the failure surface defined by (2) is conical, with the apex of the cone being at the origin of the stress axes. Since the hypothesis of isotropic hardening was made, under continuous loading the yield surface expands symmetrically about the hydrostatic axis, its ultimate position being the failure surface (2). Hence, the yield function is given by:

$$\left(\frac{I_1^3}{I_3} - 27\right) \cdot \left(\frac{I_1}{p_a}\right)^m = F\left(W_p\right) \tag{3}$$

The specific expression of the work-hardening law for PE pellets can be determined empirically by calculating the experimental values of the plastic work in a standard triaxial compression test and plotting its variation with $f_p \equiv \left(\frac{I_1^3}{I_3} - 27\right) \cdot \left(\frac{I_1}{p_a}\right)^m$ (see Figure 2.1). An exponential variation as proposed by Lade (1977) was found to approximate well PE data, *i.e.*:

$$f_p\left(W_p\right) = a \cdot \mathrm{e}^{-b\,W_p} \cdot \left(\frac{W_p}{p_a}\right)^{\frac{1}{c}} \quad , \quad c > 0 \tag{4}$$

where the coefficients *a*, *b*, and *c* are functions of the confining pressure (see Figure 2.1 showing the relationship between f_p and the plastic work at 14.7 and 35 kPa confining pressure, respectively).

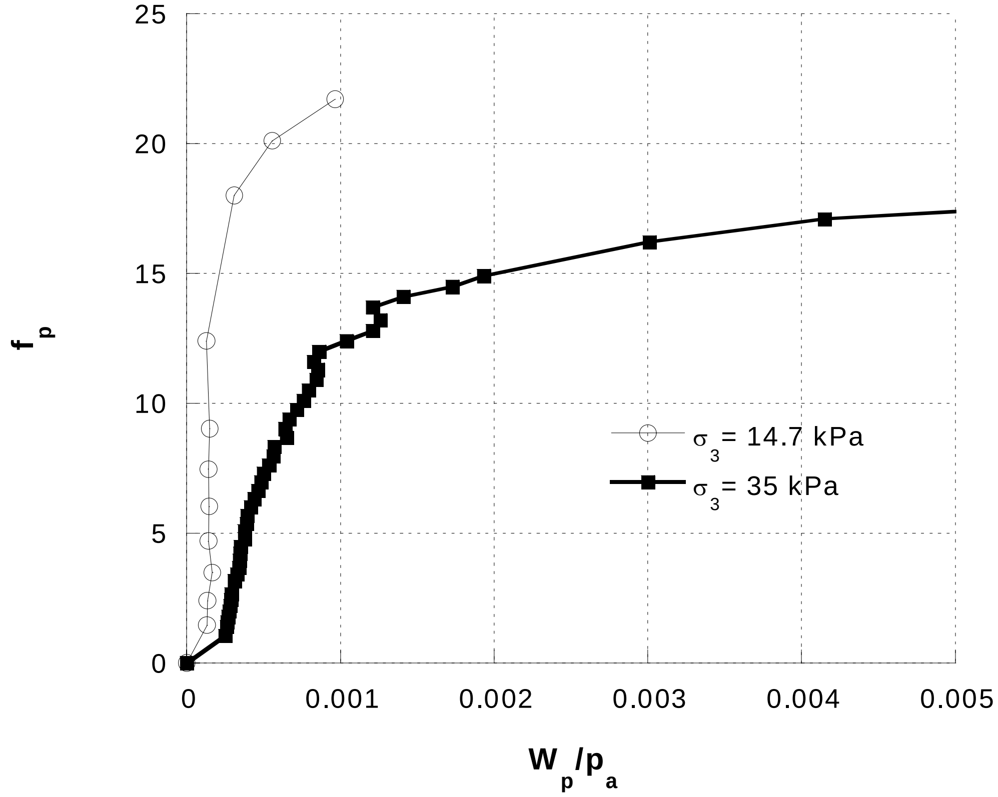

Figure 2.1: Variation of the plastic work normalized by the atmospheric pressure with the stress level $f_p \equiv \left(\frac{I_1^{\,3}}{I_3} - 27\right) \cdot \left(\frac{I_1}{p_a}\right)^m$ at σ_3 = 14.7 and 35 kPa, respectively

For PE pellets, a linear variation of *c* with the confining pressure was observed:

$$c = \kappa + \xi \cdot \frac{\sigma_3}{p_a} \tag{5}$$

where κ = 14047 and ξ = -0.0447. Since the ultimate position of the yield surface is the failure surface, for a given value of the confining pressure, $f_p\left(W_p^{peak}\right) = \eta_1$, where W_p^{peak} is the value of the plastic work at the peak deviatoric stress. Thus, using (4) it follows that:

$$a = \eta_1 \left(\frac{e \cdot p_a}{W_p^{peak}} \right)^{1/c},$$

$$b = \frac{1}{c \cdot W_p^{peak}} \tag{6}$$

where e is the basis of the natural logarithm. The variation of W_p^{peak} with the confining pressure can be approximated by:

$$W_p^{peak} = n \cdot p_a \cdot \left(\frac{\sigma_3}{p_a} \right)^l, \tag{7}$$

where *l* = 0.125 and *n* = 0.977. Next, by making use of (6) and (7), the laws of variation of the coefficients *a* and *b* with confining pressure can be obtained.

The formulation of the model is completed by providing the plastic potential. If the plastic potential coincides with the yield function, then

$$d\varepsilon_3^p / d\varepsilon_1^p = \left(\partial f_p / \partial \sigma_1\right) / \left(\partial f_p / \partial \sigma_3\right), \tag{8}$$

$d\varepsilon_3^p$ and $d\varepsilon_1^p$ being the plastic axial strain and plastic lateral strain increments, respectively, σ_1 the axial applied stress, and σ_3 the given confining pressure. However, for PE pellets as for most particulate systems, (8) is not in agreement with the experimental data, thus the flow rule ought to be nonassociated. Following Lade (1977), we consider for the plastic potential a mathematical form similar to that of the yield function, i.e.:

$$g_p = I_1^{\,3} - \left(27 + \eta_2 \left(\frac{p_a}{I_1} \right)^m \right) \cdot I_3 ,$$

(9)

where η_2 is a constant for given values of f_p and σ_3. Note that if η_2 were equal to f_p at all stress levels, the plastic potential would coincide with the yield function (2). Thus,

$$d\varepsilon^p{}_{ij} = d\lambda_p \cdot \left(\frac{\partial g_p}{\partial \sigma_{ij}} \right), \tag{10}$$

where $d\lambda_p$ is the plastic factor. Next, using the flow rule (10), η_2 can be expressed as:

$$\eta_2 = \frac{3 \cdot \left(1 + \upsilon^p\right) \cdot I_1^2 - 27 \cdot \sigma_3 \cdot \left(\sigma_1 + \upsilon^p \cdot \sigma_3\right)}{\left(\frac{p_a}{I_1} \right)^m \cdot \left[\sigma_3 \cdot \left(\sigma_1 + \upsilon^p \cdot \sigma_3\right) - \frac{m \cdot \left(1 + \upsilon^p\right) \cdot I_1^2}{f_p \cdot \left(p_a / I_1\right)^m + 27} \right]}$$

(11)

where $\nu^p = -\frac{d\varepsilon_3{}^p}{d\varepsilon_1{}^p}$. For any given value of the confining pressure, η_2, computed using (11), was found to have a linear variation with f_p; the slope could be considered constant, whereas the intercept depends on the confining pressure. A simple expression of the type proposed by Lade (1977) was found to approximate well PE data:

$$\eta_2 = s \cdot f_p + r \sqrt{\frac{\sigma_3}{p_a}} + t \tag{12}$$

where *s* = 0.033, *r* = -3.265, and *t* = -1.554. Again, since the experimental values of η_2 are smaller than f_p, f_p does not coincide with g_p i.e. the flow rule is nonassociated. Note that negative values of η_2 correspond to compressive volumetric behavior whereas positive values correspond to expansive plastic behavior (Lade, 1977).

II.3. Numerical Implementation and Comparison with experimental results

The increased complexity of the constitutive models, justified by the need to reproduce with improved accuracy material behavior under general loading, deformation, and strain rate conditions, result in increased complexity of the numerical algorithms. In an effort to obtain a better global accuracy and stability of the numerical solution, algorithms that can be applied to a specific class of models are being developed (see for example, Ahadi and Krenk (2003) for a 3D generalization of Cam-Clay models or Borja et al. (2003) for smooth three invariant representations of Mohr-Coulomb model).

In this work, a robust and computationally inexpensive method, the convex cutting plane (CCP) algorithm, proposed by Ortiz and Simo (1986) was used to integrate the single-surface elastoplastic model presented in the previous section. It is an implicit procedure, which is computationally attractive because it can be linearized in closed form. The normality condition is enforced at the initial (known) iteration and the algorithm does not require the gradient of the flow rule or hardening law. The flow chart for the procedure applied to the elastoplastic Lade type model is given below.

1. Initialize the iteration counter step *k=0*.

2. Initialize the plastic strain $\varepsilon^{p\,(0)}_{n+1} := \varepsilon^{p}_{n}$, the plastic work $W_{p_{n+1}}^{(0)} = W_{p_n}$ and plastic factor $\Delta\lambda_{n+1}^{(0)} := 0$.

3. Compute ***C***, the matrix of elastic moduli, possibly depending on the initial stress σ_n through its invariants

4. While *k<k max* repeat steps 5-14.

5. Compute the trial elastic stress $\sigma_{n+1}^{(k)} = C : \left(\varepsilon_{n+1} - \varepsilon^{p\,(k)}_{n+1}\right)$.

6. Compute $[I_1^{(k)}\ I_2^{(k)}\ I_3^{(k)}]$ the invariants of the trial elastic stress tensor $\sigma_{n+1}^{(k)}$.

7. Compute the increase in hardening parameter $f_{p\,n+1}^{(k)}$ as: $f_{p\,n+1}^{(k)} = a \cdot e^{-b\cdot W_{p\,n+1}} \cdot \left(\frac{W_{p\,n+1}}{p_a}\right)^{1/c}$

8. Compute the plastic moduli, $D_{n+1}^{(k)}$ as

$$D_{n+1}^{(k)} = a \cdot e^{-b\cdot W_{p\,n+1}} \cdot \left[-b \cdot \left(\frac{W_{p\ n+1}}{p_a}\right)^{\frac{1}{c}} + \frac{1}{c} \cdot \left(\frac{1}{p_a}\right)^{\frac{1}{c}} \cdot W_{p\,n+1}^{\frac{1}{c}-1}\right]$$

9. Compute the yield function $f_{n+1}^{(k)} = f\left(\sigma_{n+1}^{(k)}, w_{n+1}^{(k)}\right) := \left(\frac{I_1^{3\ (k)}}{I_3^{(k)}} - 27\right) \cdot \frac{I_1^{(k)}}{p_a} - w_{n+1}^{(k)}$.

10. Is $f_{n+1}^{(k)} \leq TOL_1$ true?

The condition verifies that $\sigma_{n+1}^{(k)}$ is on or under the yield surface of hardening parameter $f_{p\,(n+1)}^{(k)}$ and TOL_1 is a tolerance, accounting for rounding errors.

11. If YES, the final new stress is equal to the elastic trial stress. END AND EXIT.

12. If NOT, plastic correction is needed, as follows:

13.Obtain increments to plastic factor: $\Delta^2\lambda_{n+1}^{(k)} = \dfrac{f_{n+1}^{(k)}}{\left(\dfrac{\partial f_{n+1}^{(k)}}{\partial \sigma}\right)^T C \dfrac{\partial f_{n+1}^{(k)}}{\partial \sigma} - \dfrac{\partial f_{n+1}}{\partial f_p}^{(k)} D_{n+1}^{(k)}}$

14.Update plastic strain, plastic factor, and state variable:

$$\varepsilon_{n+1}^{p\ (k+1)} = \varepsilon_{n+1}^{p\ (k)} + \Delta^2\lambda_{n+1}^{(k)} \frac{\partial f_{n+1}}{\partial \sigma}^{(k)}$$

$$\Delta\lambda_{n+1}^{(k+1)} = \Delta\lambda_{n+1}^{(k)} + \Delta^2\lambda_{n+1}^{(k)}$$

$$f_{p\,n+1}^{(k+1)} = f_{p\,n+1}^{(k)} + \Delta^2\lambda_{n+1}^{(k)} D_{n+1}^{(k)}$$

15. Update iteration counter $k=k+1$ and return to step 4.

Figures 2.2 (a) and 2.2 (b) show comparisons between numerical simulations and data obtained in monotonic tests at 14.7 and 35 kPa confining pressures. Note that the model describes well the overall stress-strain behavior observed in the tests. The main features of the volumetric response, particularly the increase in the value of the dilatancy threshold level with increasing confining pressure are very well simulated. The very good agreement between the experimental pressure-volumetric strain curve under isotropic compression and the linear elastic response curve corresponding to K= 17975 kPa (see Figure 2.3) shows that this average value of the bulk modulus is an accurate measure of the compressibility of the material.

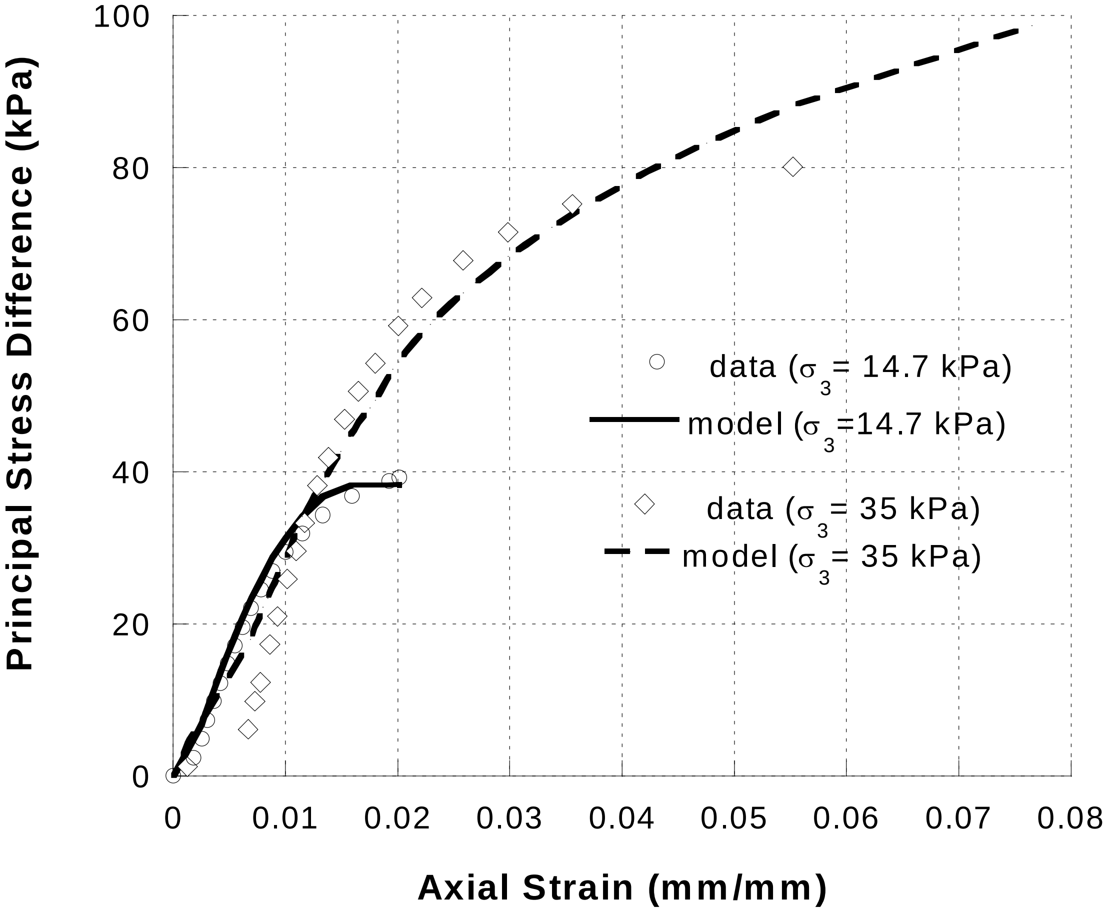

Figure 2.2 (a): Comparison between theoretical and experimental stress-axial strain curves at $\sigma_3 =$ 14 kPa and 35 kPa, respectively .

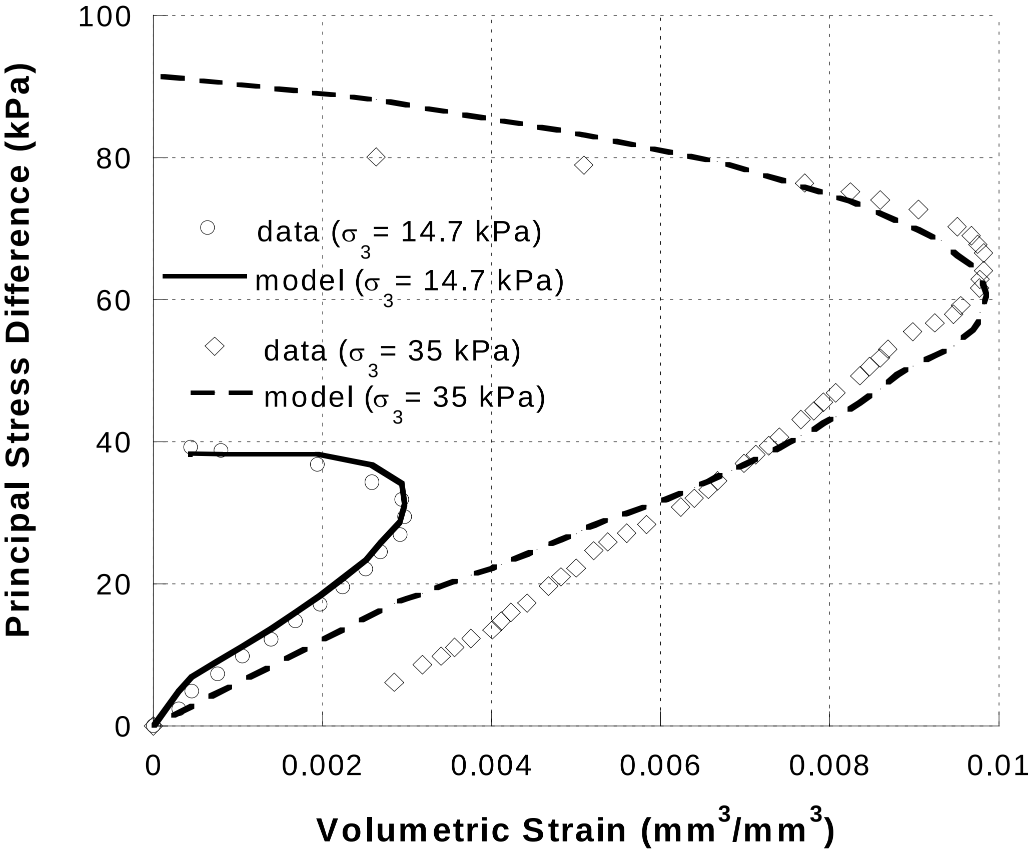

Figure 2.2 (b): Comparison between theoretical and experimental stress-volumetric strain curves at σ_3 = 14 kPa and 35 kPa, respectively;

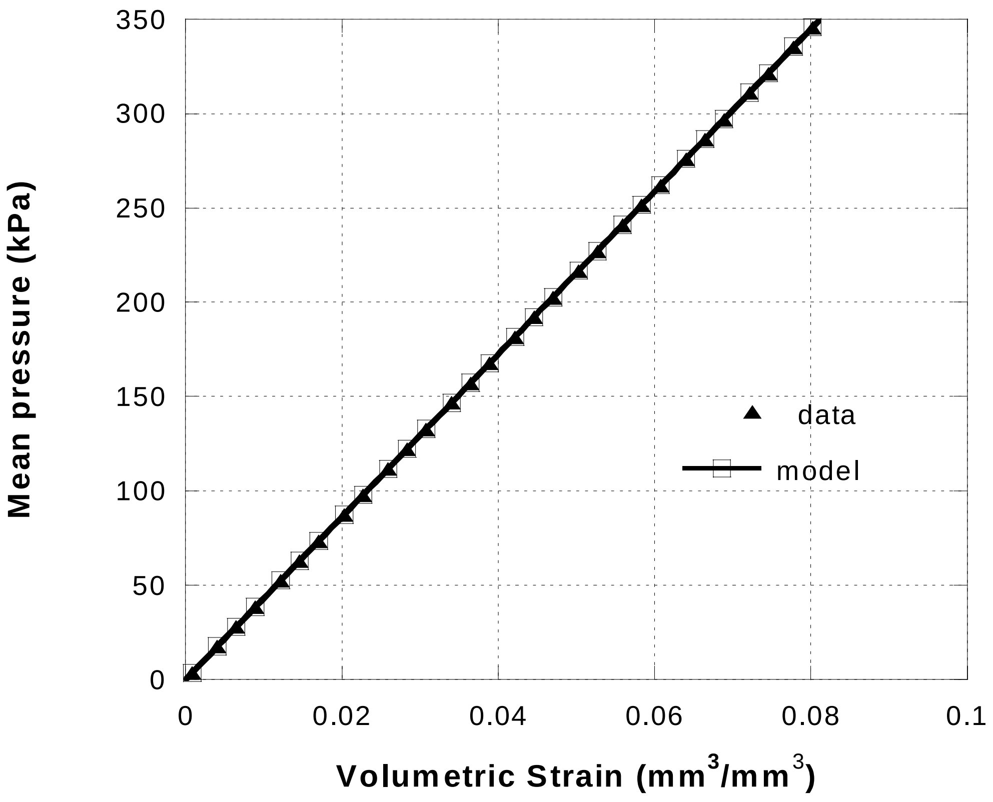

Figure 2.3: Comparison between theoretical and experimental stress strain curves for hydrostatic compression on PE pellets

II.4. Constitutive Modeling of the Behavior of the Silica System

II.4.1 Elastic/plastic Approach

Data shows that even in the elastic regime the behavior is strongly nonlinear (see Section I.3.2 and I.3.3). Thus, the elastic behavior should be modeled using a differential Hooke's law with variable elastic moduli. To reproduce the stress dependency of the Young modulus E, we propose a law of variation with the mean pressure of the form:

$$E = E_\infty + \gamma \cdot p_a \cdot e^{-\delta \cdot \left(\frac{I_1}{p_a}\right)} \tag{13}$$

where I_1 denotes the first stress invariant $(I_1 = \sigma_1 + \sigma_2 + \sigma_3)$, $E_\infty (= 2.5 \cdot 10^5 kPa)$ is an asymptotic value corresponding to very high pressures, p$_a$ is the atmospheric pressure, while γ and δ are material constants. For silica, we found that $\gamma = -2.0017 \cdot 10^5$ and $\delta = 8.3 \cdot 10^{-4}$.

Similarly, the variation of the bulk modulus K with the mean stress was approximated by:

$$K = K_\infty + \psi \cdot p_a \cdot e^{-\beta \cdot \frac{I_1}{p_a}} \tag{14}$$

where $K_\infty = 2.5 \cdot 10^5 kPa$ $\psi = -1.399 \cdot 10^5$ and $\beta = 1.21 \cdot 10^{-3}$. The comparison between the theoretical variation of the bulk modulus with the mean pressure and data is shown in Figure 2.4.

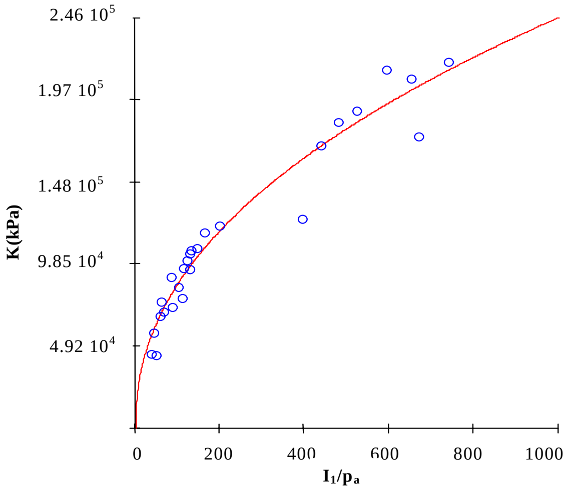

Figure 2.4: Comparison between the experimental and theoretical variation of the bulk modulus with the mean pressure for silica system.

First, we interpreted the data in terms of the Mohr-Coulomb criterion. In this model it is assumed that the material is perfectly plastic, *i.e.* the yield locus is fixed in the stress space. The yield surface coincides with the failure surface:

$$\tau_f = c + \sigma_n \tan\varphi \tag{15}$$

where τ_f and σ_n are the shear and normal stresses on the failure plane, respectively; *c* is the cohesion, and φ is the angle of internal friction. We estimated the cohesion and the angle of internal friction from compression data. We found $c = 0.56kPa$ and $\varphi = 33^\circ$. Figure 2.5 shows a comparison between model and data. The Drucker Prager criterion was also used to interpret the data. The advantages of using Drucker-Prager over Mohr- Coulomb are: (1)it is expressed in terms of stress invariants and thus can be applied to describe failure surface under any loading conditions, (2) it has been proven to accurately describe the strength characteristics of granular media. The expression of Drucker-Prager criterion is:

$$\sqrt{I_{2D}} = \alpha \cdot I_1 + k \tag{16}$$

where I_1 is the first stress invariant, I_{2D} the second invariant of the stress deviator, α and k are material parameters. For silica we found $\alpha = 0.3197$ and $k = 1.304$.

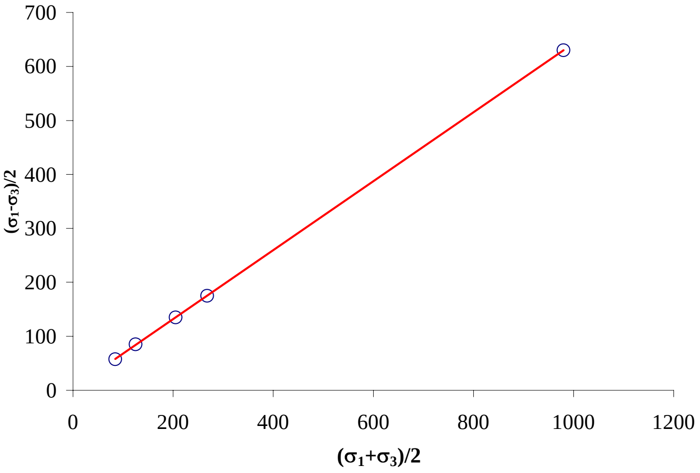

Figure 2.5: Mohr-Coulomb Yield Surface for silica system.

We have also modeled the observed behavior using the elastic/plastic model developed by Lade and co-workers. In this theory the total strain increment $d\varepsilon$ due to a stress increment $d\sigma$ is divided in three components: an elastic strain component $d\varepsilon^e$, a plastic collapse strain increment component $d\varepsilon^c$, and a plastic expansive strain increment component $d\varepsilon^p$, such that:

$$d\varepsilon_{ij} = d\varepsilon_{ij}^e + d\varepsilon_{ij}^c + \varepsilon_{ij}^p \tag{17}$$

The elastic strain is computed using a non-linear Hooke's law. The plastic collapse strain is given by a plastic stress-strain theory involving a cap-type yield surface while the plastic expansive strains are computed using a stress-strain theory, which involves a conical yield surface with apex at the origin of the stress space. The collapse behavior, which occurs under hydrostatic conditions is modeled by the yield function:

$$f_c = \left(\frac{W}{k \cdot p_a} \right)^{\frac{1}{d}} p_a^2 \tag{18}$$

where W is the irreversible stress work and $f_c = I_1^{\,2} + 2 \cdot I_2^{\,2}$, with I_1 and I_2 being the first and second invariant of the stress tensor. For our system, $k = 0.0122$ and $d = 0.8$.

The expansive behavior is governed by the following yield function:

$$f_p = \left(\frac{I_1^{\,3}}{I_3} - 27 \right) \cdot \left(\frac{I_1}{p_a} \right)^m \tag{19}$$

while the failure condition is given by: $f_p = \eta_1$. For silica, we found that $m = 0.088$ and $\eta_1 = 1.82$. Hydrostatic compression of an isotropic powder system results in equal linear strains in the three principal directions. For this condition, the direction of the strain increments concides with the hydrostatic axis. Thus, the plastic potential must be equal to the spherical yield cap (f_c). In Figure 2.6. (a) is shown the location of the yield cap relative to the conical failure surface for silica. The plastic potential for expansive strains is given by:

$$g_p = I_1^{\;3} - \left(27 + \eta_2 \left(\frac{p_a}{I_1} \right)^m \right) \cdot I_3 \tag{20}$$

For given values of f_p and σ_3, η_2 is a constant. Negative values of η_2 correspond to plastic volumetric strains, which are compressive, and positive values of η_2 correspond to plastic expansive strains. In Figure 2.6b the yield surface of silica in the principal stress space is also shown.

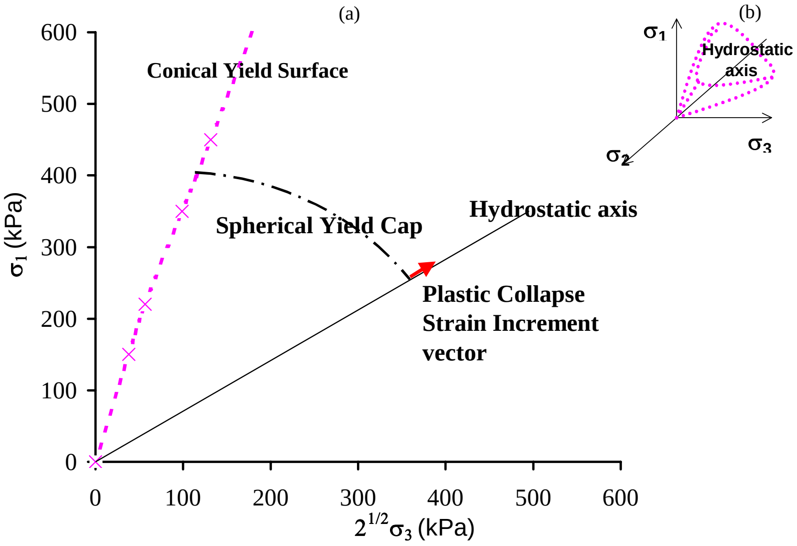

Figure 2.6: (a) Calculated Failure Surface (–×–) and yield cap in triaxial plane.(b) trace of the yield surface in octahedral plane for silica system.

II.4.2 Numerical Implementation

Hydrostatic Response

The Closest Point Projection and the Cutting-Plane algorithms were both implemented in MatLab. A parameter sensitivity study was done on the constants involved in the expression of the bulk modulus and hardening law. It appears that the closest agreement between simulation and experimental results is obtained when the Cutting-Plane algorithm is used, an exponential type of law of variation for K and a hardening constant $d=1$ (see Figure 2.7).

Deviatoric Response

Comparison between experimental and simulation results for silica show that the model describes particularly well the effect of confining pressure on the volumetric strains. The non-linearity, the stress-path dependency and the gradual change from compressible to dilatant behavior were correctly modeled. It was thus demonstrated that the theory is applicable to silica for general 3-D conditions. As an example in Figures 2.8 and 2.9 is shown a comparison between experimental data and simulation results using the model for a confining pressure of 70.6 kPa. Although the model overestimates the data, the transition from compressibility to dilatancy is well reproduced.

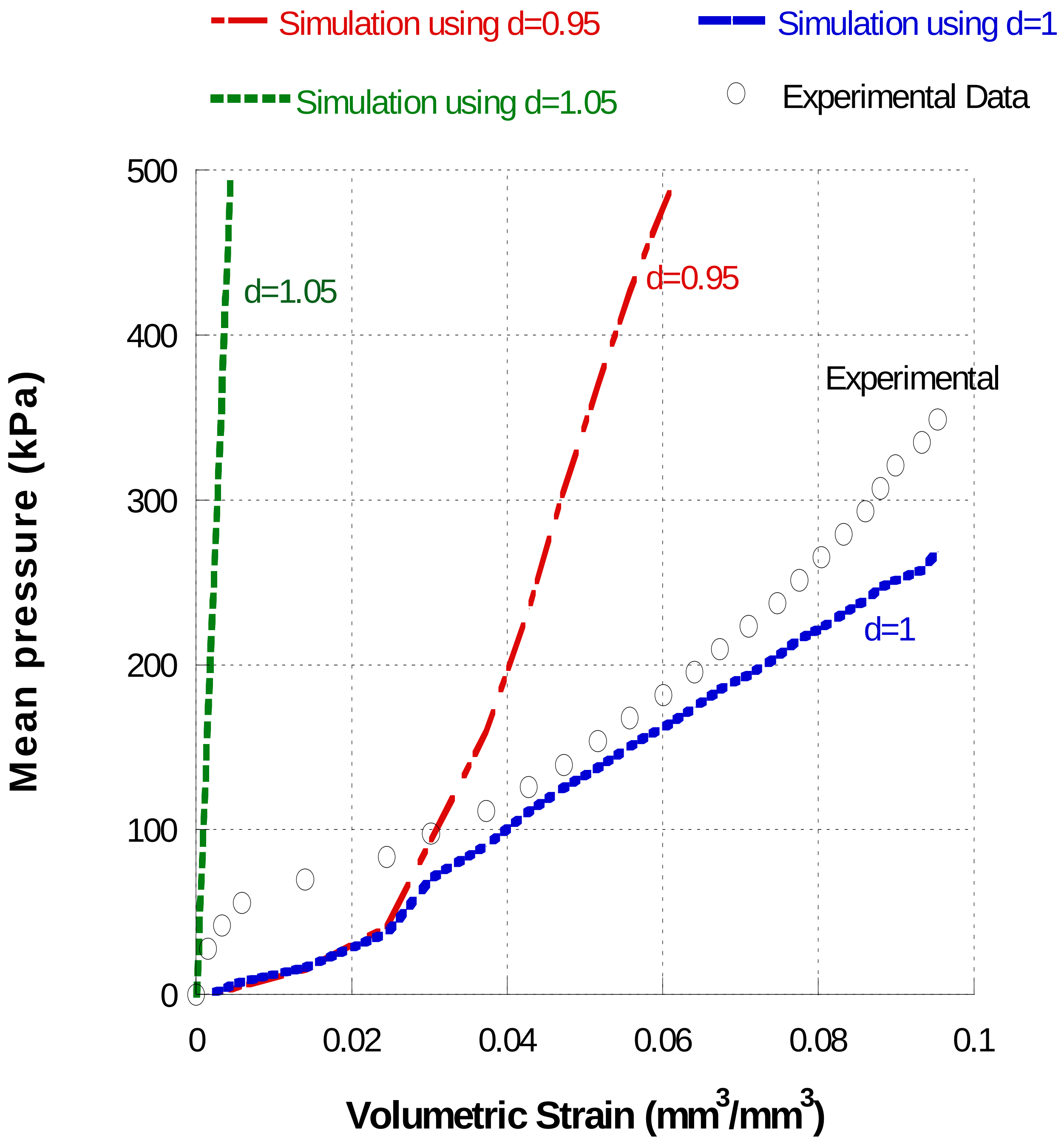

Figure 2.7: Mean stress vs. volumetric strain for silica system. Effects of hardening constant d.

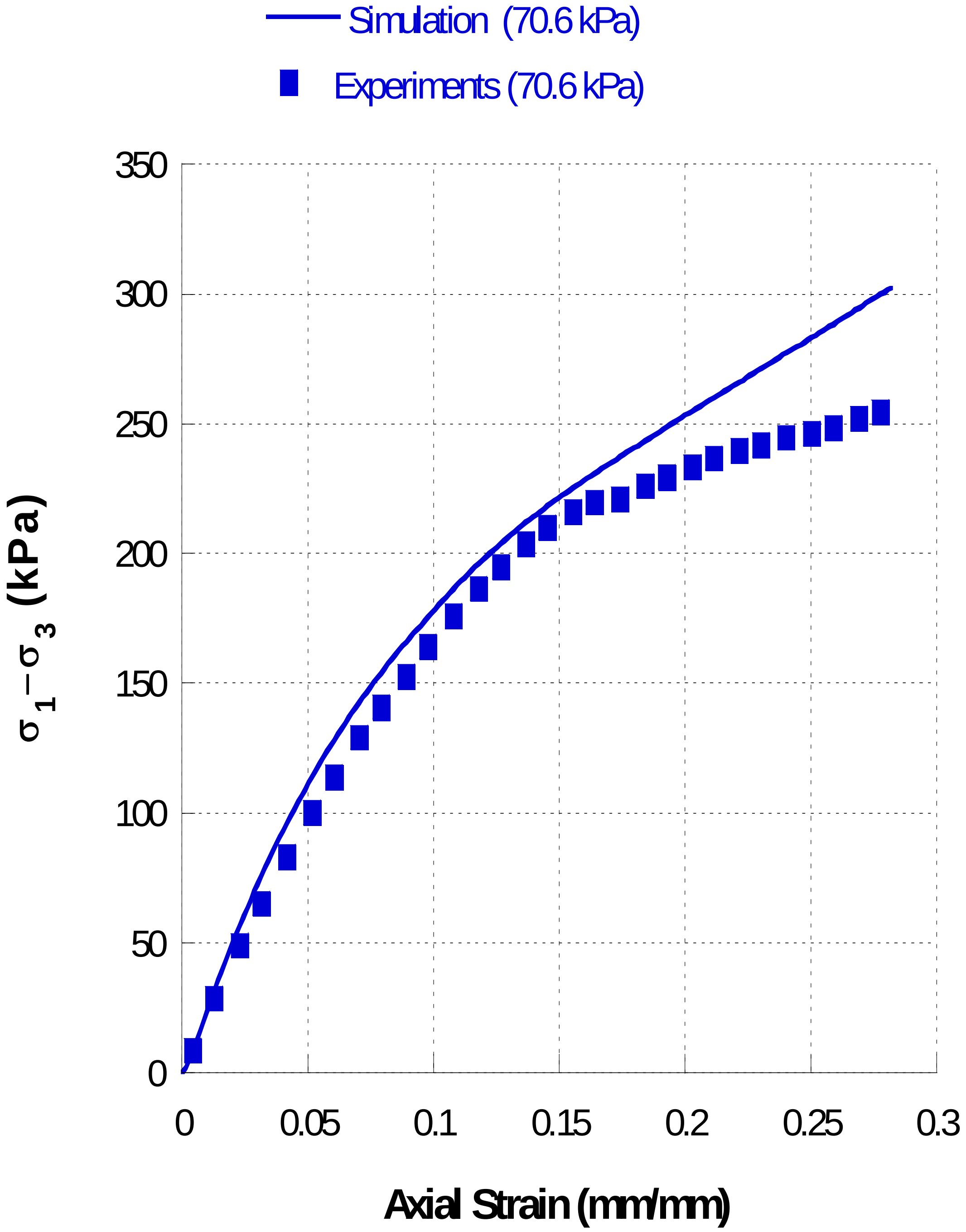

Figure 2.8: Simulated and experimental deviatoric stress vs. axial strain at 70.6 kPa for silica powder.

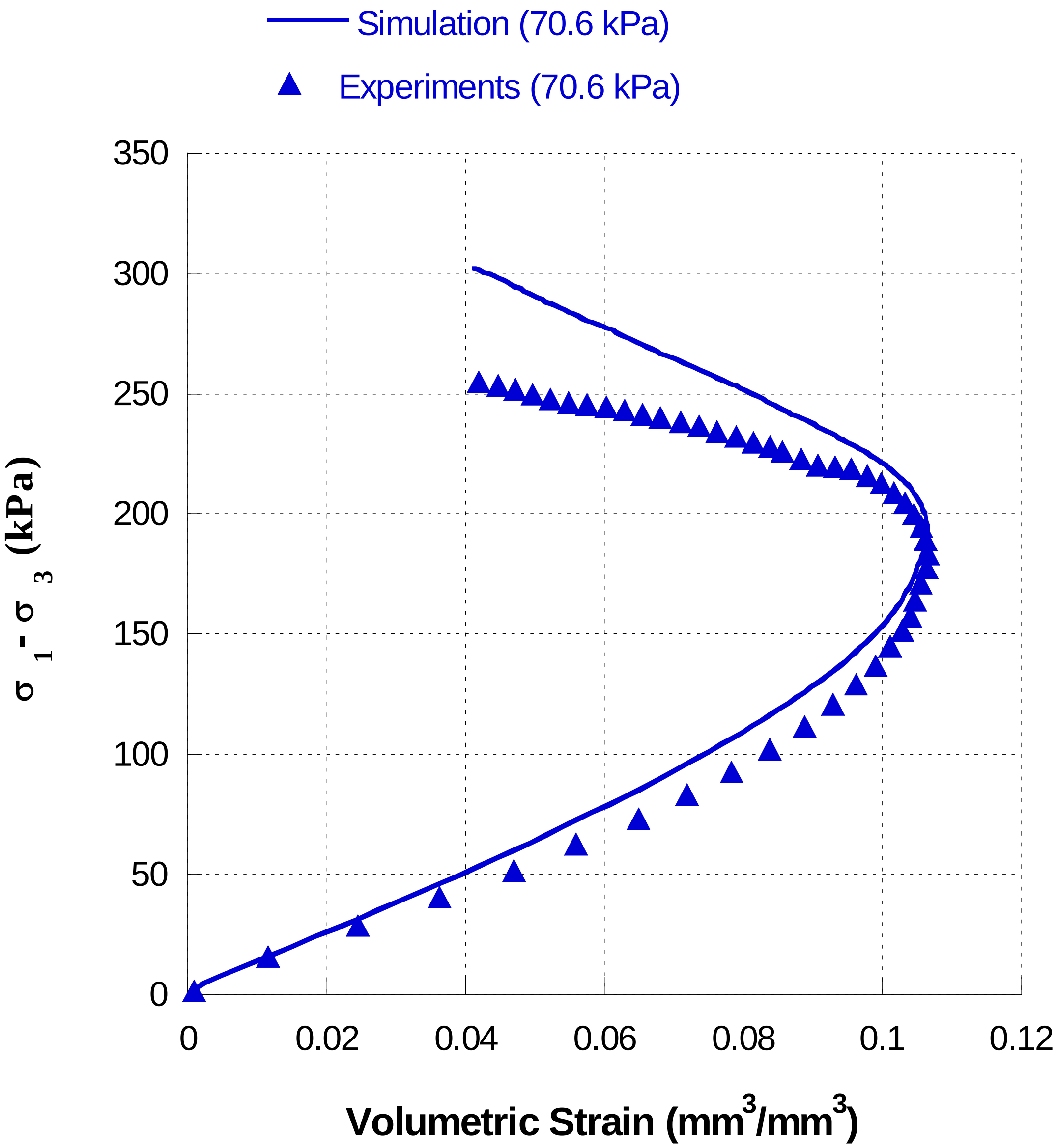

Figure 2.9: Simulated and experimental deviatoric stress vs. volumetric strain curve corresponding to a confining pressure of 70.6 kPa confinement for silica powder.

II.4.3 Viscoelastic Modeling

In this section, we present a novel quasi-linear viscoelastic model aiming at describing besides time effects such as creep, stress relaxation, and strain rate effects, the fundamental mechanical property exhibited by particulate systems that is to be either compressible or dilatant depending on the stress state.

The general form of the proposed constitutive equation is:

$$\dot{\varepsilon}_V = -k_V\left(\varepsilon_V - H(p,q)\right) + \frac{\dot{p}}{K} \tag{21}$$

$$\dot{\varepsilon}' = -k\left(\varepsilon' - G(p,q)\,\sigma'\right) + \frac{\dot{\sigma}'}{2G} \tag{22}$$

where ε' denote the deviator of the strain tensor and ε_V stand for the volumetric strain. We assume that the instantaneous response is elastic and is characterized by K and G, the dynamic bulk modulus and shear modulus, respectively. In equations (21)-(22), $H(p,q)$ and $G\left(p,q\right)$ define the stabilization boundaries for the volumetric and shearing strains and are assumed to depend on stress through $p = \frac{tr\,\boldsymbol{\sigma}}{3}$ and $q = \sqrt{\frac{3}{2} tr\,(\boldsymbol{\sigma}')^2}$, the first invariant of the stress tensor $\boldsymbol{\sigma}$ and the second invariant of the stress deviator $\boldsymbol{\sigma}'$. The volumetric and shearing viscosities, denoted by k and k_V, are considered to be constant. The main features of our model that distinguishes it from the classical viscoelastic ones are: (i) the volumetric part of the strain depends on both the deviatoric (shear) stress components and mean pressure, (ii) the deviatoric part of the strain is also influenced by the volumetric deformability characteristics. We will show that by a judicious choice of the mathematical expressions of the relaxation boundaries, all the observed characteristics of the deformation of particulate systems could be described with high accuracy.

Application of the constitutive model to silica

For a given particulate system, the specific mathematical expressions of the constitutive functions involved in the proposed model could be determined from the quasi-static confined triaxial compression data. Indeed, the monotonic response curves at a very low strain rate could be considered to be close to the stabilization boundaries. Under confined triaxial compression conditions, silica exhibits both compressibility and dilatancy and the $\sigma_1 - \sigma_3$ vs. ε_V curve show a plateau for stresses close to failure (see Section I, Figure 1.5(b)). To reproduce these characteristics, we approximate the relaxation boundary for the volumetric strain with a hyperbola that passes through the origin

$$H(p,q)=\frac{q-d}{c}-\frac{ad}{c(q-a)},$$

(23)

and of asymptotes: $q=a$ and $q=c\varepsilon_V+d$, where *a, c,* and *d* are functions of the stress state. For a given confining pressure σ_3 = constant, *a* represents the horizontal asymptote toward which tends the $\sigma_1-\sigma_3$ vs. ε_V curve whereas *c* is the double of the slope of the tangent at the origin of the same curve. Furthermore,

$$d=\frac{(q_d-a)^2}{a}\cdot\frac{\tan^2\alpha+1}{\tan^2\alpha-1} \tag{24}$$

where $c=\tan 2\alpha$ and q_d denotes the dilatancy threshold. For silica, we found that the variation of the functions *a, c,* and q_d with the stress state is very well described by

$$a=a(\sigma_3)=a_1\sigma_3+a_2 \tag{25.1}$$

$$c=c(\sigma_3)=c_1\sigma_3^2+c_2\sigma_3+c_3 \tag{25.2}$$

$$q_d=q_d(\sigma_3)=v_1\sigma_3^2+v_2\sigma_3+v_3 \tag{25.3}$$

where a_1 = 3.42, a_2 = 68.16 kPa, c_1 = -0.1785 kPa^{-1}, c_2 = 38.836, c_3 = -707.82 kPa, v_1 = -0.0228 kPa^{-1}, v_2 = 5.67, and v_3 = -85.6 kPa. Figure 2.10 shows a comparison between model predictions and data for the confining pressure σ_3 = 93 kPa. According to the constitutive model under confined conditions, the evolution equation for shear strains is:

$$\varepsilon_1-\varepsilon_3=qg(p,q) \tag{26}$$

where ε_1 denotes the axial strain, ε_3 is the radial strain, $p=(\sigma_1+2\sigma_3)/3$ and $q=\sigma_1-\sigma_3$. Thus, the specific expression of $g(p,q)$ can be obtained by approximating the stabilization boundary.

For silica, it is found that under a given confining pressure σ_3 =constant, the following polynomial law fits the data well

$$g(q) = m_1 q^5 + m_2 \tag{27}$$

where m_1 and m_2 are constants. The variation of m_1 and m_2 with the confining pressure is well approximated by

$$m_1 = m_1(\sigma_3) = \frac{t_1}{t_2 + \sigma_3^5} \tag{28.1}$$

$$m_2 = s_1 \exp(s_2 \sigma_3) \tag{28.2}$$

where t_1 = 3.133·10^{-6}, t_2 = 8.1107·10^5, s_1 = 0.0022 and s_2 = -0.0255.

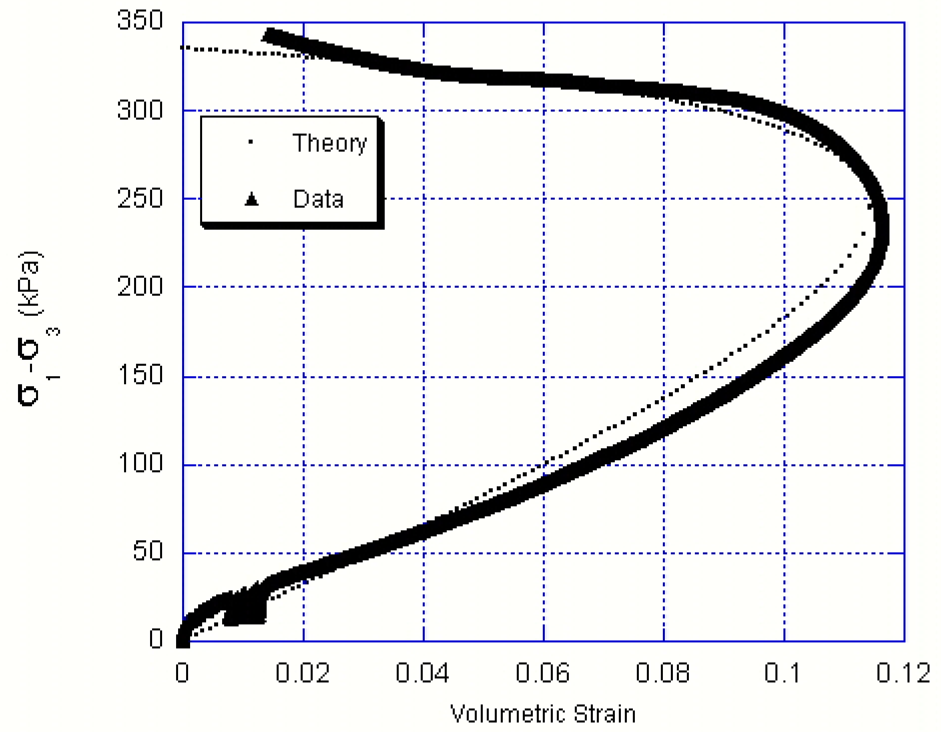

Figure 2.10: Comparison between model prediction and data under σ_3 = 93 kPa

.

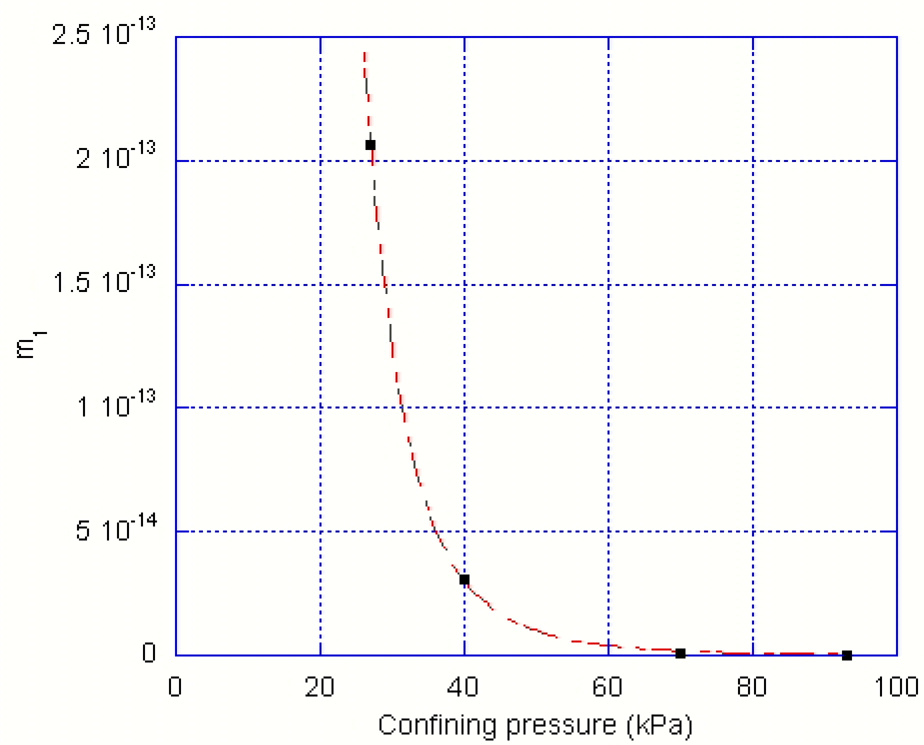

Figure 2.11: Comparison between the theoretical variation of the parameter m_1 and data (symbols).

II.5. Summary and conclusions

An enhanced triaxial testing device has been used to investigate the quasi-static behavior of several cohesive systems under dry conditions: (i) *silica* (silicon dioxide, floated powder) of *spherical* shaped particles having a mean particle size of 63.5 μm; (ii) *polyethylene pellets*, *cylindrical* in shape (4 millimeters in height by 3 millimeters in diameter), and (iii) microscrystalline cellulose, PH-105, of angular shape and mean particle size 20μm.

Based on the test results, we have adopted an elastic/plastic approach to characterize the inviscid behavior. The model describes particularly well the effect of confining pressure on the volumetric strains. The non-linearity, stress-path dependency and the gradual change from compressible to dilatant behavior were correctly modeled. It was thus demonstrated that the theory is applicable to silica for general 3-D conditions.

To describe time effects on the material behavior, a general 3 -D quasi-linear viscoelastic constitutive model was proposed. Contrary to existing rate-type constitutive equations, this model predicts a dependency of the volumetric strain on both the deviatoric (shear) stress components and mean pressure. Furthermore, it was shown that by a judicious choice of the mathematical expressions of the relaxation boundaries both compressibility and dilatancy as well as instantaneous failure could be well predicted. A procedure for the determination of the material parameters based on a minimal set of data was provided. A very good comparison was found between the model prediction and data.

Based on the test results on the PE pellets it can be concluded that under hydrostatic compression the stress-strain response is linear and elastic. Under deviatoric conditions, the main characteristics of the response are: non-linearity, stress-path dependency, and gradual change from compressibility to dilatancy with increasing deviatoric stresses. The time influence on the behavior was revealed in creep tests as well as in tests performed at different strain rates. It was found that the time dependent properties depend on the loading history. However, short-term time effects can be neglected and the behavior can be described accurately using a single surface, Lade type elastic-plastic theory. It was demonstrated that this theory captures the change in volumetric deformation mechanisms with the increase in the applied deviatoric stress. The increase in the value of the dilatancy threshold level with increasing confining pressure is particularly well described.

Long-term (over 24hrs) creep test results showed a marked difference between axial and volumetric creep behavior. Furthermore, the volume viscosity is not constant, but depends on the current density (or level of compaction). Clearly, such effects cannot be described in the framework of viscoplasticity theory, which is based on the concept of overstress and where the yield and potential have the same mathematical expressions as the yield and potential for inviscid behavior. However, a viscoplastic fluid type formulation should be more appropriate. Additional rheological measurements would be required for the development and calibration of such a model.

References Section II

Abdel-Hadi, A. I., Cristescu, N. D., Cazacu, O. and Bucklin, R A, 2000. Development of a new technique for measuring volume change of dry particulate systems under very low confining pressures, in: Kraisheh, M. K., Godfrey, T. A., Willam, K. J. (Eds.), Recent Trends in Constitutive Modeling of Advanced Materials, Proceedings of the 2000 ASME Intl Mechanical Engineering Congress and Exposition, November 5-10, 2000, Orlando, Florida, AMD -Vol. 239, pp. 69-75.

Abdel-Hadi A.I., Zhupanska O.I. and Cristescu, N.D., 2002. Mechanical Properties of Microcrystaline Cellulose. Part I. Experimental Results. Mech. Mater. 34, 373-390.

Ahadi, A., Krenk, S., 2003. Implicit Integration of Plasticity Models for Granular Materials, Comput. Methods. Appl. Mech. Eng. 192, 3471-3488.

Alawaji, H., Runnesson K., Sture S. and Axelsson K., 1992. Implicit Integration in Soil Plasticity under Mixed Control for Drained and Undrained Response. Int. J. Numer. Anal. Met. 16, 737-756.

Aydin, I., Bricoe, B., Sanliturk, K.Y.1996. The Internal Form of Compacted Ceramic Components: A Comparison of a Finite Element Modeling with Experiment. Powder Technol. 89, 239-254.

Bardett, J., Lode, P., 1990. Dependencies for Isotropic Pressure-Sensitive Elastoplastic Materials. J Appl. Mech.T ASME. 57 (3), 498-506.

Borja, R. I., Sama, K. M., Sanz, P. F., 2002. On the Numerical Integration of Three-Invariant Elastoplastic Constitutive Models. Comput. Methods. Appl. Mech. Eng., 192 1227-1258.

Cazacu, O., Jin, J., Cristescu, N.D., 1977. A new constitutive model for alumina powder compaction. KONA, 15, 103-112.

Chtourou, H., Gakwaya, A., Guillot M., 2002. Modeling of the Metal Powder Compaction Process Using the Cap Model. Part I. Experimental Material Characterization and Validation. Int. J. Solids. Struct.. 39, 1059-1075.

Drescher, A., 1998. Some aspects of flow of granular materials in hoppers. Phil. Trans. R. Soc. Lond. A, 356, 2649-2666.

Gethin, D. T., Lewis, R. W., Tran, D. V., Ariffin, A. K., 1994. Finite Element Modeling of Multilevel Compaction of Powders, Adv. Powder Metall. Part. Mater. 7, 13-22.

Jin , J., Cristescu, N.D., 1998. A constitutive model for powder materials. J Eng. Mater. Technol Trans ASME. 120, 97-104.

Kandala, R.N., Puri, V.M., 2000. Measurement of cohesion and angle of internal friction using cubical triaxial tester and comparison with computer controlled shear cell, Particul. Sci. Tehnol. 18 (2), 71-88.

Lade, P. V., 1975. Elastoplastic stress strain theory for cohesionless soil. J. Geotech. Eng. ASCE. 101, 1037-1053.

Lade, P. V., 1977. Elasto-plastic stress-strain theory for cohensionless soil with curved yield surface, Int. J. Solids. Struct., 13, 1014-1035.

Lade P. V and Kim M. K. 1995. Single hardening constitutive model for soil, rock and concrete. Int. J. Solids. Struct., 37, 6343-6360.

Ortiz, M., Simo, J.C.,1986. An analysis of a new class of integration algorithms for elastoplastic constitutive relations, Int J Numer Meth Eng. 23, 353-366.

Peric, D., Ayari, M. A., 2000. Influence of Lode’s Angle on the Pore Pressure Generation in Soils, Int. J. Plasticity. 18, 1039-1059.

Roscoe, K.H., Burland, J. B., 1968. On the generalized stress-strain behavior of wet clays Engineering Plasticity, J. Heyman and F. A. Leckie, Eds, Cambridge University Press, Cambridge, England.

Sato, H., Shimoyama, M, Kamiya, T,. 2002 .Raman spectra of high-density, low-density, and linear low-density polyethylene pellets and prediction of their physical properties by multivariate data analysis. J Appl. Polym. Sci. 86 (2), 443-448.

Saxena, S. K., Reddy, R .K., Sengupta, A., 1988. Verification of a constitutive model for granular materials in: Saada, A., Bianchini,G. (Eds.). Constitutive Equations for Granular Non-Cohesive Materials, Balkema, Rotterdam.

Trasorras J., Krauss, T. M., Ferguson B. L., 1989. Modeling of Powder Compaction Using the Finite Element Method. Adv Powder Metall Part Mater. 1, 85-104.

Puri, V.M., Tripodi, M.A., Manbeck, H.B., Messing, G.L. 1995. Constitutive model for dry cohesive powders with applications to powder compaction. *KONA*,13, 135-150.

Verwijs, M.J., Janssen, R.J.M., Scarlett, B., 2002. Influence of the intermediate principal stress during powder shear in a biaxial tester. In: Proceedings of the World Congress of Technology of Particles. Sydney, Australia, July 2002 (CD-ROM).

Wan, R. G. and Guo, P.J., 1999. Modelling stress dilatancy response of sand along imposed constant strain-increment-ratio paths. in. Eds: Picu, R. C., Krempl, E. (Eds.) 4th International Congress on Constitutive Laws for Engineering Materials, July 27-30, 1999, Rensselaer Polytechnic Institute, Troy, New York.

Zhang, Q., Puri, V. M., Manbeck, H. B., 1986. Determination of elastoplastic constitutive parameters for wheat en Masse. Trans. ASAE. 29 (6), 1739-1547.

TASK 3: ANALYSIS OF THE STEADY-STATE FLOW OF A COMPRESSIBLE POROUS VISCOPLASTIC MEDIUM

III.1. Introduction

The focus of this task was on describing steady flow of a compressible porous viscoplastic medium over a penetrator. The influence of the characteristics of the penetrator/target interface, impact velocity, target mechanical properties and nose geometry on the resistance to penetration is investigated.

Penetration mechanics has a long and rich history. A comprehensive review of empirical equations for the maximum penetration depth in rock, concrete, soil, ice, and marine sediments can be found in Heuze (1970), Zukas (1990), *etc*. The maximum penetration depth is expressed as a function of initial impact velocity, penetrator cross-sectional area, penetrator weight, and /or nose geometry. However, in these equations the only target material properties considered are the initial density and unconfined strength.

A large number of semi-analytical models where penetration is idealized as uniform expansion of a spherical or cylindrical cavity into a semi-infinite target have been proposed (*e.g*. Goodier (1965), Hanagud and Ross (1971), Forrestal and co-workers (*e.g*. Forrestal et al. (1988))). These cavity expansion analyses provide the radial stress at the cavity surface as a function of the cavity velocity and acceleration. This radial stress is considered to be the load on the penetrator and is subsequently used in conjunction with equations of motion to calculate the maximum depth of penetration. As emphasized in recent contributions, good agreement between model and data can be expected only if the compressibility and rate sensitivity of the target material are accounted for (see for example, Warren and Forrestal (1998)).

As part of this research effort, a new model for calculating the resistance to penetration into geological or geologically derived materials was proposed. In the analysis it is assumed that the rate of penetration and all flow fields are steady as seen from the tip of the penetrator.

This hypothesis is supported by penetration tests into cementitious materials (grout, concrete) for impact velocities below 1000 m/s. The shear response of the target material is modeled by a modified Bingham type viscoplastic equation proposed by Cazacu and Cristescu (2000) and Cristescu *et al.* (2002). The rationale for adopting such a model is that it accounts for both strain rate and compaction effects on yielding, which are key properties of any porous/brittle material. In the low-pressure regime, a non-linear pressure-volume relationship is considered. Based on experimental observations (*e.g*. Schmidt (2003)) which show that in the high-pressure regime a very large increase in pressure is necessary to produce even a very small change in density, the hypothesis of a "locking medium" is adopted: the density cannot exceed a critical value. The penetrator is wedge-shaped with a high length-over-diameter ratio. Contact between the projectile nose and target is considered to be of Coulomb type with constant friction coefficient, whereas the frictional contact between the remainder of the projectile and target is considered to be velocity dependent. Resistance to penetration is calculated for different interface conditions between the target and wedge. It is shown that for low to intermediate impact velocities, accounting for friction results in blunter optimal wedge geometry for optimal penetration performance. Furthermore, the higher the velocity, the greater is the influence of nose geometry (wedge semi-angle) on penetration. Finally, an application of the proposed model to a cementitious material is presented.

III. 2. Constitutive model for the target

The deviatoric response of the target material is modeled by a non-homogeneous Bingham type rigid/viscoplastic equation proposed by Cazacu and Cristescu (2000) (see also Cristescu *et al.* (2002)). The following notations are used: $\langle \; \rangle$ denotes the Macauley bracket with $\langle A \rangle = \frac{1}{2}\left(A + |A|\right)$ being the positive part of the real number A , $\boldsymbol{\sigma}$ is the Cauchy stress tensor, $\boldsymbol{S}$ its deviator, $\boldsymbol{I}$ the unit second order tensor ($I_{ij} = \delta_{ij}$, i, j =1…3) and p is the mean stress (i.e. $\sigma_{ij} = S_{ij} + p\delta_{ij}$). Let $\boldsymbol{D'}$ denote the deviator of the rate of deformation tensor $\boldsymbol{D}$ defined as the symmetric part of the spatial gradient of velocity and by

$II_{D'} = \frac{1}{2} D'_{ij} D'_{ij}$ its second invariant.

According to the model (Cazacu and Cristescu (2000)):

$$\boldsymbol{D}' = \begin{cases} 0 & if \quad II_S \le k^2(\rho), \\ \frac{1}{2\eta} \left\langle 1 - \frac{k(\rho)}{\sqrt{II_S}} \right\rangle \boldsymbol{S} & if \ II_S > k^2(\rho). \end{cases} \tag{1}$$

The influence of the degree of compaction on the behavior is modeled through the dependence of the yield limit in shear, k, on the current density ρ. Thus, for stress states satisfying $II_S \le k(\rho)^2$ the model response is rigid, otherwise the model response is viscoplastic. A power law variation of the yield limit with the current density is assumed

$$k(\rho) = k_0 + \beta \left(1 - \frac{\rho_0}{\rho} \right)^n, \tag{2}$$

where ρ_0 and $k_o = k(\rho_0)$ are the density and yield stress of the undeformed medium, respectively, while n and β are material constants. The yield stress k is given in stress units and η in Poise. The stress-volume relationship adopted reflects the following experimental observations (see Schmidt (2003)):

- In the low to moderate pressure regime, most cementitious materials show a highly non-linear mean stress-volumetric strain response, the reversible decrease in volume being very small,
- In the high-pressure regime, a very large increase in pressure is necessary in order to produce even a very small change in volume.

Thus, the hypothesis of a “locking medium” applies, *i.e*. the density cannot exceed a critical value. This critical density, called locking density, is the density at which no volume change occurs under hydrostatic conditions. It will be denoted by ρ_* and the pressure level at which this density is first reached, called locking pressure, is denoted by p_*.

Hence, $\rho = \rho_*$ for $p > p_*$ while for $\rho \le \rho_*$, the pressure vs. density relationship $p = p(\rho)$ is assumed to be of the form

$$p(\rho) = p_* \left(\frac{\rho}{\rho_*} \right)^m \tag{3}$$

where *m* is a material constant. The relationships (1)-(3) could be inverted, to give:

$$\boldsymbol{\sigma} = \begin{cases} p(\rho)\boldsymbol{I} + \left(2\eta + \dfrac{k(\rho)}{\sqrt{II_{D'}}} \right)\boldsymbol{D'} & \text{for} \quad \boldsymbol{D'} \neq 0, \\ p(\rho)\boldsymbol{I} & \text{for} \quad \boldsymbol{D'} = 0. \end{cases} \tag{4}$$

Note that the model accounts for both rate dependency and compaction effects on yielding, which are key properties of any cementitious or geologic materials.

III. 3. Computation of the resistance to penetration at steady-state

III. 3.1. Statement of the problem

Generally, post-test observations of gun launch penetration experiments in geologic or cementitious materials (grout, concrete) indicate that there are four stages of the penetration event (see Jones *et al.* (1998)). The first stage corresponds to nose penetration when the target material is restrained from large movements; the second stage corresponds to chipping and cratering at the point of impact; the third stage occurs when the projectile is fully embedded and the pusher plate hits the target and strips off, while the fourth stage occurs when the full length of the projectile is in the penetration channel or tunnel created by the penetrator.

The analysis presented in this paper concerns the steady-state flow of the target material over a projectile fully embedded in the target (*i.e.* fourth stage of penetration). The penetrator is considered to be rigid and wedge-shaped. Post-test observations indicate that for impact velocities up to 1000 m/s, penetration paths are relatively straight and stable with regard to the original shotline (see Jones *et al.* (1998)). Thus, we can assume that the problem is axi-symmetric with respect to the wedge centerline. Let $D = D_0 \cup D_{visco} \cup D_f$ denote the domain occupied by the penetrator and the target material around it (see Figure 3.1). The lateral extent of this domain is $F \cdot R$, where R is the wedge semi-height and F is a number estimated from post-test observations. In the domains D_0 and D_f (i.e. in front of and behind the penetrator), it is assumed that the target material is in rigid body motion while in the domain D_{visco} the material undergoes viscoplastic deformation. We further suppose that in D_{visco} the flow lines are centered at a certain pole O. Hence, the viscoplastic domain D_{visco} is bounded by the nose surface, Γ_1, MP, and the two surfaces S_0 and S_f. The surface S_f is of radius $OP \equiv r_f = \frac{R}{\sin\alpha} F$, while the surface S_0 is of radius $OM \equiv r_0 = \frac{R}{\sin\alpha}(1+\mathrm{F})$ (see Figure 3.1).

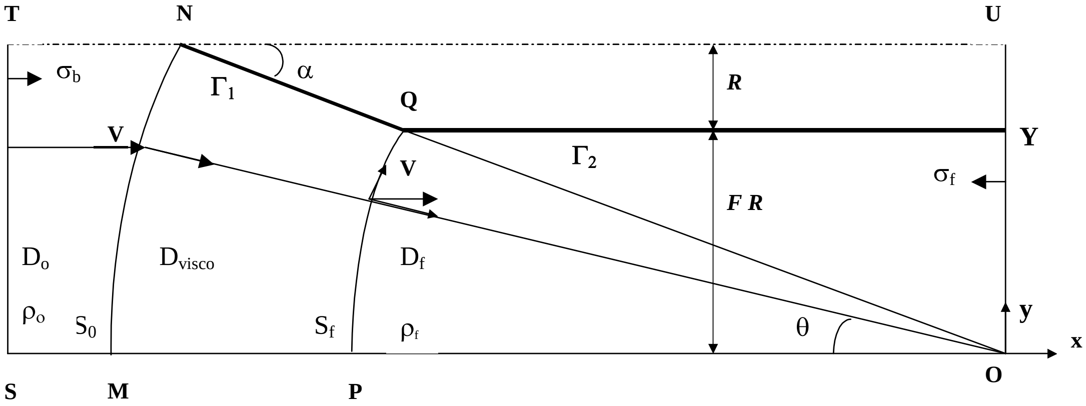

Figure 3.1: Schematic of the flow over the wedge.

We assume that there exists velocity discontinuities tangent to the surfaces S_0 and $S_{f,}$ while the components of velocity normal to these surfaces are continuous. Since across S_0

$$\left[\vec{V}\right]\cdot \vec{n} = 0 , \qquad (5)$$

with $\vec{n}$ the outward normal unit vector, it follows that in the viscoplastic domain, D_{visco}, the only non-zero velocity component is the radial component,

$$V_r = V \cos\theta , \quad 0 \le \theta \le \alpha \qquad (6)$$

and consequently the only non-zero components of the rate of deformation are

$$D_{\theta\theta} = \frac{V \cos\theta}{r}$$

and

$$D_{r\theta} = -\frac{V \sin\theta}{2r} \quad . \qquad (7)$$

The continuity equation reduces to:

$$\frac{\partial}{\partial r}\left(r\rho\right) = 0 \qquad (8)$$

Since $\rho = \rho_0$ on S_0, in the viscoplastic domain,

$$\rho = \frac{r_0}{r}\rho_0 , \qquad (9)$$

Obviously, the compaction law (9) could also be obtained by imposing that the velocity be the same in the domains D_0 and D_f (debit compatibility). In the following, we estimate the resistance to penetration based on energy considerations. The wedge semi-angle that minimizes the resistance to penetration is then determined for different interface conditions between the wedge and the target.

III. 3.2. Friction laws

Along the surface of the wedge significant friction arises. The mechanics of friction at high sliding speeds is very complex. Much of the work reported is at lower speeds or pressures than those occurring during a penetration event. In view of this, in our analysis we assume that a Coulomb friction law applies along Γ_1, the surface area of contact between the nose of the rigid projectile and the target, *i.e.*

$$\tau = \mu\sigma_n, \tag{10}$$

where τ is the shear stress in the deformed material, μ is a friction coefficient taken as constant, and σ_n is the normal pressure between the nose and the target material.

In plastic forming of metals, when one body is fully plastic and the other is rigid, a friction law of the form (see Avitzur (1968)),

$$\tau = \mu_r\sigma_Y/\sqrt{3}, \tag{11}$$

is often assumed where τ is the shear stress in the deformed material, μ_r is a friction coefficient taken constant and σ_Y is the yield limit of the material. In general, $0 \le \mu_r \le 1$, where the case $\mu_r = 0$ corresponds to "no friction", while $\mu_r = 1$ corresponds to adherence of the plastic body to the rigid die wall. Hence, according to the friction law (11) irrespective of the normal pressure between the two bodies, the shear stress is constant. The density of the target material behind the penetrator is: $\rho = \rho_f$, where $\rho_f = \rho\big|_{r=r_f}$ while the state of stress is such that $\sqrt{II_S} = k(\rho_f)$ (i.e. on the yield surface). Thus, it can be assumed that the contact between the rigid penetrator and the compacted material behind the penetrator is described by a law similar to (11), i.e.

$$\tau = \mu_r k(\rho_f) \tag{12}$$

III. 3.3. Resistance to penetration

The law of conservation of energy is used to compute the resistance to penetration. In the domains D_0 and D_f , no deformation occurs and therefore no internal power dissipation is involved. In the viscoplastic domain, the stress power per unit volume, $\boldsymbol{\sigma} : \boldsymbol{D}$ can be expressed as

$$\boldsymbol{\sigma} : \boldsymbol{D} = \sigma_{ij} D_{ij} = (4\eta) II_{D'} + 2\, k\left(\rho\right) \sqrt{II_{D'}} + p \cdot trD \tag{13}$$

Using the work-hardening law (2) in conjunction with the radial compaction law (9), we obtain:

$$\begin{aligned} \boldsymbol{\sigma} : \boldsymbol{D} = {} & \eta \frac{V^2}{r^2} \left(\frac{3 + \cos^2\theta}{3} \right) + \left[k_0 + \beta \left(1 - \frac{r}{r_0} \right)^n \right] \frac{V}{r} \sqrt{\frac{3 + \cos^2\theta}{3}} \\ & + p_* \left(\frac{\rho_0}{\rho} \right)^m \left(\frac{r_0}{r} \right)^m \frac{V \cos\theta}{r} \end{aligned} \tag{14}$$

Integrating over D_{visco}, we arrive at: $\dot{W} = \int\limits_{D_{visco}} \boldsymbol{\sigma} : \boldsymbol{D}\, dV = \int\limits_{r_f}^{r_0} \int\limits_{0}^{\alpha} (\boldsymbol{\sigma} : \boldsymbol{D})\, r\, d\theta\, dr$, or

$$\dot{W} = \eta \frac{V^2}{6} (7\alpha + \sin\alpha \cos\alpha) \ln\left(\frac{r_0}{r_f} \right) +$$

$$\frac{V}{\sqrt{3}} F(\alpha) \left[k_0 (r_0 - r_f) + \beta \frac{r_0}{n+1} \left(1 - \frac{r_f}{r_0} \right)^{n+1} \right] +$$

$$p_* \frac{V \sin\alpha}{m-1} \left(\frac{\rho_0}{\rho_*} \right)^m r_0 \left[\left(\frac{r_0}{r_f} \right)^{m-1} - 1 \right],$$

where $F(\alpha) = \int\limits_0^{\alpha} \sqrt{3 + \cos^2\theta}\, d\theta$. (15)

The surfaces S_0 and S_f are surfaces of velocity discontinuity. The power dissipated at the crossing of these surfaces is: $\dot{W}_{S_0,S_f} = \int\limits_{S_0} \vec{t}\cdot[\vec{\mathrm{v}}]dA + \int\limits_{S_f} \vec{t}\cdot[\vec{\mathrm{v}}]dA$, where $\vec{t}$ is the stress vector while $[\vec{\mathrm{v}}]$ is the jump in velocity across the respective surface. Since the magnitude of the tangential jump is $V\sin\theta$, we obtain:

$$\dot{W}_{S_0} = \int\limits_{S_0} \vec{t}\cdot[\vec{\mathrm{v}}]dA = \int\limits_0^{\alpha} \sigma_{r\theta} V \sin\theta \, r_0 \, d\theta = -\frac{\eta V^2}{2}\left(\alpha - \sin\alpha\cdot\cos\alpha\right) - r_0 k_0 \left(V\sqrt{3}\right) F_1(\alpha),$$

$$\begin{aligned}\dot{W}_{S_f} &= \int\limits_{S_0} \vec{t}\cdot[\vec{\mathrm{v}}]dA = \int\limits_0^{\alpha} -\sigma_{r\theta} V \sin\theta \, r_f \, d\theta = \frac{\eta V^2}{2}\left(\alpha - \sin\alpha\cdot\cos\alpha\right) + \\ &\left[k_0 + \beta\left(1 - \frac{r_f}{r_0}\right)^n\right]\left(V\sqrt{3}\right)F_1(\alpha)\end{aligned} \tag{16}$$

where $F_1(\alpha) = \int\limits_0^{\alpha} \frac{\sin^2\theta}{\sqrt{3+\cos^2\theta}} d\theta$. Assuming Coulomb friction (see (10)) along Γ_1, the surface area of contact between the nose of the rigid projectile and the target, the dissipation due to friction is:

$$\begin{aligned}\dot{W}_{\Gamma_1} &= \mu \int\limits_{r_0}^{r_f} (V\cos\alpha\cdot\sigma_{\theta\theta}\big|_{\theta=\alpha})dr = \\ &\mu V\cos\alpha\left\{\frac{4}{3}V\cos\alpha + \eta\ln\left(\frac{r_0}{r_f}\right) + \frac{4}{3}\frac{\cos\alpha}{\sqrt{3+\cos^2\alpha}}\left[k_0\left(r_0 - r_f\right) + \beta\frac{r_0}{n+1}\left(1-\frac{r_f}{r_0}\right)^{n+1}\right]\right\} \\ &+ \mu V\cos\alpha\cdot\frac{p_*}{m-1}\left(\frac{\rho_0}{\rho_*}\right)^m r_0\left[\left(\frac{r_0}{r_f}\right)^{m-1} - 1\right]\end{aligned} \tag{17}$$

Assuming that the friction law (11) applies along Γ_2, the surface area of contact between the penetrator and the compacted target material behind it (see Figure 1), then

$$\dot{W}_{\Gamma_2} = \mu_r \int_{\Gamma_2} k(\rho_f) V ds = \mu_r k(\rho_f) VL, \tag{18}$$

where L is the length of the penetrator shank. Next, the theorem of power expanded will be used to compute the resistance to penetration. Consider the control volume $V = D_0 \cup D_{visco} \cup D_f$ *i.e.* in the domain comprised between the planes $x = 0$ and $x = OS$ and $y = 0$ and $y = F \cdot R$, (see Figure 1). At steady state, the stress power theorem writes:

$$\int_{D_{visco}} \boldsymbol{\sigma} : \boldsymbol{D} \, d\,V + \dot{W}_{S_0} + \dot{W}_{S_f} + \dot{W}_{\Gamma_1} + \dot{W}_{\Gamma_2} = \int_{\partial V} (\sigma_b V - \sigma_f V) dA. \tag{19}$$

In (19), σ_b denotes the magnitude of the stress vector acting along the direction of the velocity on the boundary of the domain D_0 (i.e. in front of the penetrator) while σ_f is the magnitude of the stress vector acting on the boundary of D_f. We may assume that $\sigma_f = k(\rho_f)$, where ρ_f is the density of the compacted target material behind the penetrator. Substituting (14) to (18) into (19), we obtain the expression for σ_b, the resistance to penetration, as:

$$\sigma_b = \frac{1}{V(F+1)R} \left(\dot{W} + \dot{W}_{S_0} + \dot{W}_{S_f} + \dot{W}_{\Gamma_1} + \dot{W}_{\Gamma_2} + k(\rho_f) V R F \right) \tag{20}$$

III. 4. Application to concrete (data after Schmidt (2003))

To illustrate the predictive capabilities of the model, we will apply it to concrete. The modeling effort was based on the results of a series of quasi-static compression tests. All quasi-static tests were conducted using a standard fully automated MTS testing machine at a strain rate of approximately $0.77 \cdot 10^{-6}$/s and at confining pressures in the range 0-450 MPa. (Schmidt (2003)). The density of the material is 2 g/cm^3 while the uniaxial compressive strength is 42.2 MPa. The parameters involved in the non-homogeneous Bingham model (see eqs. (1)-(3)) are:

- the viscosity η,

- initial density ρ_0,
- n and β, the coefficients involved in the law of variation of the yield stress $k(\rho)$ (see (2)),
- p_*, ρ_*, m, the parameters involved in the pressure density law (3).

For this material, the locking pressure value is considered to be p_* = 0.5 GPa, a value which is based on post-test data reported by Jones *et al.* (1998). The corresponding locking density ρ_* is estimated using the relationship

$$\rho_* = \rho_0 \frac{1}{1-\varepsilon_V^f}, \tag{21}$$

where $\varepsilon_V^f = 0.068$ corresponds to the volumetric deformation at failure under confinement of 450 MPa. For sake of simplicity, we assume a quadratic dependence of pressure on density (*i.e.* we set m = 2 in (3)). We take the yield limit of the undisturbed medium $k(\rho_0)$ to be equal to the unconfined yield limit, *i.e.* $k(\rho_0)$ = 10 MPa while the yield stress of the compacted target is taken to be $k(\rho_f)$ = FF$\cdot k(\rho_0)$, FF being a parameter, which depends on the impact velocity. Assuming n = 2 in the law of variation of $k(\rho)$, we obtain

$$\beta = \frac{k(\rho_0)(FF-1)}{\left(1-\dfrac{\rho_0}{\rho_f}\right)^2} \tag{22}$$

Next, equation (20) is used to calculate the resistance to penetration. The numerical test cases presented correspond to impact velocities in the range of 300m/s to 1000 m/s. The wedge dimensions are set at: R = 6.35 mm and L = 89 mm. As an example, Figure 3.2 shows (σ_b / p_*), the resistance to penetration normalized by the locking pressure, versus the projectile semi-angle α for an impact velocity V = 300 m/s. Calculations were done for four different values of the coefficient of friction between the wedge tip and target material.

The yield stress of the compacted target $k(\rho_f)$ was considered to be 2.5 $k(\rho_0)$, while the coefficient of friction between the body of the wedge and the target was set to μ_r = 0.6. Note that irrespective of the contact conditions between the wedge and target, there exists a critical angle for which the resistance to penetration is minimum. Keeping all the other parameters the same, the more friction that is present, the blunter the nose required to achieve minimum resistance to penetration (of course, assuming that no erosion takes place and that the nose does not fail). This trend was observed for all impact velocities.

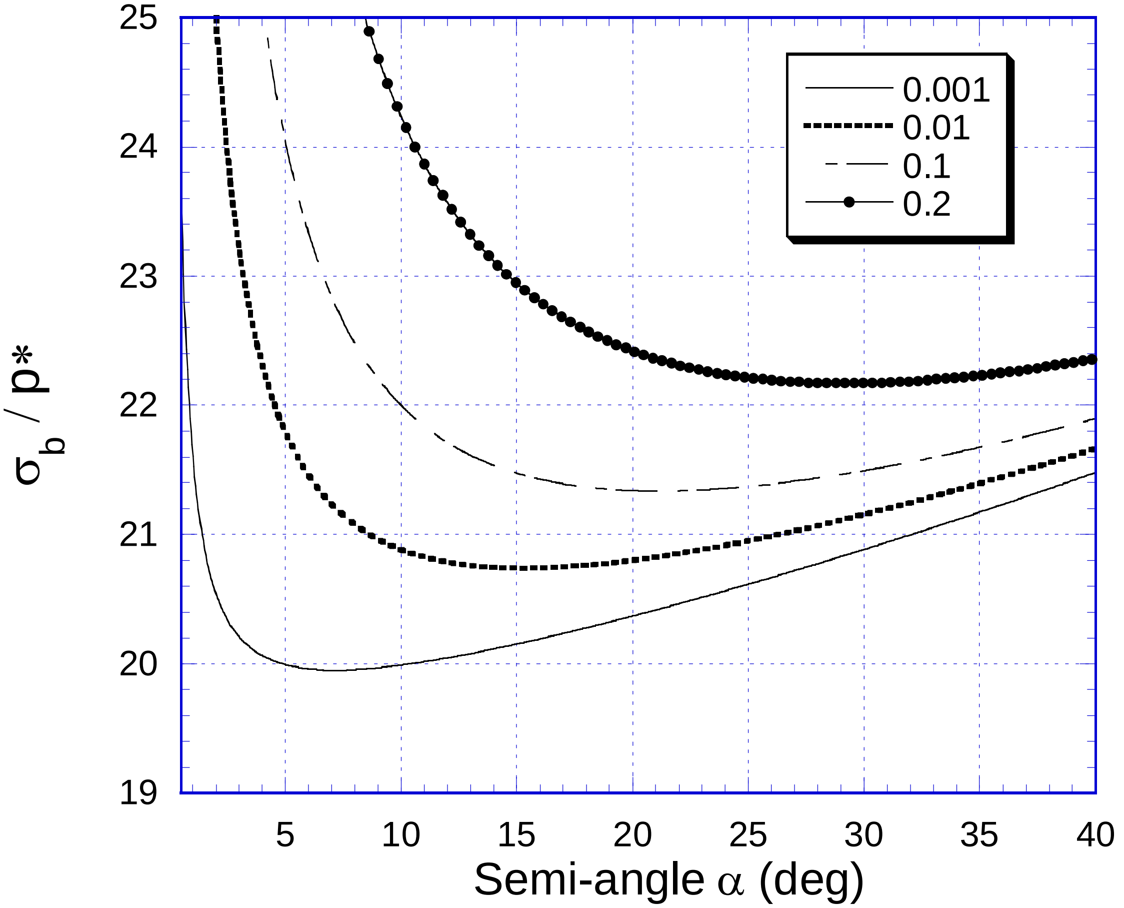

Figure 3.2: Resistance to penetration σ_b normalized by the locking pressure p_* as a function of the projectile semi-angle α for different values of the friction coefficient between the target and the wedge tip; impact velocity V=300 m/s.

The plots of the optimal wedge angle vs. impact velocity for different values of the friction coefficient between the tip and target is presented in Figure 3.3. Since compaction ratios were not available, in the calculations it was assumed that $(k\left(\rho_f\right)/k(\rho_0)$ for an impact velocity of 1000 m/s is double that at 300 m/s impact velocity. The results indicate that at higher impact velocities a sharper nose is required for optimum performance. However, for modest friction ($\mu = 0.01$), the sharpening is minimal.

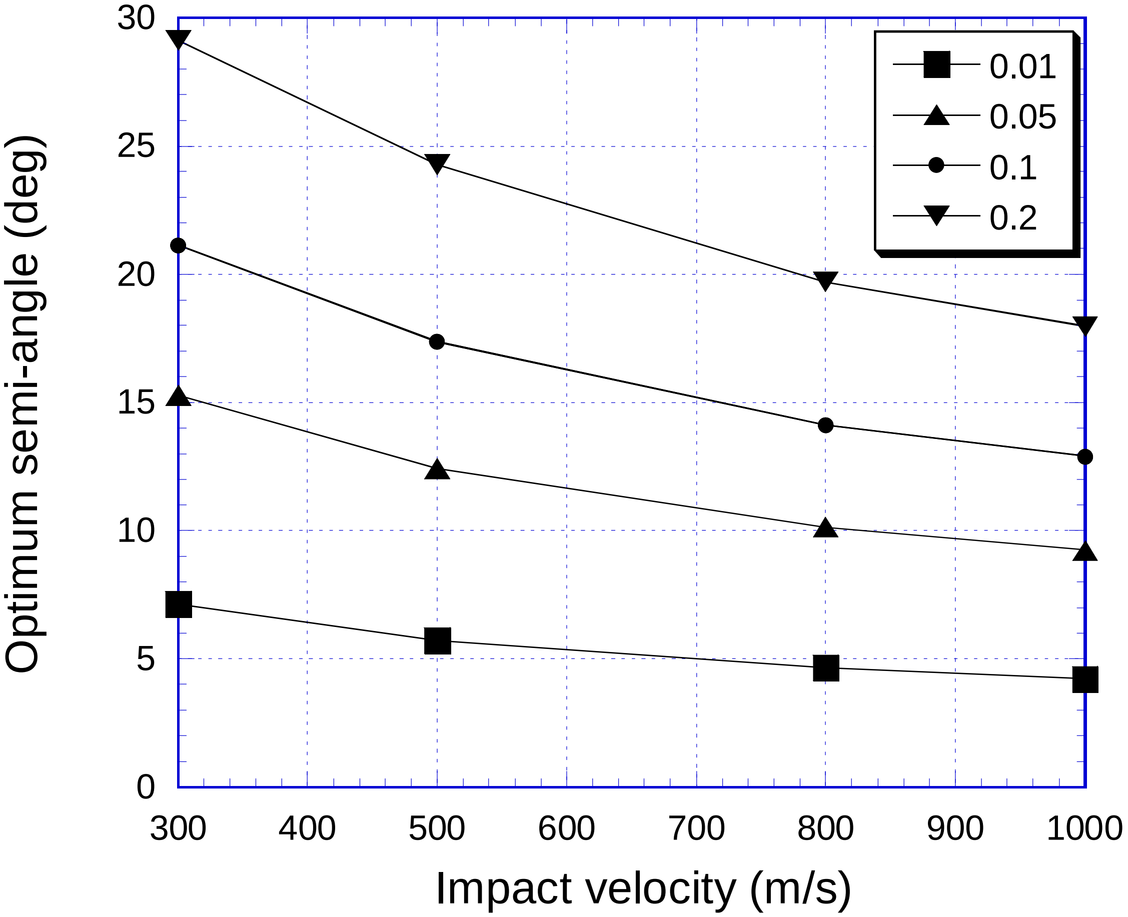

Figure 3.3: Optimum projectile semi-angle vs. impact velocity for various coefficients of friction between the wedge tip and viscoplastic target.

Figure 3.4 shows the resistance to penetration corresponding to optimum wedge angle versus the coefficient μ between the wedge tip and target for different impact velocities. Irrespective of the contact conditions, an increase in resistance to penetration occurs with increased impact velocity.

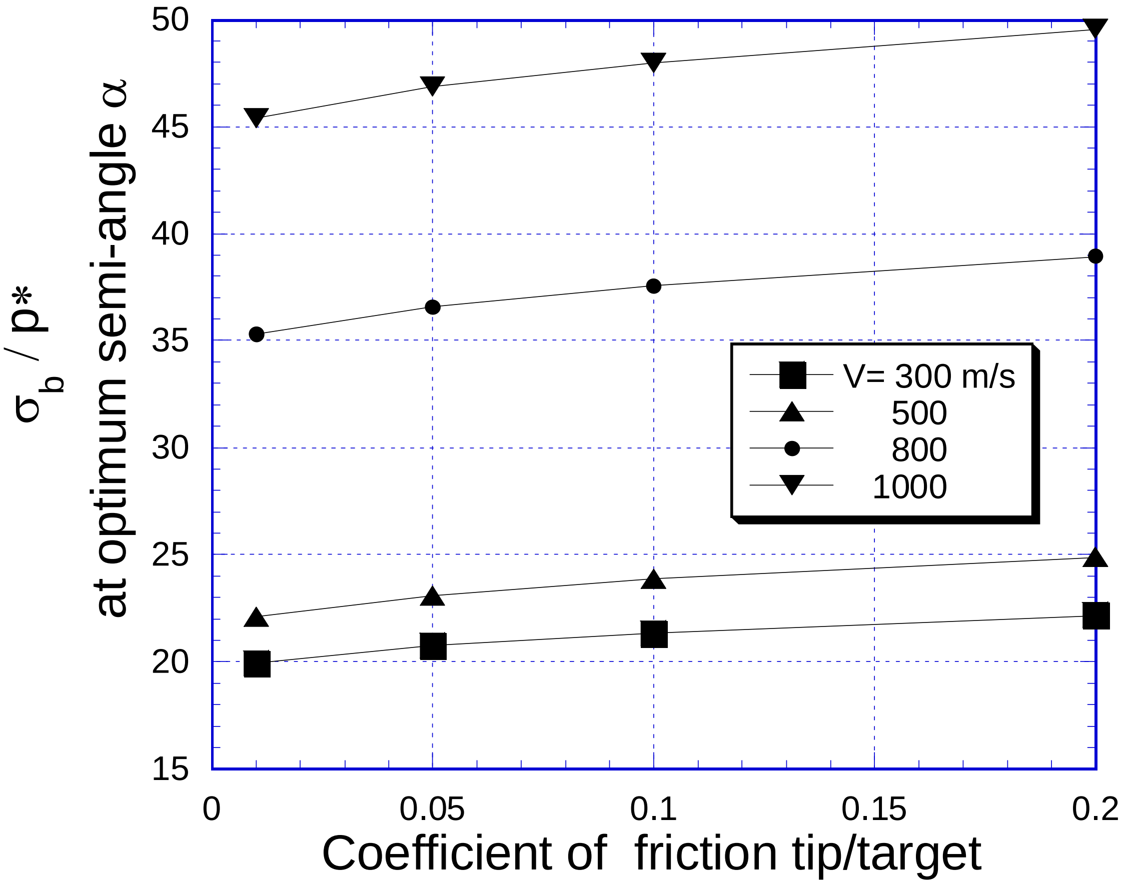

Figure 3.4: Normalized resistance to penetration corresponding to the optimum projectile semi-angle vs. the coefficient of friction between the wedge tip and viscoplastic target for various impact velocities.

III.5 Application to concrete (data from Osborn (1981))

The purpose of this study is to compare the steady-state stresses on the penetrator obtained using hydrocode computations Osborn (1981) to the steady-state stresses obtained using the proposed penetration model. The Osborn (1981) dry concrete model consists of a hydrostat and a fixed yield surface. The hydrostat defines a relationship between pressure and density whereas the yield surface is of Mohr-Coulomb type. The concrete material has an ambient density ρ_0 = 2.2 g/cm^3 and an unconfined strength f_c' = 34.47 MPa. The hydrostatic pressure (in GPa) -volume relationship is given by:

$$p = \begin{cases} 14.4\left(\dfrac{\rho}{\rho_0} - 1\right) & \mathit{if} \quad 0 \le \left(\dfrac{\rho}{\rho_0} - 1\right) \le 0.0025 \\ 0.0358 + 7.862\left[\left(\dfrac{\rho}{\rho_0} - 1\right) - 0.0025\right] & \mathit{if} \quad 0.0025 \le \left(\dfrac{\rho}{\rho_0} - 1\right) \le 0.1 \\ 0.8 + 13\left[\left(\dfrac{\rho}{\rho_0} - 1\right) - 0.1\right] & \mathit{if} \quad 0.1 \le \left(\dfrac{\rho}{\rho_0} - 1\right) \le 0.2 \\ 2.1 + 42\left[\left(\dfrac{\rho}{\rho_0} - 1\right) - 0.2\right] & \mathit{if} \quad 0.2 \le \left(\dfrac{\rho}{\rho_0} - 1\right) \le 0.3 \end{cases} \tag{21}$$

This response curve is plotted in Figure 3.5.

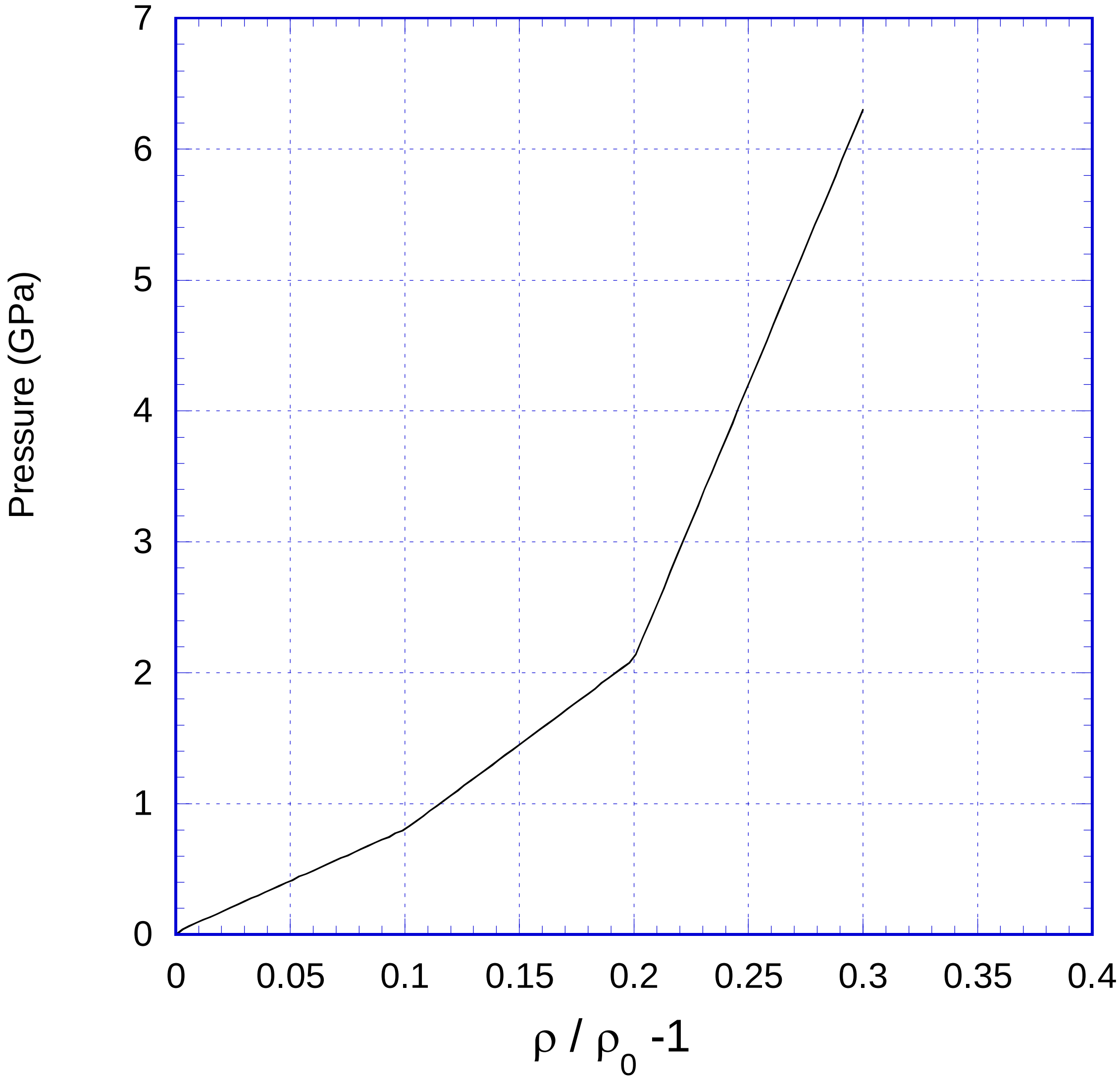

Figure 3.5: Hydrostat for 34.47 MPa concrete (after Osborn (1981).

The yield surface is of Mohr-Coulomb type with a saturation level set at 30.67 f_c'. The yield strength Y is defined by the following equations:

$$Y = \begin{cases} 3.3\left(p + 0.1\, f_c'/3\right) & if \quad -0.1 f_c'/3 < p \le f_c'/3 \\ p + 2 f_c'/3 & if \quad -0.1 f_c'/3 < p \le f_c'/3 \\ 30.67\ f_c' & if \quad 30.67\ f_c' < p \end{cases} \tag{22}$$

We use (21) to determine the material parameters involved in the pressure-density relationship

$$p = p_* \left(\frac{\rho}{\rho_*} \right)^m \qquad (23)$$

Indeed, from (21) it follows that the lock-up density is ρ_* = 2.382 g/cm^3 and the corresponding lock-up pressure is p_* = 6.3 GPa. By least-square fit, we obtain an exponent m =12.104. In Figure 3.6 are plotted together the pressure-density curves given by (21) and (23). No data concerning the dynamic viscosity nor the unconfined yield of the material were available. We assume the yield stress of the undisturbed medium $k(\rho_0)$ to be equal to half the unconfined yield limit, *i.e.* $k(\rho_0)$ = 20 MPa, set n = 2 in the power law variation of the yield stress with density and that the viscosity is the same as for the concrete mix investigated by Schmidt(2003): η = $2 \cdot 10^4$ N·s. The density of the compacted region behind the projectile $\rho_f = \rho|_{r=r_f}$, is $\rho_f = \frac{r_0}{r_f}\rho_0 = \frac{1+F}{F}\rho_0$, where 2 (F+1)R is the extent of the region affected by the impact event. We further assume F = 5, which results in ρ_f = 2.8584 g/cm^3. The dimensions of the penetrator considered in Osborn (1981) are: R = 1 cm, L = 14 cm.

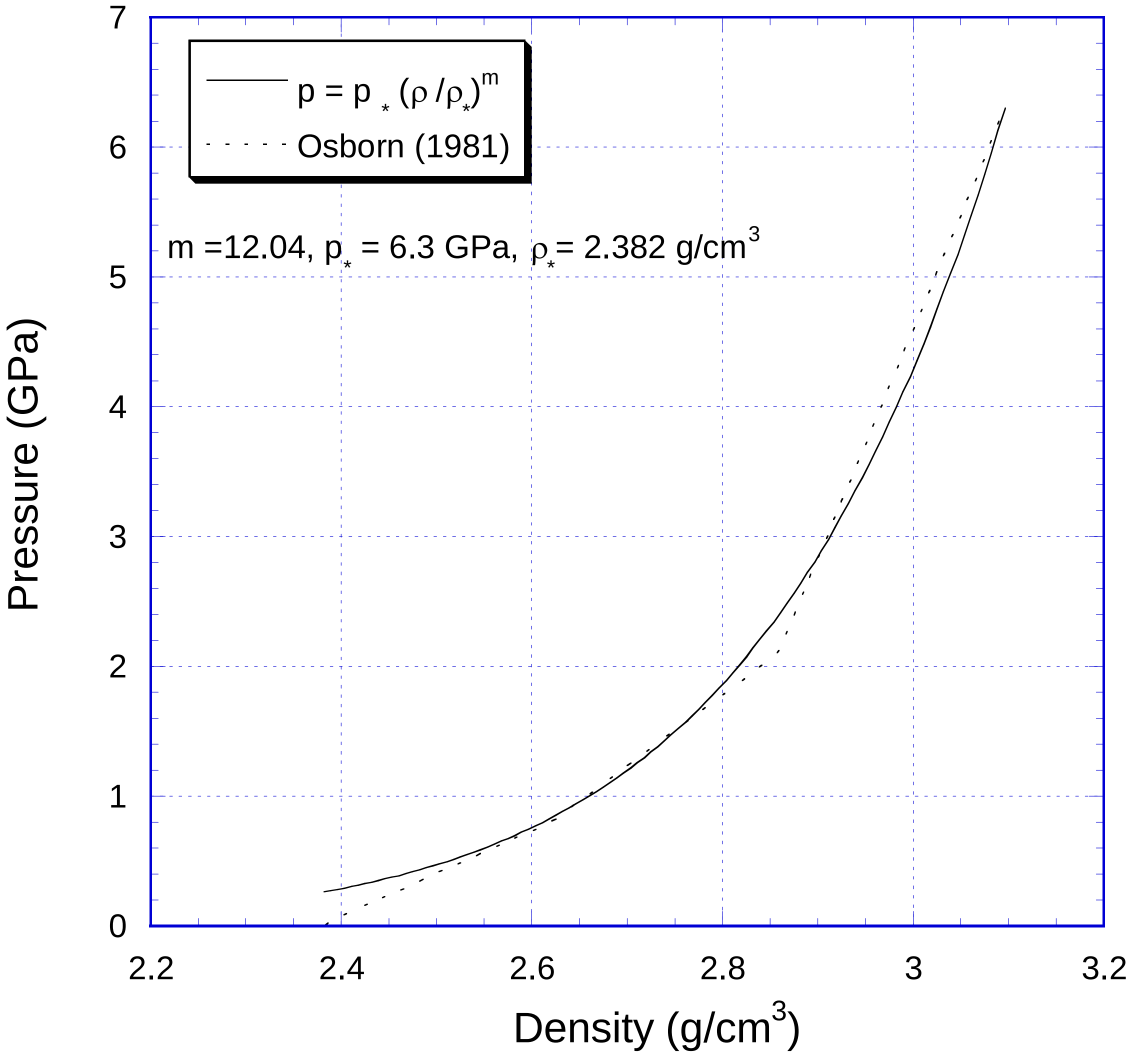

Figure 3.6: Determination of the parameters involved in the pressure-density relationship (3) using Osborn(1981) data for concrete of unconfined strength of 34.47 MPa

Figure 3.7 shows the resistance to penetration normalized by the locking pressure as a function of the projectile half-angle for several different striking velocities V. The yield stress of the compacted target taken in the simulations is: $k\left(\rho_f\right) = 63 \;\; k\left(\rho_0\right) = 1.26$ GPa, the coefficient of friction between the nose and the deformed target was set to μ = 0.2 ,while the coefficient of friction between the shank and the rigid target was $\mu_r = 0.6$.

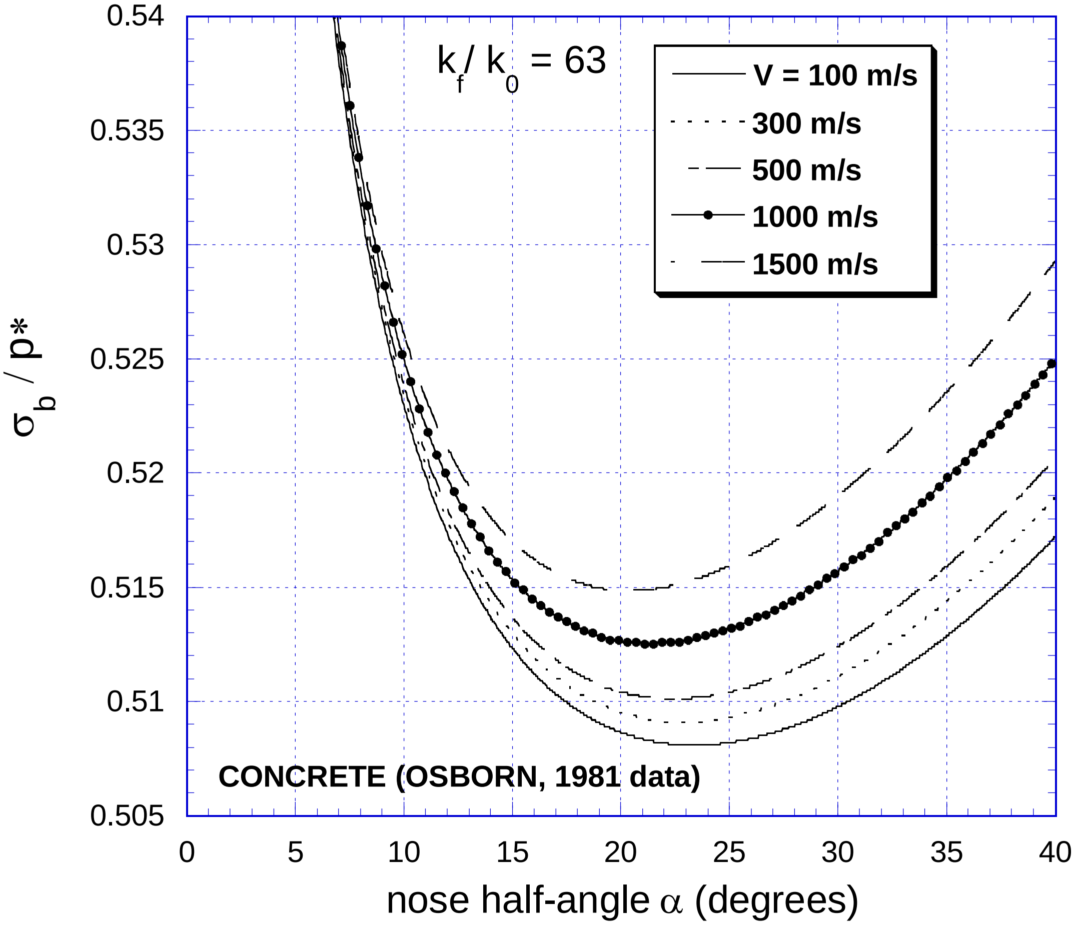

Figure 3.7: Resistance to penetration σ_b normalized by the locking pressure *p** as a function of the projectile semi-angle α for different striking velocities V; $k(\rho_f)$ = $63\,k(\rho_0)$, μ = 0.2 and $\mu_r = 0.6$

The plot of the optimal nose half-angles vs. the corresponding impact velocities is presented in Figure 3.8. Figure 3.9 shows the computed resistance to penetration at optimum angle for several different impact velocities. As expected, an increase in resistance to penetration occurs with increased impact velocity.

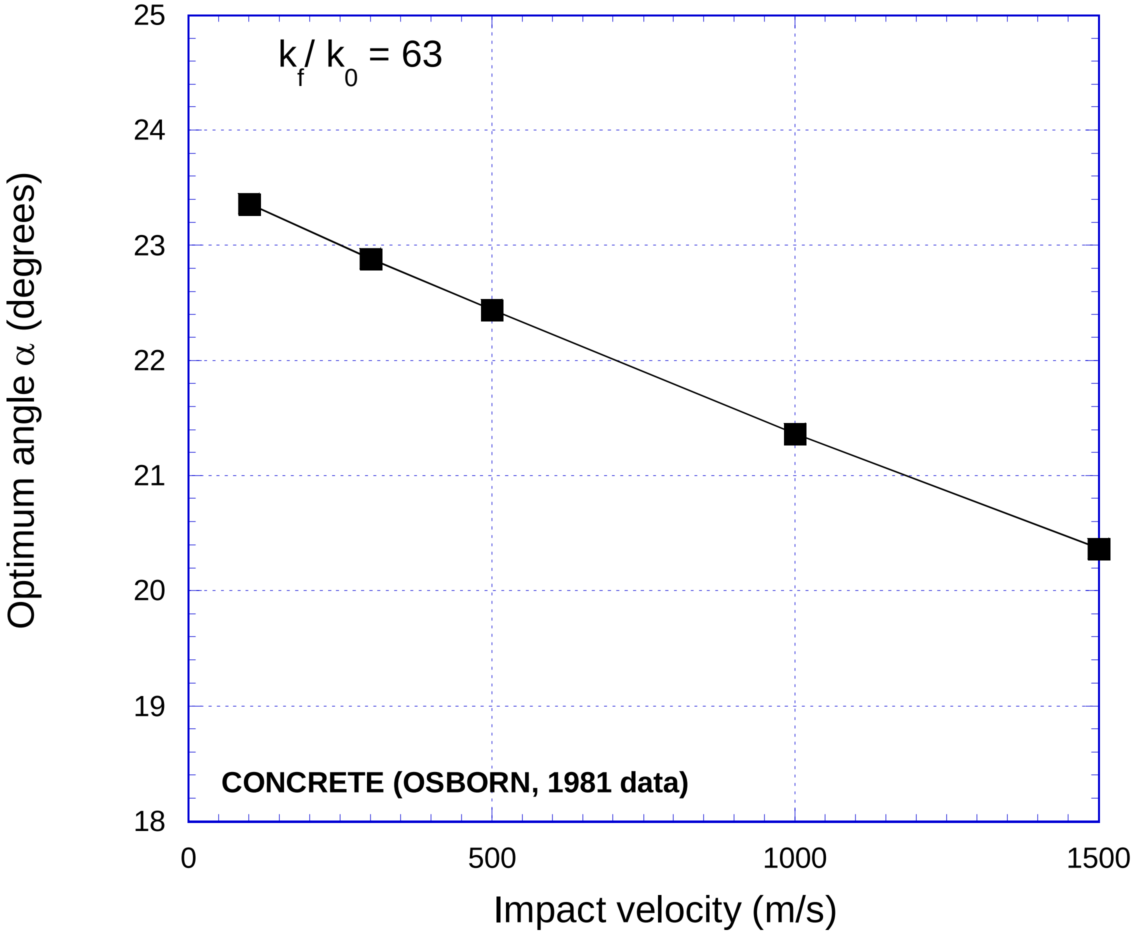

Figure 3.8: Optimum projectile semi-angle vs. impact velocity.

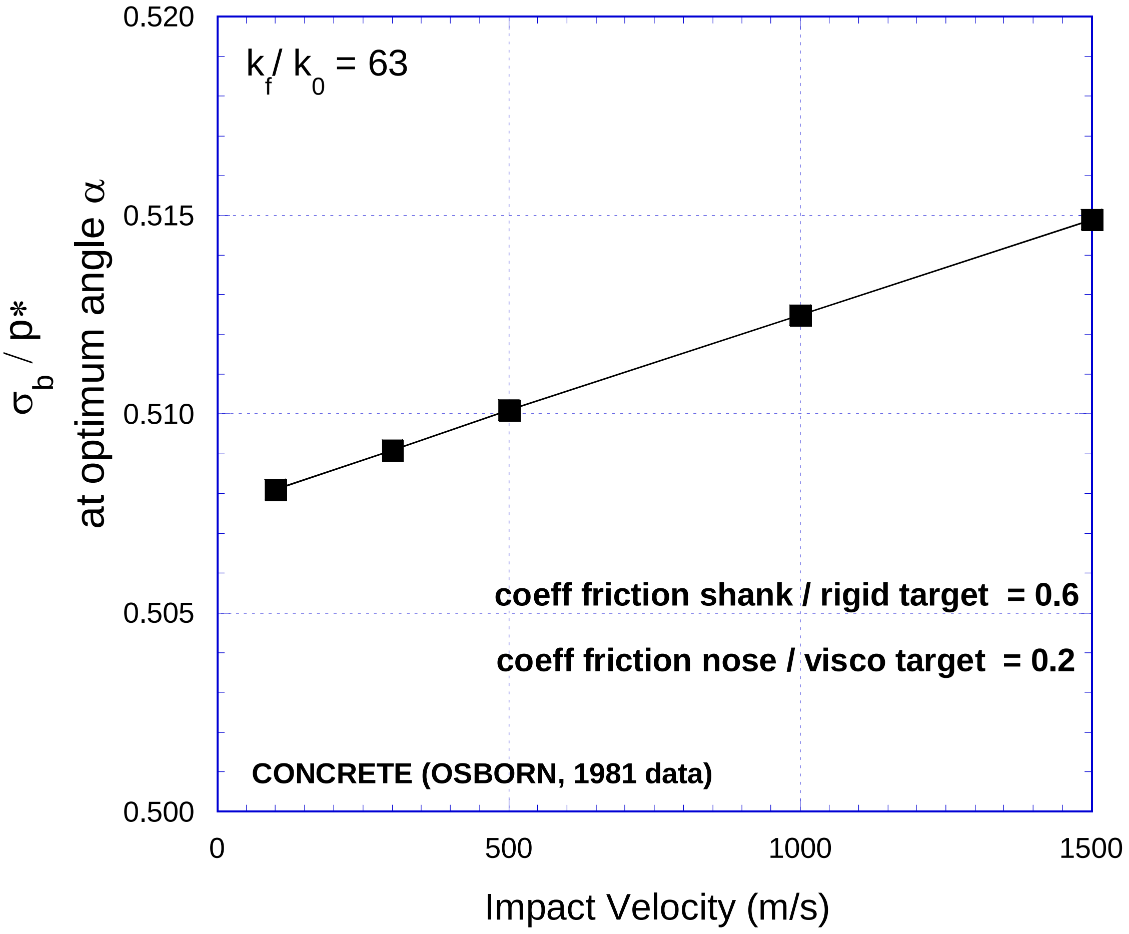

Figure 3.9: Normalized resistance to penetration corresponding to the optimum projectile half-angle as a function of the impact velocity.

Next, we analyze the effect of interface conditions. Figure 3.10 shows the optimum nose half-angle vs. impact velocity curves corresponding to 2 different values of the friction coefficients between the nose and the target. All the other parameters of the model are the same as in the previous simulations. Figure 3.11 shows a comparison between the optimum nose angles corresponding to different contact conditions. Figure 3.12 shows the optimum projectile semi-angle vs. impact velocity for $k(\rho_f):k(\rho_0)=$ 63 and 30; coefficients of friction: μ = 0.2 and μ_r = 0.6. Figure 3.13 shows the optimum resistance to penetration versus impact velocity curves corresponding to the yield stress ratio of 63:30.

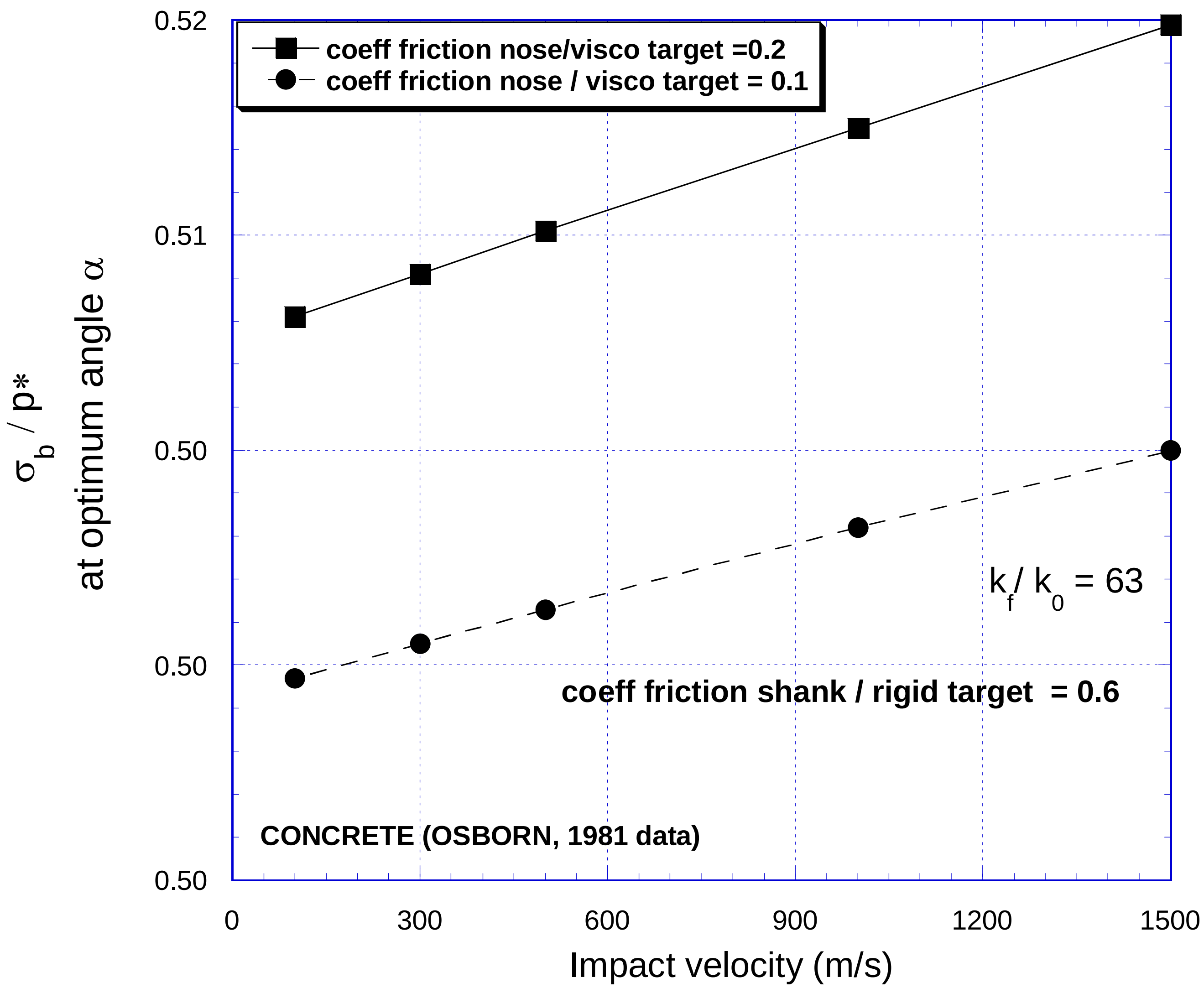

Figure 3.10: Effect of friction between nose and target: the lower the friction the sharper the optimal nose angle.

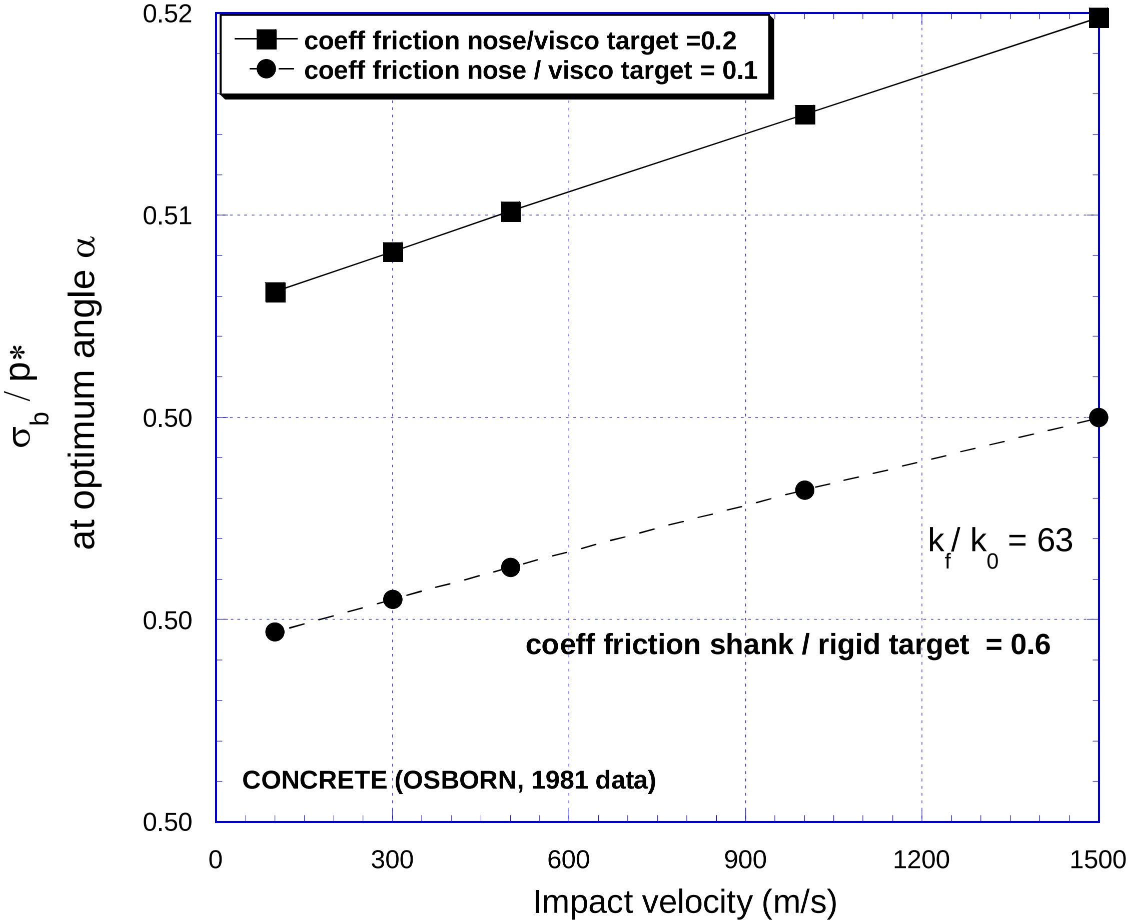

Figure 3.11: Resistance to penetration for optimum nose angle corresponding to different friction conditions at the nose/target interface.

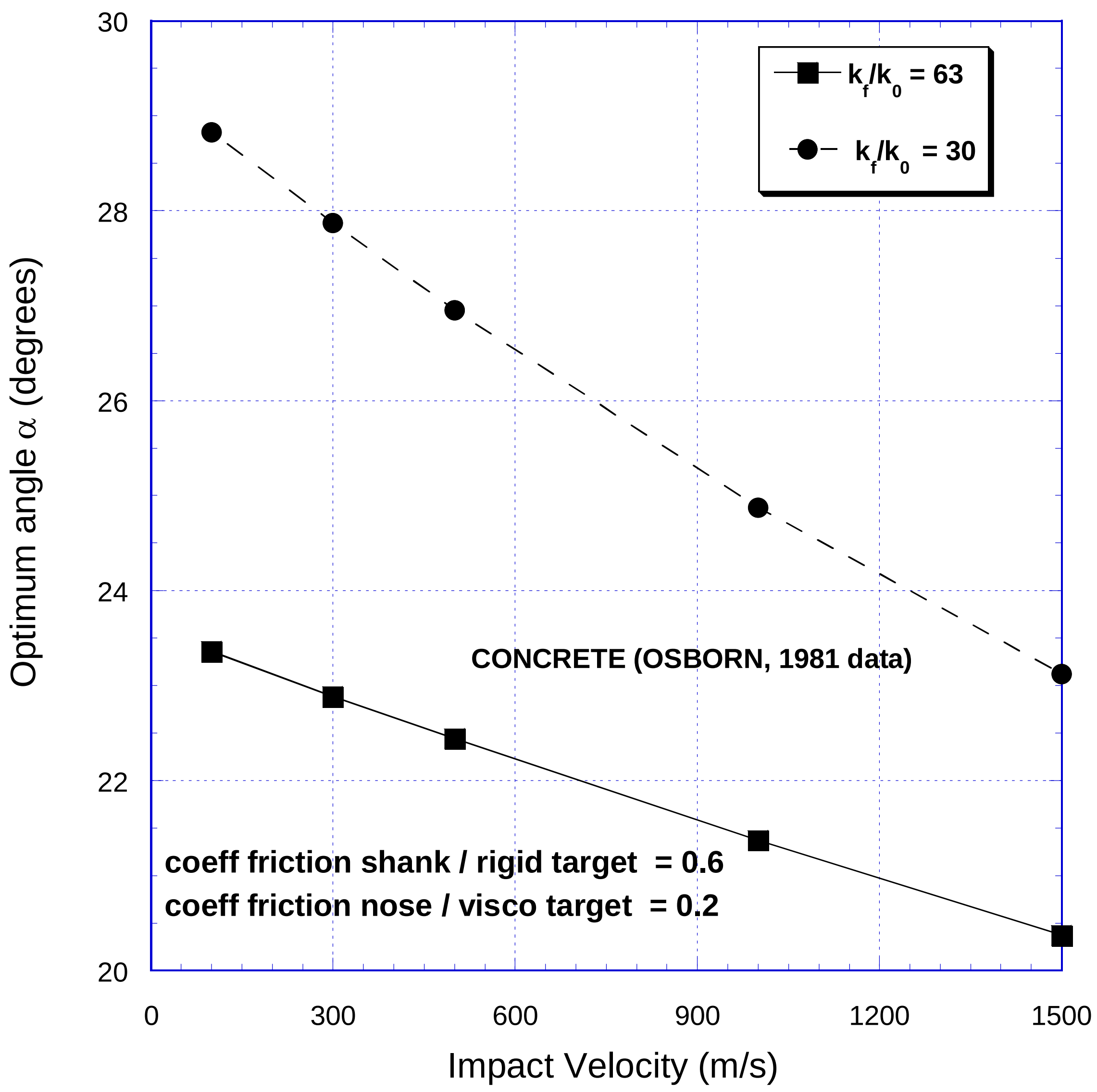

Figure 3.12: Optimum projectile semi-angle vs. impact velocity for $k(\rho_f):k(\rho_0) = 63:30$; coefficients of friction: $\mu = 0.2$ and $\mu_r = 0.6$.

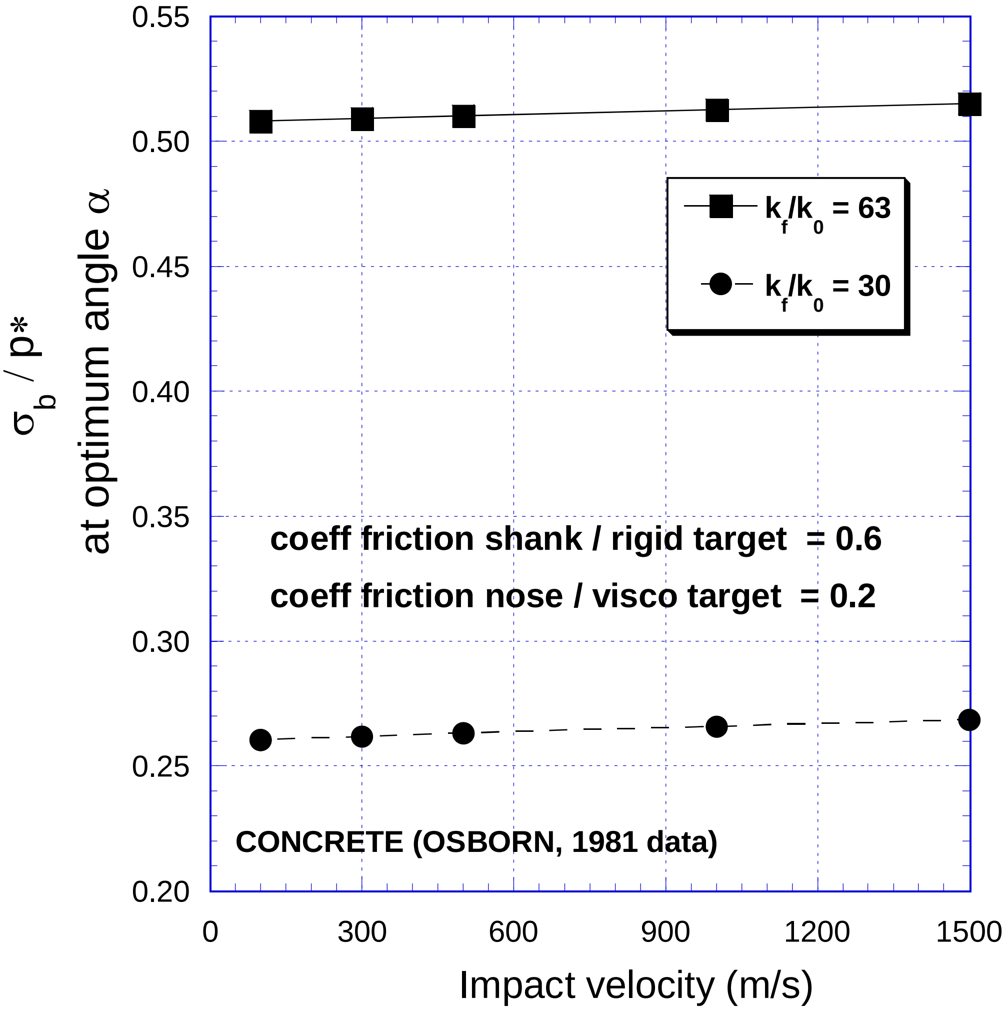

Figure 3.13: Resistance to penetration σ_b normalized by the locking pressure $p*$ corresponding to optimum nose semi-angles as a function of impact velocity for $k(\rho_f):k(\rho_0)$ = 63 and 30; coefficients of friction: μ = 0.2 and μ_r = 0.6.

The calculated resistance to penetration values are in good agreement with those reported by Osborn (1981).

III. 5. Summary and Conclusions

The purpose of this study was the investigation of the feasibility of developing a simple analytical model of the planar steady-state horizontal flow of a compressible viscoplastic material with locked hydrostat between 2 rigid plates separated by a distance 2 (F+1)R and symmetric about the penetrator centerline, R being the wedge semi-width. Resistance to penetration was calculated for different interface conditions. It was shown that accounting for friction alters the optimal wedge geometry for penetration performance by blunting the nose (wedge semi-angle). The resistance to penetration at optimal nose angle is greater for higher impact velocity. Actual compaction levels are extremely difficult to assess. Likewise is the assessment of the friction that acts between bodies during high-velocity penetration. The analysis presented does, however, provide qualitative insight into the penetration process and the role that friction plays at low to intermediate impact velocities. The conclusions of this study should be verified using alternative friction laws. This effort has been undertaken in Cazacu, Ionescu and Perrot (2004) where a slip-dependent friction law as well as the possibility of separation between the target and penetrator was considered.

References Section III

Heuze, F. E., An overview of projectile penetration into geologic materials, with emphasis on rocks. *Int.J.Rock Mech. Min. Sci*. 1990; **27:** 1-14.

Zukas, J.A., Nichols, T., H. F., Greszczuk, L. B., and Curran, D. R. *Impact Dynamics*. Wiley New York; 155-214, 1990.

Goodier, J.N. On the mechanics of indentation and cratering in solid targets of strain-hardening metal by impact of hard and soft spheres, *Proceedings of the 7th Symposium on Hypervelocity Impact*, Vol. III, Tampa, FL, Martin Company, 1965.

Hanagud, S. and Ross, B. Large deformation deep penetration theory for a compressible strain-hardening target material. AIAA Journal, 1971, **9**: 905-911.

Forrestal, M. J. and Luk, V. K., Dynamic spherical cavity expansion in a compressible elastic-plastic solid, *J. Appl. Mech.* 1988, **55**: 275-279.

Warren, T. L. and Forrestal, M.J. Effects of strain hardening and strain-rate sensitivity on the penetration of aluminum targets with spherical-nose rods, *Int. J. Solids Structures*.1998, **35** (28-29): 3737-3753.

Cazacu O. and Cristescu N. D. Constitutive model and analysis of creep flow of natural slopes. *Italian Geotechnical Journal* 2000: **34** (3): 44-54.

Cristescu N.D., Cazacu O. and Cristescu C., A Model for slow motion of natural slopes, *Canadian Geotechnical Journal,* 2002, **39**, 4: 924-937.

Schmidt M. J., High Pressure and High Strain Rate Behavior of Cementitious Materials: Experiments and Elastic/Viscoplastic Modeling. PhD dissertation, University of Florida, 2003.

Jones, E. S., Wilson, L. L., Jerome, D. M., and Christopher, F. R. (1998) An engineering analysis of normal rigid body penetration into concrete, PVP, 361, Structures Under Extreme Loading Conditions, ASME.

Avitzur B., (1968), Metal Forming: Processes and Analysis, Mc Grow Hill, New York

Cazacu, O, Ionescu, I.R., and Perrot, T. Penetration of a rigid body into a viscoplastic compressible fluid, *Proc. 4th European Congress on Computational Methods in Applied Sciences and Engineering*, P. Neittaanmäki, T. Rossi, K. Majava, and O. Pironneau, Jyväskylä, Eds., Finland, 24-28 July 2004, pp.1-18.

DISTRIBUTION LIST
AFRL-MN-EG-TR-2005-7030

Defense Technical Information Center 8725 John J. Kingman Road, Ste 0944 Ft Belvoir, VA 22060-6218	1

EGLIN AFB OFFICES:

AFRL/MN CA-N	1
AFRL/MNOC-1 (STINFO Office)	1

AFRL/MNA	1
AFRL/MNAC (DR. LIJEWSKI)	1
AFRL/MNAC (DR. VANDEN)	1
AFRL/MNAC (DR. SCHMIDT)	1
AFRL/MNAC (MR. NIXON)	1
AFRL/MNAC (DR. TU)	1
AFRL/MNAC (DR. WILSON)	1
AFRL/MNAC (MR. STEWART)	1
AFRL/MNAC (DR. NANCE)	1
AFRL/MNAC (MR. KEEN)	1
AFRL/MNAC (MAJ. HILBUN)	1
AFRL/MNAC (LT. SCHEARER)	1
AFRL/MNAC (MR. ELLISON)	1
AFRL/MNAC (MR. STANDLEY)	1
GERC, University of Fl (Dr. Cazacu)	1